Astronomy & Astrophysics manuscript no. sn2011dh-2-v4
January 30, 2014

The type IIb SN 2011dh - 2 years of observations and modelling of the bolometric and photometric lightcurves.

M. Ergon[1], A. Jerkstrand[2] **Group 1 (in alphabetic order):**, M. Bersten[6], N. Elias-Rosa[5], C. Fransson[1], M. Fraser[2], A. Pastorello[3], J. Sollerman[1], S. Taubenberger[4], S. Valenti[3] **Group 2 (in alphabetic order, to be extended):**, S. Benetti[3], S. Smartt[2], and L. Tomasella[3]

[1] The Oskar Klein Centre, Department of Astronomy, AlbaNova, Stockholm University, 106 91 Stockholm, Sweden
[2] Astrophysics Research Center, School of Mathematics and Physics, Queens University Belfast, Belfast, BT7 1NN, UK
[3] INAF, Osservatorio Astronomico di Padova, vicolo dell'Osservatorio n. 5, 35122 Padua, Italy
[4] Max-Planck-Institut für Astrophysik, Karl-Schwarzschild-Str. 1, D-85741 Garching, Germany
[5] Institut de Ciències de l'Espai (IEEC-CSIC), Facultat de Ciències, Campus UAB, E-08193 Bellaterra, Spain.
[6] Kavli Institute for the Physics and Mathematics of the Universe, Todai Institutes for Advanced Study, University of Tokyo, 5-1-5 Kashiwanoha, Kashiwa, Chiba 277-8583, Japan

Submitted to Astronomy and Astrophysics

ABSTRACT

We present optical and near-infrared (NIR) photometry and spectroscopy of the Type IIb supernova (SN) 2011dh spanning 2 years, and modelling of the bolometric and photometric lightcurves using hydrodynamical modelling for the diffusion phase (3-40 days) and early tail (40-100 days) and steady-state NLTE modelling for the late tail (100-500 days). The hydrodynamical modelling use a fitting procedure based on a model grid, which allows us to determine the errors in the results arising from the observed quantities. Using this method we find a helium core mass of $3.4^{+0.6}_{-0.3}$ $M_\odot$, an explosion energy of $0.55^{+0.40}_{-0.16}\times10^{51}$ erg and a mass of ejected ^{56}Ni of $0.075^{+0.028}_{-0.017}$ $M_\odot$ for SN 2011dh and similar values for SNe 1993J and 2008ax, although the mass of ^{56}Ni depends sensitively on the adopted distance and extinction. Steady-state NLTE modelling of the 100-500 days bolometric and photometric lightcurves, using a restricted set of ejecta models, gives a good fit for a model corresponding to a star of 12 $M_\odot$ initial mass, consistent with our results from the steady-state NLTE modelling of the nebular spectra in Jerkstrand et al. (2014), the hydrodynamical modelling in Bersten et al. (2012) and this paper and the progenitor analysis in Maund et al. (2011). Time-dependent NLTE modelling shows that after 600 days freeze-out in the helium envelope becomes important and a steady-state assumption is no longer valid. The energy deposition in our optimal model is dominated by the positrons emitted in the decay of ^{56}Co after 450 days, but we find it likely that the emitted flux is dominated by recombination emission caused by the freeze-out or other energy sources after 600 days. We find an excess in the MIR as compared to model photometry developing between 100 and 200 days, during which an increase in the optical tail decline rates is also observed. This behaviour could be explained by a modest amount of dust (τ = 0.25) being formed in the ejecta during this period, although the photometric evolution in the MIR is only partly reproduced. A modest amount of CO first overtone band emission is detected at 89 and 202 days implying a contribution to the Spitzer 4.5 μm band from CO fundamental band emission. We present an analysis of the nebular spectra complementary to the steady-state NLTE modelling in Jerkstrand et al. (2014). Estimates of the sizes of the line emitting regions, ranging from ~3000 km s^{-1} for the oxygen lines to ~1500 km s^{-1} for the iron lines, suggest partial mixing of the nuclear burning zones, and the sizes of these regions are in all compared cases smaller than for SNe 1993J and 2008ax. The profiles of the [O I] 6300 Å and Mg I] 4571 Å lines show a remarkable similarity, suggesting these lines to be emitted by the same material and to originate from the O/Ne/Mg zone. We use small scale fluctuations in these line profiles to estimate a filling factor of the line emitting material of $\lesssim$0.07, and repetitions of the fluctuations in the [O I] 6300 Å and [O I] 6364 Å lines to estimate a line ratio close to 3, consistent with optically thin emission, from 200 days and onwards. The [O I] 6300 Å, [O I] 5577 Å and Mg I] 4571 Å lines all show significant blue-shifts decreasing towards zero at 400 days, which we find to be consistent with an absorptive continuum opacity in the line emitting regions, similarly decreasing with time. This paper concludes our extensive observational and modelling work on SN 2011dh presented in a series of papers. The initial masses of $\lesssim$15 $M_\odot$ found for SNe 2011dh, 1993J and 2008ax, by hydrodynamical modelling of the bolometric lightcurves and steady-state NLTE modelling of nebular spectra in Jerkstrand et al. (2014), suggest that all of these Type IIb SNe originates from binary systems, as previously established for SN 1993J. !The length of this abstract is of course far to long. However, I kept it this way so you could comment on what to keep and not to keep.!

Key words. supernovae: general — supernovae: individual (SN 2011dh) — galaxies: individual (M51)

1. Introduction

Type IIb supernovae (SNe) are observationally characterized by a transition from Type II (with hydrogen lines) at early times to Type Ib (without hydrogen lines but with helium lines) at later times. The physical interpretation is that these SNe arise from stars that have lost most of their hydrogen envelop, either through stellar winds or interaction with a binary companion. Which of these production channels are dominating is still debated but for SN 1993J, the prime example of such an SNe, a companion star was detected by direct observations (Maund et al. 2004). The evolution of this binary system has been successfully modelled (Podsiadlowski et al. 1993; Stancliffe & Eldridge 2009) and it is widely accepted that the companion was

responsible for the removal of the hydrogen envelope. Bright, nearby Type IIb SNe as 1993J, 2008ax and the recent 2011dh are essential to improve our understanding of this class. Observations of the progenitor star in pre-explosion images, a search for the companion star when the SN has faded and multi-method modelling of high quality data, all provide important clues to the nature of Type IIb SNe and their progenitor stars.

In this paper we present the extensive optical and near-infrared (NIR) dataset, covering nearly two years, that we have obtained for SN 2011dh. The first 100 days of this dataset have been presented in Ergon et al. (2013, herafter E14). Detailed hydrodynamical modelling of the SN using those data were presented in Bersten et al. (2012, hereafter B12) and steady-state NLTE modelling of nebular spectra in Jerkstrand et al. (2014, hereafter J14). Identification and analysis of the plausible progenitor star was presented in Maund et al. (2011, hereafter M11) and confirmation of the progenitor identification through its disappearance in E14.

SN 2011dh was discovered on 2011 May 31.893 UT (Griga et al. 2011) in the nearby galaxy M51 at a distance of 7.8 Mpc (E14). The SN has been extensively monitored from X-ray to radio wavelengths by several teams. Most observations cover the 3-100 days period, but late time data have been published in Tsvetkov et al. (2012), Van Dyk et al. (2013), Sahu et al. (2013), Shivvers et al. (2013) and Helou et al. (2013). As in E14 we focus on the UV to MIR emission. The explosion epoch, the distance to M51 and the interstellar line-of-sight extinction towards the SN used in this paper, are all adopted from E14.

The nature of the progenitor star has been a key issue since the identification of a yellow supergiant in pre-explosion images, coincident with the SN (M11; Van Dyk et al. 2011). Recent progress in modelling of the SN (B12; J14; Shivvers et al. 2013) and the disappearance of the progenitor candidate (E14; Van Dyk et al. 2013) strengthens the hypothesis that the progenitor was a yellow supergiant of moderate mass, as was originally proposed in M11. In this paper we present further modelling in support of this hypothesis. As shown in Benvenuto et al. (2013) a binary interaction scenario that reproduces the observed and modelled properties of the yellow supergiant is possible. HST observations that could detect or set useful constraints on the presence of a companion star are scheduled for Cycle 21.

The paper is organized as follows. In Sect. 2 we present the observations and describe the reduction and calibration procedures and in Sect. 3 we present an observational analysis and comparison of the observations to SNe 1993J and 2008ax. In Sect. 4 we model the bolometric and photometric lightcurves and in Sect. 5 we discuss the interpretation of the observations given our optimal model and discuss and review the results obtained so far and our current understanding of Type IIb SNe. Finally, we conclude and summarize the paper in Sect. 6. In Appendix A we provide details on the hydrodynamical modelling.

2. Observations

2.1. Software

As in E14 two different software packages have been used for 2-D reductions, measurements and calibrations of the data. The IRAF based QUBA pipeline (Valenti et al. 2011, hereafter V11) and another IRAF based package which we will refer to as the SNE pipeline. This package has been developed with the particular aim to provide the high level of automation needed for large sets of data.

2.2. Imaging

An extensive campaign of optical and NIR imaging was initiated for SN 2011dh shortly after discovery using a multitude of different instruments. The observations during the first 100 days have been described in E14. The late time data were obtained with the Liverpool Telescope (LT), the Nordic Optical Telescope (NOT), Telescopio Nazionale (TNG), the Calar Alto 3.5m (CA 3.5m) and 2.2m (CA 2.2m) telescopes, the Asiago 67/92cm Schmidt (AS Schmidt) and 1.82m Copernico (AS 1.82m) telescopes, the William Herschel Telescope (WHT), the Albanova Telescope (AT) and the United Kingdom Infrared Telescope (UKIRT). The major contributors were the NOT, the AS Schmidt and the AT for the optical observations and the the CA 3.5m, the WHT and the UKIRT for the NIR observations. The late time dataset includes 61 epochs of optical imaging and 9 epochs of NIR imaging which, together with the early time observations, gives a total of 146 epochs of optical imaging and 32 epochs of NIR imaging.

2.2.1. Reductions and calibration

The optical and NIR raw data have been reduced with the QUBA and SNE packages respectively as described in E14, except for the optical LT and NIR UKIRT data for which reductions provided by the automated telescope pipelines have been used. Photometry was performed with the SNE pipeline as described in E14. Comparison to photometry on template subtracted images shows that the background contamination is negligible before ~300 days after which we have used photometry on template subtracted images. The optical and NIR photometry was calibrated to the Johnson-Cousins (JC), Sloan Digital Sky Survey (SDSS) and 2 Micron All Sky Survey (2MASS) systems as described in E14 where we also discuss the related uncertainties. The photometry was transformed to the standard systems using S-corrections (Stritzinger et al. 2002) as described in E14, except for the JC U and SDSS u bands which were transformed using the linear colour-terms tabulated in E14. As discussed in E14 we find the calibration to be accurate to within five percent in all bands for the first 100 days. The accuracy of the late time photometry depends critically on the accuracy of the S-corrections. The late time JC and SDSS photometry were mainly obtained with the NOT but comparisons between S-corrected NOT, LT and CA 2.2m JC and SDSS observations at ~300 days show differences at the 5 percent level suggesting that this precision is maintained. We note that in this phase S-corrections are absolutely necessary. For example the difference between the NOT and CA 2.2m I band observations are almost one magnitude at ~300 days if these are not applied, mainly because of the strong [Ca II] 7291,7323 Å and Ca II 8498,8542,8662 Å lines. The late time 2MASS photometry was obtained with a number of different telescopes and although the sampling is sparse the shape of the lightcurves suggests that the errors in the S-corrections are modest. Note that we have used JC-like *UBVRI* filters and SDSS-like *gz* filters at NOT whereas we have used JC-like *BV* filters and SDSS-like *ugriz* filters at LT. The JC-like *URI* and SDSS-like *uri* photometry were then tied to both the JC and SDSS systems to produce full sets of JC and SDSS photometry.

!We probably add a discussion here, or possible a separate section, on the very late time observations and the uncertainties in these.!

2.2.2. Space Telescope Observations

We have also performed photometry on the Spitzer 3.6 and 4.5 μm imaging[1] using the SNE pipeline as described in E14 to calculate magnitudes in the natural (energy flux based) Vega system of IRAC. All Spitzer images were template subtracted as described in E14 and the photometry is in good agreement with that published in Helou et al. (2013) !quantify this!. Optical and UV SWIFT magnitudes were published in E14.

2.2.3. Results

The S-corrected optical and NIR magnitudes and their corresponding errors are listed in Tables 4, 5 and 6 and the Spitzer 3.6 and 4.5 μm magnitudes and their corresponding errors in Table 7. For completeness we also include the magnitudes for the first 100 days already published in E14. All magnitudes, including the SWIFT magnitudes published in E14, are shown in Fig. 1 which also shows cubic spline fits using 3-5 point knot separation, error weighting and a 5 percent error floor or, when the sampling is sparse, linear interpolations. All calculations in Sect. 3, including the construction of the bolometric lightcurve, are based on these spline fits and linear interpolations. In these calculations the errors in the fitted splines have been estimated as the standard deviation and then propagated.

2.3. Spectroscopy

An extensive campaign of optical and NIR spectroscopic observations was initiated for SN 2011dh shortly after discovery with data obtained from a multitude of telescopes. The observations during the first 100 days have been described in E14. The late time data were obtained with the NOT, the TNG, the WHT, the CA 2.2m, the Asiago 1.22m Galileo telescope (AS 1.22m), and the Gran Telescopio Canarias (GTC). The major contributors were the NOT, the WHT and the GTC. Details of all spectroscopic observations, the telescope and instrument used, epoch and instrument characteristics are given in Table 8. The late time dataset includes 18 optical spectra obtained at 13 epochs and 2 NIR spectra obtained at 2 epochs which, together with the early time observations, gives a total of 73 optical spectra obtained at 39 epochs and 20 NIR spectra obtained at 12 epochs.

2.3.1. Reductions and calibration

The optical and NIR raw data were reduced and the flux extracted using the QUBA and SNE pipelines respectively as described in E14. The optical and NIR spectra were flux and wavelength calibrated using the QUBA and SNE pipelines respectively as described in E14. The absolute flux scale of all spectra has been calibrated against interpolated photometry using a least square fit to all bands for which the mean energy wavelength is at least half an equivalent width within the spectral range.

!Some spectra still has to be corrected for telluric absorption. The wavelength calibration of all spectra, with the important exception of the ~200 days NIR spectra, have been checked against skylines but some have not been shifted yet (but in all these cases the shift is very small).!

[1] Obtained through the DDT program by G. Helou.

2.3.2. Results

All reduced, extracted and calibrated spectra will be made available for download from the Weizmann Interactive Supernova data REPository[2] (WISeREP) (Yaron & Gal-Yam 2012). Figure 3 shows the sequence of observed spectra where those obtained on the same night using the same telescope and instrument have been combined. For clarity some figures in this and the following sections are based on time-interpolations of the spectral sequence as described in E14. To further visualize the evolution, the spectra have been aligned to a time axis at the right border of the panels. Interpolated spectra were used in the calculations of the bolometric lightcurve (Sect. 3.2) and S-corrections. Figure 2 shows the interpolated optical and NIR spectral evolution of SN 2011dh for 5−425 days with a 20-day sampling. All spectra in this and subsequent figures have been corrected for redshift and interstellar extinction.

3. Analysis

In this section we provide an analysis of the data and a comparison of these to the Type IIb SNe 1993J and 2008ax. Besides SN 2011dh, these are the best monitored Type IIb SNe so far, which motivates a detailed comparison. Both occurred in nearby galaxies, have progenitor detections and well constrained explosion epochs. We keep the analysis of the photometric and bolometric evolution observational, as we return to the physical interpretation in Sect. 4, where we present steady-state NLTE and hydrodynamical modelling of these data. The analysis of the spectral evolution is complementary to the steady-state NLTE modelling of these data in J14, and we therefore frequently refer to this paper and the results obtained therein. The early (0-100 days) evolution of SN 2011dh, as well as comparisons in this phase to SNe 1993J and 2008ax, were discussed in E14, and here we focus on the evolution after 100 days.

As discussed in E14, the systematic errors stemming from the uncertainties in distance and extinction are large for all three SNe, which should be kept in mind when absolute quantities are compared. For SNe 1993J and 2008ax we adopt the same values and error bars for the distance and extinction as in E14. The references for the photometric and spectroscopic data of SNe 1993J and 2008ax used in the comparison are the same as specified in E14 !not true, we use additional late time data!. We note that the lack of S-corrected photometry for SN 1993J complicates the comparison, whereas for SN 2008ax the S-corrected JC photometry by Taubenberger et al. (2011) agrees reasonably well with the JC photometry by Tsvetkov et al. (2009).

3.1. Photometric evolution

Absolute magnitudes were calculated as in E14. In Fig. 4 we show absolute optical and NIR magnitudes for SN 2011dh as compared to SNe 1993J and 2008ax, and in Table 1 we tabulate the tail decline rates at 100, 200 and 300 days. Most striking is the similarity between the lightcurves, except for a shift towards higher luminosities for SNe 1993J and 2008ax, the shift being larger in bluer bands and negligible in the NIR and most pronounced for SN 2008ax. As discussed in E14, this difference could be explained by an error in the adopted extinctions.

Given the caveat that SNe 1993J and 2008ax are only partly covered in U and NIR, we find the following general trends. At 100 days the V, R and I decline rates are roughly twice the decay

[2] http://www.weizmann.ac.il/astrophysics/wiserep/

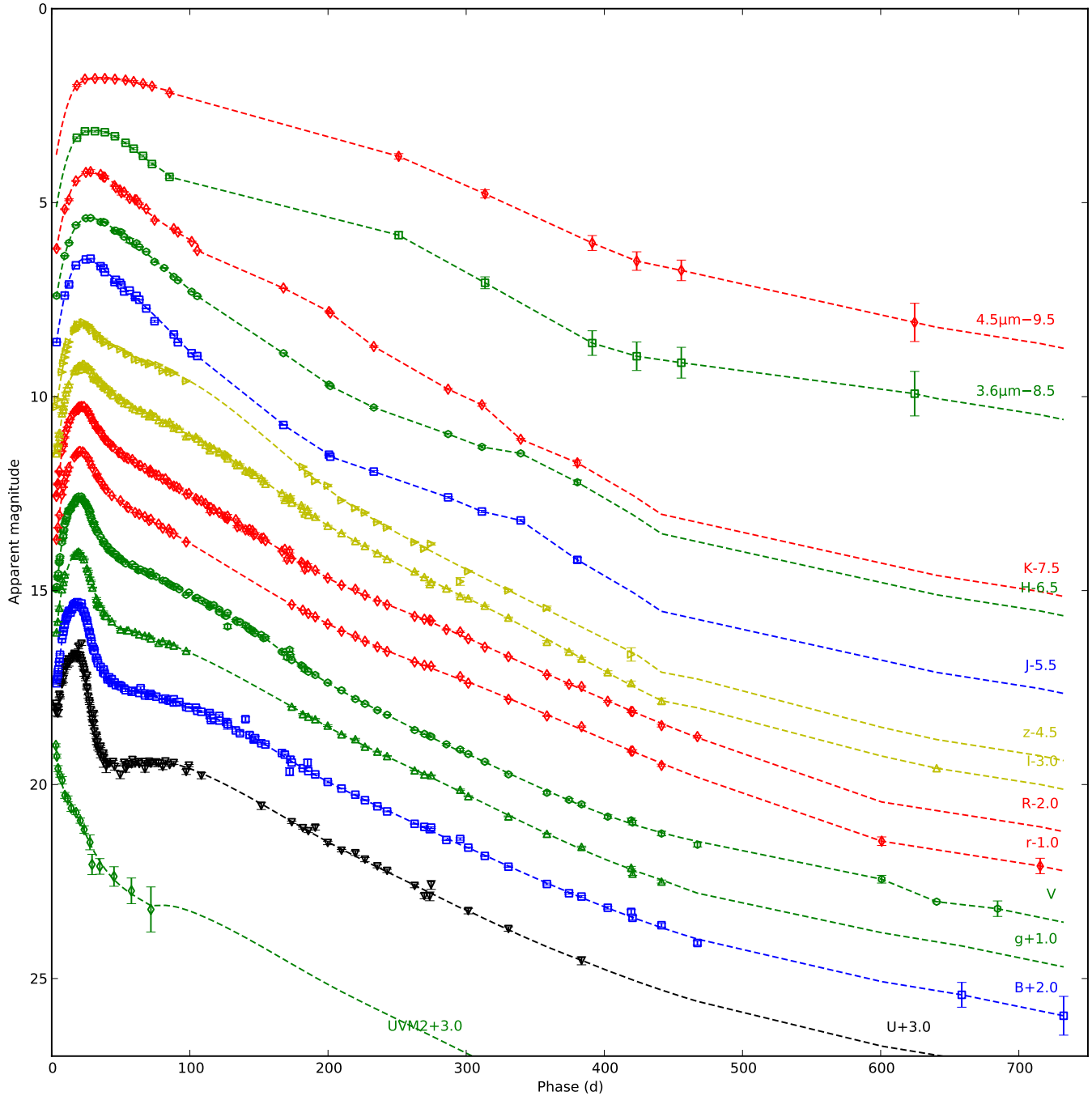

Fig. 1. Photometric evolution of SN 2011dh in the UV, optical, NIR and MIR. For clarity each band has been shifted in magnitude. Each lightcurve has been annotated with the name of the band and the shift applied. We also show the S-corrected SWIFT JC photometry (crosses) and cubic spline fits or linear interpolations (dashed lines).

rate of ^{56}Co, and subsequently decrease towards 300 days. The *U* and *B* decline rates are significantly lower at 100 days, subsequently approach the other optical decline rates and then evolve similarly. The *J* and *H* band decline rates are considerably higher than the optical at 100 days, subsequently approach those and eventually become considerably lower. For SNe 2011dh and 1993J the *K* band behaves quite differently than the other NIR bands. At 100 days the decline rate is significantly lower, but as it remains roughly constant, it subsequently approach the other NIR decline rates and eventually becomes condsiderably higher. As seen in Fig. 1, the optical lightcurves of SN 2011dh flattens considerably after ∼450 days, approaching a decline rate similar to, or lower, than the decay rate of ^{56}Co.

Both SNe 2011dh and 1993J were also monitored in the MIR, SN 2011dh in the Spitzer 3.6 and 4.5 μm bands and SN 1993J in the *L* band, which is similar to the Spitzer 3.6 μm band. For both SNe a strong excess in the MIR develops between ∼100 and ∼250 days. For SN 1993J the MIR coverage ends at ∼250 days and for SN 2011dh the subsequent evolution is fairly similar to the evolution in the optical, and the considerable flattening seen in the optical lightcurves after ∼450 days, is also seen in the Spitzer lightcurves.

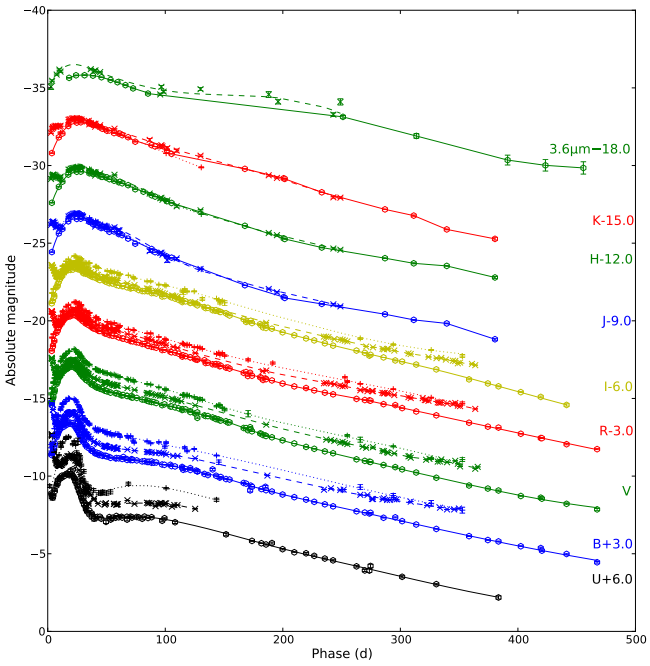

Fig. 4. Photometric evolution of SN 2011dh (dots) in the optical and NIR as compared to SNe 1993J (crosses) and 2008ax (pluses). For clarity each band has been shifted in magnitude. Each lightcurve has been annotated with the name of the band and the shift applied.

!I have removed a discussion on the colour evolution here. Maybe this should be included, I'm not sure. It is a very long paper.!

3.2. Bolometric evolution

As in E14 we have used a combination of the spectroscopic and photometric methods, applied to wavelength regions with and without spectral information respectively, when calculating the pseudo-bolometric lightcurves. The details of these methods have been described in E14.

Figure 5 shows the *U* to *K* (3300-24000 Å) pseudo-bolometric lightcurves for SN 2011dh as compared to SNe 1993J and 2008ax for the 0-500 days period as calculated with the photometric method, and in Table 2 we tabulate the decline rates at 100, 200 and 300 days. Given the caveat that SNe 1993J and 2008ax are not covered in NIR after ~250 and ~150 days respectively, their *U* to *K* pseudo-bolometric lightcurves are remarkably similar to the one of SN 2011dh, except for the shift towards higher luminosities discussed previously in Sect. 3.1. The decline rates decreases from ~0.020 mag day^{-1}, roughly twice the decay rate of ^{56}Co, at 100 days to ~0.015 mag day^{-1} at 400 days. There is however a significant increase in the decline rate between ~150 and ~200 days for SN 2011dh, not seen for SNe 1993J and 2008ax. For SN 1993J the decline rate becomes increasingly lower towards 300 days as compared to SNe 2011dh and 2008ax, which is consistent with an increasing contribution from CSM interaction in this phase.

Figure 6 shows the UV to MIR (1900-50000 Å) pseudo-bolometric lightcurve for SN 2011dh, as calculated with the combined spectroscopic and photometric methods, and in Table 9 we tabulate the 3-300 days period (for which we have full UV to MIR coverage) for reference. As expected, the UV to MIR and *U* to *K* pseudo-bolometric lightcurves are very similar. The decline rates at 100, 200, 300 and 400 days are 0.021, 0.022, 0.015 and 0.016 mag day^{-1}, but the increase in decline rate between ~150 and ~200 days is not as pronounced as in the *U* to *K* pseudo-bolometric lightcurve. Given the caveats that the NIR coverage ends at ~350 days, and the sampling is sparse and

Table 1. Tail decline rates at 100, 200 and 300 days for SN 2011dh compared to SNe 1993J and 2008ax as measured from cubic spline fits.

SN	Band	Rate (100 d) (mag day^{-1})	Rate (200 d) (mag day^{-1})	Rate (300 d) (mag day^{-1})
2011dh	*U*	0.013	0.019	0.018
2011dh	*B*	0.014	0.019	0.017
2011dh	*V*	0.018	0.021	0.018
2011dh	*R*	0.020	0.019	0.016
2011dh	*I*	0.019	0.021	0.017
2011dh	*J*	0.036	0.017	0.012
2011dh	*H*	0.029	0.019	0.011
2011dh	*K*	0.020	0.020	0.024
1993J	*U*	0.006	...	...
1993J	*B*	0.011	0.017	0.012
1993J	*V*	0.019	0.019	0.017
1993J	*R*	0.022	0.015	0.013
1993J	*I*	0.022	0.019	0.013
1993J	*J*	0.041	0.016	...
1993J	*H*	0.033	0.018	...
1993J	*K*	0.023	0.022	...
2008ax	*U*	0.013	...	...
2008ax	*B*	0.015	0.018	0.016
2008ax	*V*	0.022	0.018	0.017
2008ax	*R*	0.023	0.016	0.015
2008ax	*I*	0.018	0.021	0.013
2008ax	*J*	0.035	...	...
2008ax	*H*	0.032	...	...
2008ax	*K*	0.033	...	...

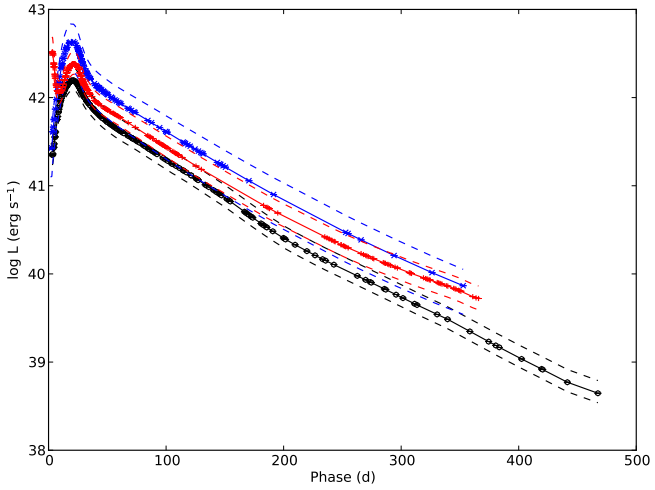

Fig. 5. Pseudo-bolometric *U* to *K* lightcurve for SN 2011dh (black circles and solid line) calculated with the photometric method as compared to SNe 1993J (red crosses and solid line) and 2008ax (blue pluses and solid line). The upper and lower error bars for the systematic error arising from extinction and distance (dashed lines) are also shown.

Table 2. Tail decline rates at 100, 200, and 300 days for the *U* to *K* bolometric lightcurve of SN 2011dh compared to SNe 1993J and 2008ax.

SN	Rate (100 d) (mag day^{-1})	Rate (200 d) (mag day^{-1})	Rate (300 d) (mag day^{-1})
2011dh	0.021	0.021	0.016
2008ax	0.020	0.017	0.015
1993J	0.021	0.017	0.013

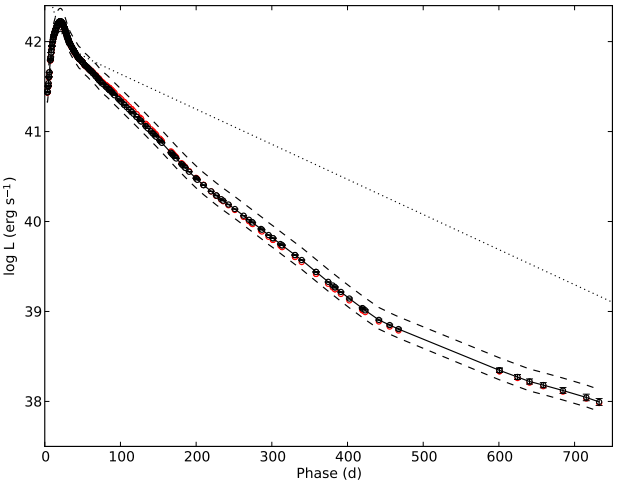

Fig. 6. Pseudo-bolometric UV to MIR lightcurve for SN 2011dh calculated with the spectroscopic (black circles and solid line) and photometric (red circles) method. The upper and lower error bars for the systematic error arising from extinction and distance (black dashed lines) and the radioactive decay chain luminosity of 0.075 $M_\odot$ of ^{56}Ni (black dotted line) are also shown.

the measurement errors large after ~500 days, the UV to MIR pseudo-bolometric lightcurve show a significant flattening after ~500 days, when the decline rate decreases to a value similar to, but lower than, the decay rate of ^{56}Co.

Figure 7 shows the fractional UV (1900-3300 Å), optical (3300-10000 Å), NIR (10000-24000 Å) and MIR (24000-50000 Å) luminosities for SN 2011dh. The early evolution was discussed in E14, and after 100 days the most notable is the strong increase in the MIR fraction between ~100 and ~250 days. The subsequent evolution becomes quite uncertain after ~350 days when the NIR coverage ends and ~500 days when the sampling and measurement errors become worse, but the optical, NIR and MIR fractions seems to be roughly constant during this period. Keeping these uncertainties in mind it is worth noting the dominance of the optical flux even at ~750 days.

Figure 8 shows the evolution of the SED as calculated with the photometric method, overplotted with blackbody fits to the *B*, *V*, *I*, *J*, *H* and *K* photometry as well as the observed (interpolated) spectra. The early evolution was discussed in E14, and after 100 days the most notable is again the strong excess developing in the MIR between ~100 and ~250 days. There also seems to be a similar excess developing in the *K* band between ~100 and ~200 days, gradually fading away towards 300 days.

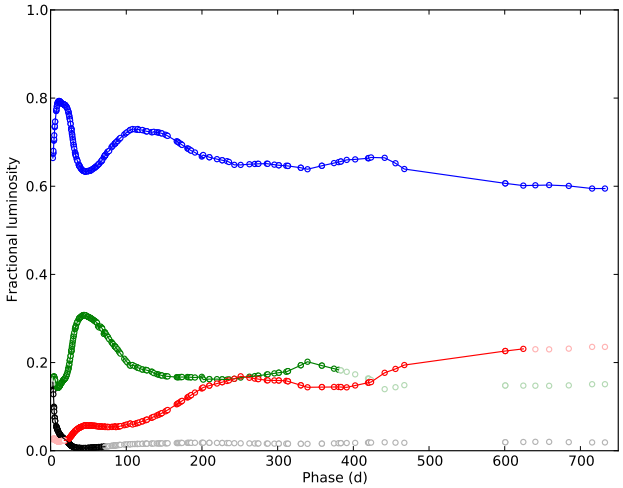

Fig. 7. Fractional UV (black dots), optical (blue dots), NIR (green dots) and MIR (red dots) luminosity for SN 2011dh. Extrapolations are display in shaded colour.

3.3. Spectroscopic evolution

The early spectral evolution was discussed in some detail in E14 and in this section we focus on the spectral evolution from 100 days and onwards. Steady-state NLTE modelling of this evolution as well as a detailed analysis of the formation of the identified lines and the evolution of their fluxes are presented in J14. In this section we summarize the findings in J14 and provide a complementary analysis, mainly related to the line profiles and what can be learned about the distribution of the material from the different nuclear burning zones. In doing this we refer to the subdivision of the ejecta described in J14 with a Fe/Co core surrounded by the Si/S zone, the oxygen-rich O/Si/S, O/Ne/Mg and O/C zones, the helium-rich He/C and He/N zones and the hydrogen-rich envelope. The amount of macroscopic mixing between these zones is determined by hydrodynamical instabilities in the explosion (Hammer et al. 2010) and is a free parameter in the steady-state NLTE modelling.

In Sect. 3.3.1 we describe our methods for characterization of the line profiles and estimation of the line emitting regions, in Sects. 3.3.2-3.3.8 we discuss the identified lines element by element, in Sect. 3.3.10 we discuss small scale variations in the line profiles and in Sect. 3.3.11 we compare the line profiles of SN 2011dh to those of SNe 1993J and 2008ax.

3.3.1. Line profiles and emitting regions

To characterize the line profiles in an observational way we calculate the typical wavelength and widths of the lines. The typical wavelength of the line is calculated as the first wavelength moment of the flux (center of flux) and the typical widths as the blue- and red-side regions containing 76 percent of the flux, corresponding to the half-width-half-maximum (HWHM) of a Gaussian profile. Both these quantities are quite insensitive to the continuum subtraction and are thus suitable for characterization and comparison to other SNe. The continuum level is determined by a linear interpolation between the minimum flux levels on the blue and red sides within a region set to ±6000 km s^{-1} for most of the lines, ±10000 km s^{-1} for the Ca II 8662 Å line and ±3000 km s^{-1} for the [Fe II] 7155 Å line.

Figure 10 shows the center of flux and blue- and red-side widths as compared to the rest wavelength for the [O I]

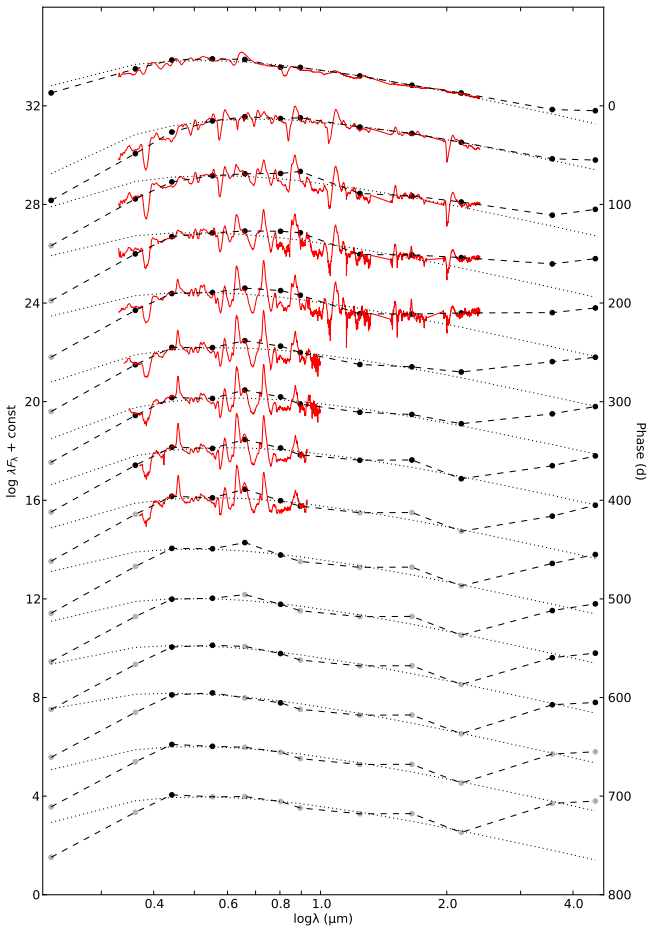

Fig. 8. The evolution of the SED as calculated with the photometric method (black dots and dashed lines) overplotted with blackbody fits to the *V*, *I*, *J*, *H* and *K* photometry (black dotted lines) as well as the observed spectra interpolated as described in Sect. 2.3.2 (red solid lines). Extrapolations fare displayed in shaded colour.

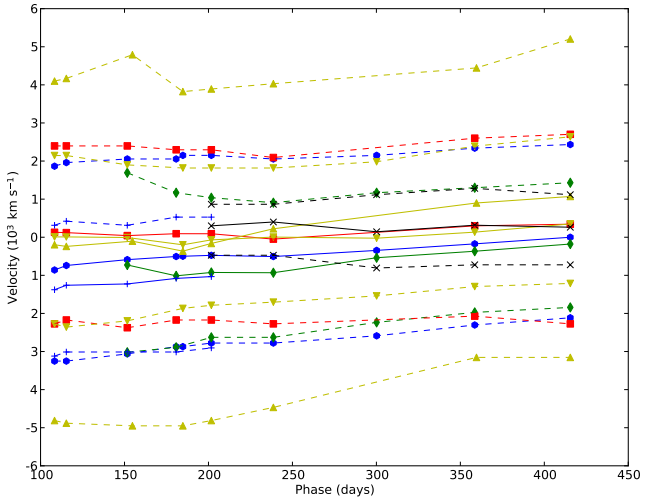

Fig. 10. Center of flux velocities (solid lines) and the blue- and red-side widths (dashed lines) as compared to the rest wavelengths for the [O I] 6300,6364 Å (blue dots), Mg I 4571] Å (green diamonds), Na I 5890,5896 Å (red squares), [Ca II] 7291,7323 Å (yellow downward triangles), Ca II 8498,8542,8662 Å (yellow upward triangles), [Fe II] 7155 Å (black crosses) and [O I] 5577 Å (blue pluses) lines.

6300,6364 Å, [O I] 5577 Å, Mg I] 4571 Å, Na I 5890,5896 Å, [Ca II] 7291,7323 Å, Ca II 8498,8542,8662 Å and [Fe II] 7155 Å lines calculated with this method. The rest wavelength is assumed to be 6316 Å for the [O I] 6300,6364 Å line as is appropriate for a line ratio of 3 and 5993 Å, 7307 Å and 8662 Å for the Na I 5890,5896 Å, [Ca II] 7291,7323 Å and Ca II 8498,8542,8662 Å lines respectively.

To estimate the sizes of the line emitting regions and the absorptive continuum optical depths required to cause the blueshift of the typical wavelength seen in many lines we use a method based partly on the knowledge gained from J14. For lines found to be optically thin using the steady-state NLTE modelling, we fit the line profile of a spherically symmetric region of constant line emissivity, optically thin in the line and with a constant absorptive continuum opacity, to the observed line profile. This gives a rough estimate of the size of the region responsible for the bulk of the line emission.

Some lines arise as a blend of more than one line which has to be taken into account. The [O I] 6300 Å flux was calculated by iterative subtraction of the [O I] 6364 Å flux, from the left to the right, using $F_{6300}(\lambda) = F_{6300,6364}(\lambda) - F_{6300}(\lambda - \Delta\lambda)/R$, where $\Delta\lambda$ is the wavelength separation between the [O I] 6300 Å and 6364 Å lines and R the [O I] 6300,6364 Å line ratio. This ratio was assumed to be 3, as is supported by the steady-state NLTE modelling and estimates based on small scale variations (Sect. 3.3.10). In all other cases, where the line ratios of the blended lines are not known, we make a a simultaneous fit assuming the same size of the emitting region for all of the blended lines.

3.3.2. Hydrogen lines

Summary of the findings in J14: No (isolated) hydrogen lines are identified. Some Hα emission arising from the hydrogen-rich envelope is present, but is found to be increasingly dominated by [N II] 6548,6583 Å emission arising from the helium zone after ~150 days. No detectable absorption is found in Hα or any of the other hydrogen lines.

Figure 9 shows the post 100 days (interpolated) spectral evolution centred on the Hα line. There is a dip in the [O I] 6300,6364 Å line profile after ~150 days, that corresponds well to the early time Hα absorption minimum at ~11000 km s^{-1} (E14). However, as discussed in Sect. 3.3.10, this feature repeats in a number of other lines and is rather due to clumping/asymmetries in the ejecta. There is also an emerging emission feature near the rest wavelength of Hα after ~200 days which, given the findings in J14, is rather be due to [N II] 6548,6583 Å emission.

Using the method described in Sect. 3.3.1, we find the feature to be well fitted by emission from a region with a radius of 5500 km s^{-1}, emitting mainly in the [N II] 6583 Å line, although the wings of the observed line profile may extend to ~12000 km s^{-1} on the red side. Hα emission from the hydrogen-rich envelope is expected to result in a flat-topped line profile, at least 11000 km s^{-1} wide (E14). The size of the line emitting region, as well as the extent of the wings, is instead consistent with emission from the helium zone, in agreement with the results in J14.

!But the peak at late times is exactly at the rest wavelength of Hα. What does this mean?!

3.3.3. Helium lines

Summary of the findings in J14: The (isolated) helium lines identified are the He I 10830 Å and He I 20581 Å lines, although the He I 10830 Å line is found to be blended with the [S I] 10820 Å line. The helium lines arise mainly from the helium zone, but there is also a significant contribution from helium in the Fe/Co zone. Both lines are found to be optically thick, implying a significant contribution from line scattering.

Figure. 9 shows the post 100 days (interpolated) spectral evolution for the identified helium lines. The He I 10830 Å and He I 20581 Å lines emerge at ∼10 and ∼15 days respectively (E14) and remain until our spectral coverage ends, both in emission and absorption.

Both the He I 10830 Å and He I 20581 Å lines have P-Cygni like profiles, suggesting a significant contribution from scattering, in agreement with the results in J14. Although the unblended He I 20581 Å line has a quite broad peak it is not flat-topped, suggesting a contribution from helium at low velocities. This is again in agreement with the results in J14, where we find helium in the F/Co zone to contribute significantly at low velocities.

3.3.4. Oxygen lines

Summary of the findings in J14: The (isolated) oxygen lines identified are the [O I] 5577 Å, O I 7774 Å, O I 9263 Å, O I 11300 Å, O I 13164 Å and [O I] 6300,6364 Å lines, although the O I 9263 Å line is found to be blended with the [Co II] 9338,9344 Å line on the blue side. All these lines are found to arise from the oxygen zones, the part arising from the O/C and O/Si/S zones depending sensitively on the amount of molecule (CO and SiO) cooling in these zones.

Figure 9 shows the post 100 days (interpolated) spectral evolution for the identified oxygen lines. The allowed oxygen lines emerge between ∼25 and ∼50 days (E14) and, except for the [O I] 5577 Å line which disappears at ∼300 days, remain until our spectral coverage ends. The [O I] 6300,6364 Å line emerge at ∼100 days and remains until our spectral coverage ends.

Using the method described in Sect. 3.3.1, we measure the radius of the [O I] 6300,6364 Å line emitting region to 3400, 3100 and 2900 km s^{-1} at 202, 300 and 415 days respectively. The line profile fits (Fig.11) are quite good, but the observed emission is underestimated at low velocities and extends to at least ∼5000 km s^{-1}, suggesting radially decreasing emissivity.

The center of flux of the [O I] 6300,6364 Å line shows a blue-shift of ∼1000 km s^{-1} at 100 days, decreasing towards zero at 400 days, whereas the center of flux of the [O I] 5577 Å line shows a blue-shift of ∼1500 km s^{-1} at 100 days, decreasing towards ∼1000 km s^{-1} at 200 days, when the line begins to fade away. Using the method described in Sect. 3.3.1, we find the blue-shift of the [O I] 6300,6364 Å line profile to be well fitted by a decreasing absorptive continuum opacity in the line emitting region. This is in agreement with the results in J14, where the cause of this blue-shift is found to be line-blocking in the core. We do not find any significant blue-shifts of the O I 11300 and 13164 Å lines, where we expect line-blocking to be less effective, in support of this hypothesis.

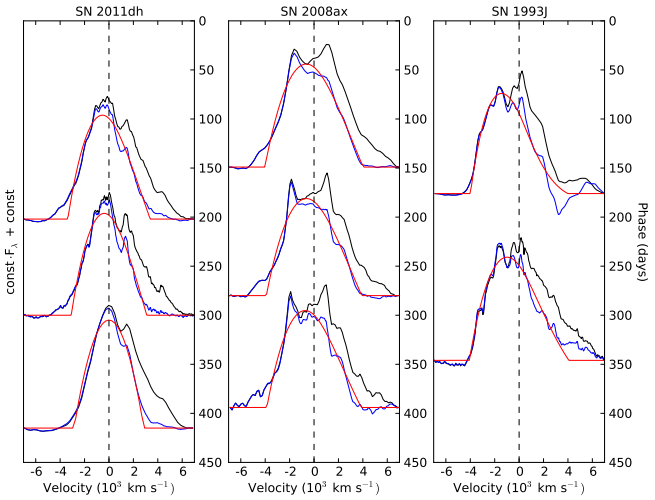

Fig. 11. [O I] 6300,6364 Å (black) and decomposed [O I] 6300 Å (blue) line profiles at selected epochs as compared to line profile fits (red) for SNe 2011dh (left panel), 2008ax (middle panel) and 1993J (right panel)

3.3.5. Sodium lines

Summary of the findings in J14: The only (isolated) sodium line identified is the Na I 5890,5896 Å line. Observationally this line is hard to disentangle from the He I 5876 Å line, but the emission is found to arise mainly from the Na I 5890,5896 Å line (although absorption could be a blend), and to be a combination of recombination emission from the O/Ne/Mg zone and scattering throughout the ejecta.

Figure 9 shows the post 100 days (interpolated) spectral evolution for the Na I 5890,5896 Å line. The line has a P-Cygni like profile, suggesting a significant contribution from scattering, in agreement with the results from J14 and remains, both in emission and absorption, until our spectral coverage ends.

3.3.6. Magnesium lines

Summary of findings in J14: The (isolated) magnesium lines identified are the Mg I] 4571 Å and Mg I 15040 Å lines, and both are found to arise mainly from the O/Ne/Mg zone.

Figure 9 show the post 100 days (interpolated) spectral evolution for the identified magnesium lines. The Mg I] 4571 Å line emerge at ∼150 days whereas the Mg I 15040 Å line may emerge as early as ∼40 days (E14) and both remain until our spectral coverage ends.

Using the method described in Sect. 3.3.1, we measure the radius of the Mg I] 4571 Å line emitting region to 3600, 2800 and 2700 km s^{-1} at 202, 300 and 415 days respectively, and the radius of the Mg I 15040 Å line emitting region to 3400 and 2900 km s^{-1} at 89 and 205 days respectively. The line profile fits (Fig. 12) of the Mg I] 4571 Å line are quite good, but the observed emission is underestimated at low velocities and extends to at least ∼5000 km s^{-1}, suggesting radially decreasing emissivity.

The center of flux of the Mg I] 4571 Å line shows a blue-shift of ∼1000 km s^{-1} at ∼200 days, decreasing towards a few hundred km s^{-1} at ∼400 days. Using the method described in Sect. 3.3.1, we find the blue-shift of the Mg I] 4571 Å line profile to be well fitted by a decreasing absorptive continuum opacity in

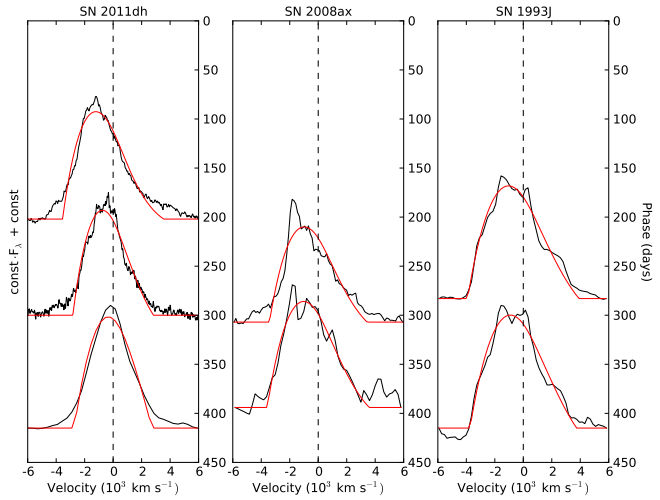

Fig. 12. Mg I] 4571 Å line profiles (black) at selected epochs as compared to line profile fits (red) for SNe 2011dh (left panel), 2008ax (middle panel) and 1993J (right panel).

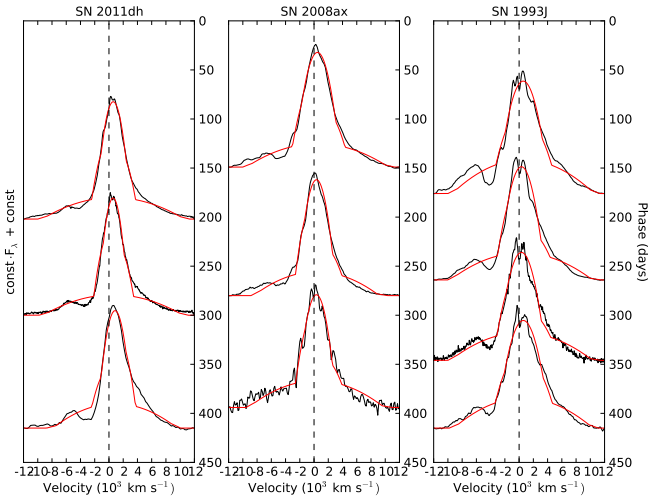

Fig. 13. [Ca II] 7291,7323 Å line profiles (black) at selected epochs as compared to line profile fits (red) for SNe 2011dh (left panel), 2008ax (middle panel) and 1993J (right panel).

the line emitting region. This is in agreement with the results from J14, where the cause of this blue-shift is found to be line-blocking in the core. We don't find any significant blue-shift of the Mg I 15040 Å line, where we expect line-blocking to be less effective, in support of this hypothesis.

The estimated radius of the Mg I line emitting region of 2700-3600 km s^{-1} is similar to the estimated radius of the O I line emitting region of 2900-3400 km s^{-1}. As mentioned above the Mg I lines is found in J14 to arise from the O/Ne/Mg zone and the O I lines to arise from the O/Ne/Mg zone and, depending on the amount of molecule (CO and SiO) cooling, the O/C and O/Si/S zones. As is evident from Figs. 11 and 12 (but see also Fig. 16) the profiles of the [O I] 6300 and the Mg I] 4571 Å lines are very similar suggesting these to arise from the O/Ne/Mg zone. In Sect. 3.3.10 we find this to be true also for small scale variations in the line profiles in further support of this hypothesis.

3.3.7. Calcium lines

Summary of the findings in J14: The (isolated) calcium lines identified are the Ca II 3934,3968 Å, Ca II 8498,8542,8662 Å and [Ca II] 7291,7323 Å lines. Absorption in the Ca II 3934,3968 Å lines is found to occur throughout the ejecta and the Ca II 8498,8542,8662 Å lines to arise mainly from fluorescence in these lines. The [Ca II] 7291,7323 Å lines, on the other hand, is found to arise mainly from the Si/S zone, with a possible contribution throughout the ejecta from fluorescence in the Ca II 3934,3968 Å lines. The Ca II 8498,8542,8662 Å line is found to be blended with the [C I] 8727 Å line, arising mainly from the O/C zone, the amount of blending depending sensitively on the amount of molecule (CO) cooling in this zone.

Figure 9 shows the post 100 days (interpolated) spectral evolution for the identified calcium lines. The Ca II 3934,3968 Å line is present initially in absorption (E14) and remains so until the spectral coverage ends. The Ca II 8498,8542,8662 Å line is present initially with a P-Cygni profile (E14), but disappears in absorption at ∼100 days. The Ca II 8498,8542 Å lines disappear in emission at ∼300 days, whereas the Ca II 8662 Å line remains until the spectral coverage ends. The [Ca II] 7291,7323 Å line emerges at ∼100 days and remains until the spectral coverage ends.

Using the method described in Sect. 3.3.1, we measure the radii of a two-component [Ca II] 7291,7323 Å line emitting region to 2400/9900, 2100/9100 and 2400/9000 km s^{-1} at 202, 300 and 415 days respectively. The line profile fits (Fig. 13) are good in the inner region but worse in the wings, which are quite asymmetric and also blended with the [Fe II] 7155 Å line on the blue side. The more pronounced red-side wing could indicate a P-Cygni like contribution from scattering.

The center of flux for the Ca II 8498,8542,8662 Å line shows a red-shift increasing towards ∼1000 km s^{-1} at 400 days. As the center of flux is calculated with respect to the rest wavelength of the Ca II 8662 Å line (Sect. 3.3.1) this suggests a significant contribution from the [C I] 8727 Å line to the flux, which is in agreement with the results from J14 if the amount of molecule (CO) cooling in the C/O zone is modest.

The size of the inner [Ca II] 7291,7323 Å line-emitting region of 2100-2400 km s^{-1} is less than the 2700-3600 km s^{-1} found for the Mg I and O I line emitting regions which, assuming this emission arise mainly from the Si/S zone (see above), suggests partial mixing of the Si/S zone and the surrounding oxygen zones. The size of the outer [Ca II] 7291,7323 line-emitting region of 9000-9900 km s^{-1} implies a contribution from calcium in the helium zone.

3.3.8. Iron group lines

Summary of the findings in J14: The (isolated) iron lines identified are the [Fe II] 7155 Å, [Fe II] 12600 Å and [Fe II] 16400 Å lines. The (isolated) cobalt lines identified are the [Co II] 9338,9344 Å, [Co II] 10190,10248,10283 Å and [Co II] 15475 Å lines, although the [Co II] 9338,9344 Å line is found to be blended with the O I 9263 Å line on the blue side. All of the identified iron and cobalt lines are found to arise from the Fe/Co zone.

Figure. 9 shows the post 100 days (interpolated) spectral evolution for the identified iron and cobalt lines. The [Fe II] 7155 Å line emerges at ∼150 days and remains until our spectral coverage ends. The [Fe II] 12600 Å and [Fe II] 16400 Å lines are

identified in our last NIR spectrum at ~200 days, although the identification of the former is a bit doubtful given the large offset from the rest wavelength. The [Co II] 9338,9344 Å line may emerge as early as ~50 days and remains until our spectral coverage ends, whereas the [Co II] 10190,10248,10283 Å and [Co II] 15475 Å lines are identified in our last NIR spectrum at ~200 days.

Using the method described in Sect. 3.3.1, we measure the radius of the [Fe II] 7155 Å line emitting region to 1600 km s^{-1} at 300 and 415 days, and the radius of the [Fe II] 16440 Å line emitting region to 2100 km^{-1} at 206 days. We also measure the radius of the [Co II] 10190,10248,10283 Å line emitting region to 2000 km s^{-1} at 206 days. The [Co II] 15475 Å line is noisy, but we find the radius of the line-emitting region to be 3200 km s^{-1} at 206 days. As mentioned the [Co II] 9338,9344 Å line is blended with the O I 9263 Å line on the blue side, and also appears to be blended with other lines on the red side, so we do not attempt to estimate the radius of the line emitting region.

Except for the [Co II] 15475 Å line at 206 days, the estimates of the size of the Fe II and Co II line emitting region lies in the range 1600-2100 km s^{-1}, significantly smaller than the 2700-3600 km s^{-1} estimated for the O I and Mg I line emitting region. This is consistent with a scenario where the Fe/Co core and the surrounding oxygen zones are only partially mixed. However, as discussed in Sect. 4.5, hydrodynamical modelling of the early lightcurve strongly suggest that some amount of Fe/Co core material have been mixed far out in the ejecta. This is not neccesarily in conflict with the Fe II and Co II line profiles as this amount may be small enough not to be clearly visible.

3.3.9. CO overtone band

Figure 14 shows continuum subtracted observed K band spectra at 89 and 206 days compared to the synthetic K band spectrum at 200 days for the optimal steady-state NLTE model (Sect. 4.1). The region where we expect CO overtone mission is marked in the figure and is assumed to be 22750-24350 Å (reference). The continuum was estimated as a linear interpolation between the endpoint fluxes of the region averaged over 100 Å. As seen in Fig. 14 there is a clear excess in the region both compared to the continuum and the model spectrum and the shape and extent of the feature is similar at 89 and 202 days. Although other explanations cannot be excluded we find it reasonable to interpret this feature as CO overtone emission.

The integrated continuum subtracted flux in the region was 3.1×10^{-14} and 8.1×10^{-15} erg s^{-1} cm^{-2} at 89 and 206 days respectively. These values should be taken with some care as they depend sensitively on the method used to subtract the continuum. The total flux in the 4.5 μm band, calculated using the zeropoint flux and the equivalent width of the band, was 4.9×10^{-13} and 1.7×10^{-13} erg s^{-1} cm^{-2} at 89 and 206 days respectively. Note that the value at 206 days lies in the gap of the Spitzer observations and has been linearly interpolated between 85 and 251 days. If all of the flux in the 4.5 μm band was due to CO fundamental band emission this would correspond to fundamental to overtone band flux ratios of ~15 and ~20 at 85 and 206 days respectively.

3.3.10. Small scale fluctuations

Figure 15 shows small scale fluctuations in the [O I] 6300,6364 Å, [O I] 5577 Å, O I 7774 Å, Mg I] 4571 Å and Na I 5890,5896

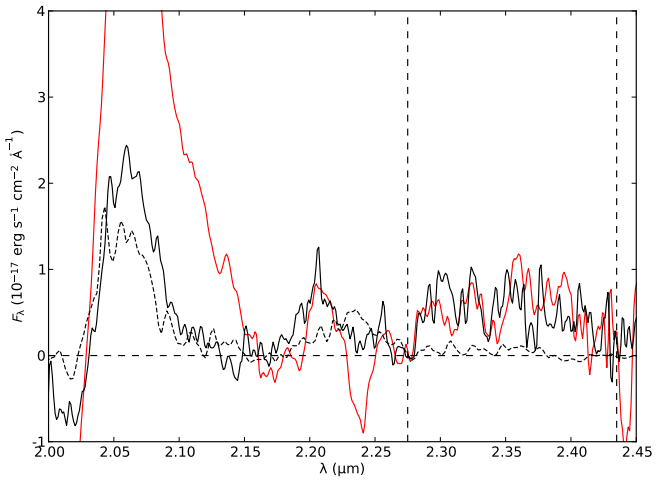

Fig. 14. Continuum subtracted observed K band spectra at 89 (red solid line) and 206 (black solid line) days compared to the continuum subtracted synthetic K band spectrum at 200 days (black dashed line) for the optimal steady-state NLTE model. The CO overtone region have been marked by black dashed lines and the observed flux at 206 days scaled with the ratio of the measured total CO overtone fluxes.

Å lines at 202 and 300 days. The resolution is ~600 and ~250 km s^{-1} in the 202 and 300 days spectra respectively. A 1000 km s^{-1} box average of the line profile was repeatedly (3 times) subtracted to enhance the small scale fluctuations. We have tested this method on the product of synthetic large and small scale structures and the small scale structure is recovered with reasonable accuracy. In the upper left panel we show a comparison of the [O I] 6300 Å line profiles at 202 and 300 days. These are very similar and there is not much evolution of the small scale fluctuations in the line profile during this period. We identify 8 features marked A-H with an FWHM between 300 and 600 km s^{-1} present at both epochs.

However, features G and H interpreted as belonging to the [O I] 6364 Å line match very well with the E and F features interpreted as belonging to the [O I] 6300 Å line so these are likely to be repetitions. Minimizing the RMS (Root Mean Square) of the small scale fluctuations redwards 3000 km s^{-1} (G and H), where the [O I] 6364 Å flux was subtracted from the [O I] 6300,6364 Å line profile using the method described in Sect. 3.3.1, we find a line ratio of 2.9 at 202 and 300 days to give a complete removal of features G and H. This ratio is in agreement with the value of 3 expected for optically thin emission and also with the results from J14.

In the upper right panel we show the corrected [O I] 6300 Å line profile and in the lower left panel we show a comparison to the Mg I] 4571 Å line profile at 300 days. All features except B are clearly identified and the agreement is good. The features on the blue side is weaker for the Mg I] 4571 Å line, which is consistent with the larger red-side flux deficit for this line, but the relative (flux normalized) strength of all features are similar. The good agreement suggests that the [O I] 6300 Å and Mg I] 4571 Å lines arise from the same nuclear burning zones. Given that the Mg I] 4571 Å lines arises mainly from the O/Ne/Mg zone, as found in J14, it also suggests that the [O I] 6300 Å line arises mainly from this zone and that the contribution from the O/Si/S and O/C zones are modest.

In the lower right panel we show a comparison of the corrected [O I] 6300 Å line profile and the [O I] 5577 Å, O I 7774

Å and Na I 5890,5896 Å line profiles at 202 days. The E and F features are clearly identified in all of these line profiles, but none of the other features are seen. Since the E and F features are also the strongest it is not clear if the absence of the other features is real or if the other features are just too faint to be seen. The relative strength of the E and F features are similar for the [O I] 5577 Å, O I 7774 Å and [O I] 6300 Å lines, suggesting that all these lines arise mainly from the same nuclear burning zones, whereas the relative strength of these features for the Na I 5890,5896 Å line is a bit (~50 percent) weaker, suggesting contributions from other nuclear burning zones. This is in agreement with the results in J14, where all oxygen lines are found to arise from the oxygen zones and the Na I 5890,5896 Å line partly from the O/Ne/Mg zone.

The small scale fluctuations in the [Ca II] 7291,7323 Å line (not shown) does not match very well with those in the [O I] 6300 Å line and the relative strength of the features seen is weaker. We were not able to correct for blending as for the [O I] 6300,6364 Å line, which makes the interpretation less clear, but the result is in agreement with the results in J14, were we found this line to arise from other nucluear burning zones. This is also suggested by different sizes of the line emitting regions discussed in Sect. 3.3.7.

Shivvers et al. (2013) presented an analysis of the line profiles of the [O I] 6300,6364 Å, O I 7774 Å and Mg I 4571 Å lines at 268 days. By decomposition of the [O I] 6300,6364 Å line profile into Gaussian profiles, assuming a [O I] 6300,6364 Å line ratio of 3, they found a good fit for one broad and two narrow profiles located at -400 and 1600 km s^{-1}. The two strongest features in our analysis, E and F, are located at ~0 and ~1500 km s^{-1} and likely correspond to the two features found by Shivvers et al. (2013). They also find these features to repeat in the O I 7774 Å and Mg I 4571 Å lines, in agreement with our analysis. The difference in velocity for the E feature is likely explained by the different methods used.

Matheson et al. (2000) presented an analysis of the small scale fluctuations in the line profiles of SN 1993J. They found a good agreement between the fluctuations in the [O I] 6300 Å, [O I] 5577 Å and O I 7774 Å line profiles, which is in agreement with our results for SN 2011dh. However, they did not find a good agreement between the fluctuations in the [O I] 6300 Å and Mg I] 4571 Å line profiles, which is a bit surprising since we find an excellent agreement between fluctuations in these lines for SN 2011dh. One possible explanation is that the [O I] 6300 Å line is dominated by flux from the O/Ne/Mg zone for SN 2011dh but not for SN 1993J, as we expect the Mg I] 4571 Å line to emerge from this zone, whereas the oxygen lines could also have contributions from the O/Si/S and O/C zones.

The small scale fluctuations observed provide evidence for a clumpy ejecta as have been previously demonstrated for SNe 1993J (Matheson et al. 2000) and 1987A (Stathakis et al. 1991; Chugai 1994). In a simplified way we may represent the material of some nuclear burning zone by a number of randomly distributed clumps, having a typical size and occupying some fraction of the ejecta volume (filling factor). The small scale fluctuations in the line profiles then arise from statistical fluctuations in the distribution of the clumps, the RMS of the fluctuations increasing with decreasing number of clumps and/or filling factor and/or increasing size of the clumps. In the simplest case the ejecta is assumed to be a (globally) homogeneous sphere, which is in fact exactly how the core is represented in the steady-state NLTE modelling (Sect. 4.1).

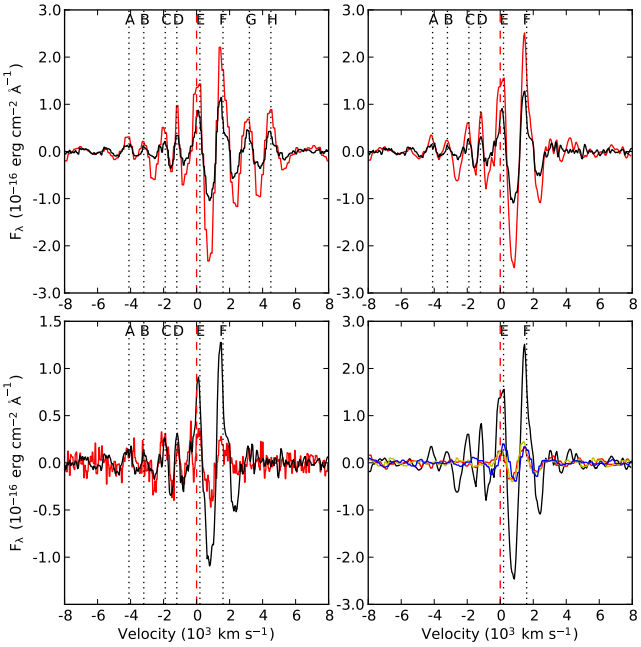

Fig. 15. Comparison of box average subtracted line profiles. The upper left panel shows the [O I] 6300 Å line profile at 202 (red) and 300 (black) days. The upper right panel shows the corrected [O I] 6300 Å line profile at 202 (red) and 300 (black) days. The lower left panel shows the corrected [O I] 6300 Å line profile (black) and the Mg I] 4571 Å line profile (red) at 300 days. The lower right panel shows the corrected [O I] 6364 Å line profile (black) and the [O I] 5577 Å (red), O I 7774 Å (green) and Na I 5890/5896 Å (blue) line profiles at 202 days.

Matheson et al. (2000) applied the statistical model by Chugai (1994) to their spectra of SN 1993J, giving a filling factor of ~0.06 for oxygen zone material, distributed within a sphere with 3800 km s^{-1} radius. Using their estimated typical clump size of 300 km s^{-1}, this corresponds to ~900 clumps. The model requires the radius of the sphere containing the clumps, the typical size of the clumps and the RMS of relative flux fluctuations in lines originating from the clumps. In the case of SN 2011dh we adopt a radius of the sphere containing the bulk of the oxygen zone material of ~3500 km s^{-1} based on the estimates of the O I and Mg I line emitting regions in Sect. 3.3.4 and 3.3.6. For SN 1987A a typical clump size of 120 km s^{-1} was estimated from the power spectrum of the [O I] 6300 Å line by Stathakis et al. (1991) using high-resolution spectroscopy, but it is not clear how this was done by Matheson et al. (2000). As we do not have access to high-resolution spectroscopy for SN 2011dh we can only estimate an upper limit on the typical clump size taken to be 300 km s^{-1}, the smallest size of the features seen. The RMS of the relative flux fluctuations in the inner part (±2000 km s^{-1}, see Chugai (1994)) of the sphere for both the corrected [O I] 6300 Å and the Mg I 4571 Å lines was ~0.09 at 300 days. Using these estimates and applying Chugai (1994, eq. 11), we find an upper limit on the filling factor of oxygen zone material within the sphere of ~0.07 and a lower limit on the number of oxygen zone clumps of ~900. These values are in good agreement with the values estimated by Matheson et al. (2000) for the clumping of oxygen zone material in SN 1993J.

3.3.11. Comparison to SNe 1993J and 2008ax

Figure 11, 12 and 13 shows a comparison of the (continuum subtracted) [O I] 6300 Å, Mg I] 4571 Å and [Ca II] 7291,7323 Å line profiles and fits using the method described in Sect. 3.3.1 for SNe 2011dh, 2008ax and 1993J respectively. The estimated radii of the line emitting regions are 4000-4100 and 3900-4000 km s^{-1} for the [O I] 6300 Å line, 3700-3900 and 3400-3600 km s^{-1} for the Mg I] 4571 Å line and 3000-3400 and 2600-3000 km s^{-1} for the [Ca II] 7291,7323 Å line for SNe 1993J and 2008ax respectively. These radii are in all cases significantly larger than the radii of the line emitting regions estimated for SN 2011dh (Sect. 3.3.4, 3.3.6 and 3.3.7), and are in all cases larger for SN 1993J than for SN 2008ax. The radius of the [Ca II] 7291,7323 Å line emitting region is in all cases smaller than the radii of the [O I 6300] Å and Mg I] 4571 Å line emitting regions, suggesting partial mixing of the Si/S zone and the surrounding oxygen zones as previously discussed for SN 2011dh in Sect. 3.3.7.

The shape of the [O I] 6300 Å and Mg I] 4571 Å line profiles for SNe 2008ax and 1993J differers from those of SN 2011dh and are significantly flatter at low velocities, most pronounced for SN 2008ax. This would in a spherical symmetric geometry suggest a lower fractional emissivity at low velocities as compared to SN 2011dh and possible a decreasing emissivity or even a void at low velocities. The shape of the [Ca II] 7291,7323 Å line profiles on the other hand are similar and centrally peaked for all SNe. Note that the double peaks of the [O I] 6300,6364 Å line profile for SN 2008ax discussed by Taubenberger et al. (2011), Maurer et al. (2010) and Milisavljevic & Fesen (2010) seem to be well explained by a repetition of the blue peak in the [O I] 6364 Å line and that this blue peak also seem to repeat in the Mg I] 4571 Å line.

Figure 16 shows the continuum subtracted mirrored blue-side profiles for the [O I] 6300 Å, Mg I] 4571 Å, [Ca II] 7291 Å and [Fe I] 7155 Å lines for SNe 2011dh, 2008ax and 1993J at 300, 307 and 283 days respectively. This figure nicely illustrates the different sizes of the line emitting regions and shapes of the line profiles discussed above. The blue side is less affected by obscuration as compared to the red side and contamination from the [O I] 6364 Å and [Ca II] 7323 Å lines to the [O I] 6300 Å and [Ca II] 7291 Å lines is probably modest, although the [Ca II] 7291,7323 Å line ratio is uncertain. Note the remarkable similarity between the [O I] 6300 Å and Mg I] 4571 Å line profiles seen for all SNe, previously discussed for SN 2011dh in Sect. 3.3.6 and 3.3.10.

For SN 2008ax a number of lines, including the Na I 5890,5896 Å, [O I] 5577, O I 7774 Å, Mg I 15040 Å, He I 10830 Å and He I 20581 Å lines, show flat-topped profiles either on the blue or both sides similar to those of the [O I] 6300 Å and Mg I] 4571 Å lines. This behaviour is quite different from SN 2011dh where no lines, except possibly the He I 20581 Å line, show flat-topped profiles. It is tempting to speculate that the differences in the shapes of line profiles, as well as the sizes of the line emitting regions, among the SNe are related to the geometry of the ejecta (or part of it) and differences in the viewing angle. In Sect. 4.5 we show that the explosion energy as well as the ejecta mass as determined from hydrodynamical modelling is similar for the three SNe (although the error bars are large). Assuming the geometry is similar for all three SNe we would observe broader and more flat-topped line-profiles if the ejecta is either elongated along the line-of-sight (e.g. bi-polar) or compressed along an axis perpendicular to the line-of-sight (e.g. disc or torus). However, more flat-topped line profiles would also be a natural consequence of a smaller degree of macroscopic mixing, preserving more of the original onion-like structure of the ejecta.

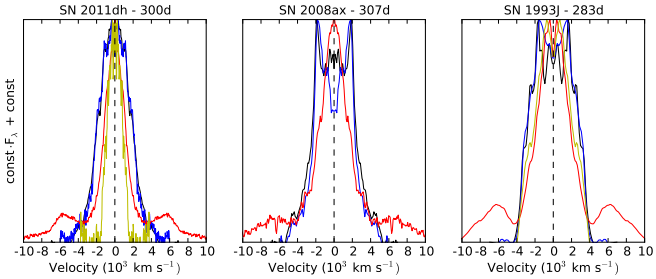

Fig. 16. Continuum subtracted mirrored blue-side profiles for the [O I] 6300,6364 Å (black), Mg I] 4571 Å (blue), [Ca II] 7291,7323 Å (red) and [Fe I] 7155 Å (yellow) lines for SNe 2011dh, 2008ax and 1993J at 300, 307 and 283 days respectively.

Figure 17 shows the center of flux velocities for the [O I] 6300,6364 Å, [O I] 5577 Å, Mg I] 4571 Å and [Ca II] 7291,7323 Å lines calculated as described in Sect. 3.3.1 for SNe 2011dh, 2008ax and 1993J. As discussed in Sects. 3.3.4 and 3.3.6 there is a blue-shift of the [O I] 6300,6364 Å, [O I] 5577 Å and Mg I] 4571 Å lines for SN 2011dh which, as seen in Fig. 17, is also present, and even more pronounced for SNe 2008ax and 1993J. For SN 2011dh this blue-shift disappears towards 400 days but for SN 2008ax and 1993J the blue-shift saturates at ~500 km s^{-1} after 200 days. As shown in Figs. 11 and 12 the asymmetric shape of the line profiles could be well explained by an absorptive continuum opacity in the line emitting region. In J14 we suggest the cause of this opacity to be line-blocking in the core as is also supported by the modelling. There is no significant blue shift in the O I 11300, 13164 Å and [Mg I] 15040 Å lines for SNe 2011dh (Sects. 3.3.4 and 3.3.6) and 2008ax in support of this hypothesis as we expect line-blocking to be less effective in the NIR. However, we also expect the line-blocking and thus the blue-shift to decrease with time as observed for SN 2011dh. The reason why this is not the case for SNe 2008ax and 1993J is unclear but if the density of the core is higher we would expect the line-blocking opacity to remain high for a longer time. For SN 2008ax an asymmetric distribution of the oxygen zone material towards the observer is contradicted by the absence of a blue-shift in the NIR lines. Milisavljevic & Fesen (2010) find the [O I] 6300,6364 Å, [O I] 5577 Å and Mg I] 4571 Å lines to be either symmetric or asymmetric towards the blue for a sample of stripped envelope SNe, which also favours obscuration of the receding-side emission as the explanation. It is worth noting that a higher optical depth in the core for SNe 2008ax and 1993J would be a natural consequence of the viewing angle for the ejecta geometries discussed above.

4. Modelling

In this section we discuss modelling of the bolometric and photometric lightcurves with the steady-state NLTE code used in J14 and described in Jerkstrand et al. (2011, 2012) and HDE, a new hydrodynamical code similar to the one used in B12 and described in Appendix A. In Sect. 4.1 we discuss modelling of the 0-500 days bolometric and photometric lightcurves with the steady-state NLTE code and the HDE code using the J14 ejecta models and in Sect. 4.2, 4.3 we discuss the effects on

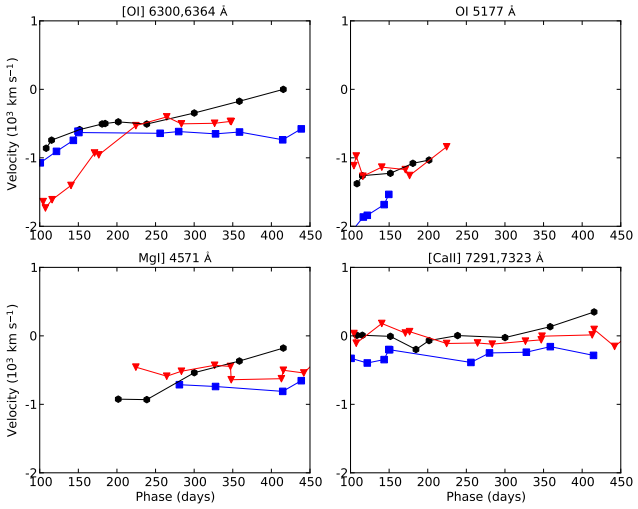

Fig. 17. Center of flux velocities for the [O I] 6300,6364 Å (upper left panel), [O I] 5577 Å (upper right panel) Mg I] 4571 Å (lower left panel), [Ca II] 7291,7323 Å (lower right panel) lines for SNe 2011dh (black dots), 2008ax (blue squares) and 1993J (red triangles).

these lightcurves by dust absorption and emission and molecule emission. In Sect. 4.4 we discuss the 500-750 days bolometric lightcurves and the effects of time dependent processes and other additional energy sources in this phase. In Sect. 4.5 we make a quantitative fit of the 0-100 days bolometric lightcurves of SNe 2011dh, 1993J and 2008ax using a model grid spanning a large volume of parameter space constructed with the hydrodynamical HDE code. In Sect. 4.6 we extend the temporal coverage of this model grid to 300 days and use a correction for the flux within the observed wavelength range determined by the steady-state NLTE modelling to fit the observed 3-300 days U to 4.5 μm pseudo-bolometric lightcurve of SN 2011dh.

4.1. Modelling of the 100-500 days bolometric lightcurve

In this section we compare synthetic pseudo-bolometric and photometric lightcurves for the J14 ejecta models to the observed 100-500 days pseudo-bolometric and photometric lightcurves. Unlike the hydrodynamical modelling in Sects. 4.5 and 4.6, the construction of a model grid is not computationally feasible. The fitting procedure is therefore by necessity qualitative, and the degeneracy of the solution and the errors in the results can not be quantified. To facilitate some qualitative understanding on how the solution varies in parameter space, we have constructed a restricted set of models listed in table 2 in J14. These models varies in at least one of the following parameters, initial mass (12, 13 or 17 $M_\odot$), degree of macroscopic mixing (medium or strong), positron trapping (local or free-streaming), molecule cooling (yes or no), dust absorption/emission (yes or no) and oxygen zone filling factor (small-large). The meaning of each parameter and the different configurations used are described in detail in J14.

The underlying 12, 13 and 17 $M_\odot$ ejecta models are constructed using the nucleosynthesis from Woosley & Heger (2007) and the density profiles for the helium and hydrogen envelope from B12, and are described in detail in J14. As by construction the ejecta models have not been evolved through the 0-100 days evolution, we use the HDE code set up to run in homologous mode to produce bolometric lightcurves for this phase and compare to the observed U to 4.5 μm pseudo-bolometric lightcurve. The initial temperature profile is taken to be that of the optimal (extended) hydrodynamical model found in Sect. 4.5. In the optimal (extended) hydrodynamical model homology is reached, and the thermal explosion energy gets exhausted, at ~3 days, so these assumptions are not critical for the subsequent evolution.

The steady-state NLTE modelling is described in detail in J14, but it is worth to explain briefly how the macroscopic mixing is treated. As discussed in Sect. 3.3.10 a clumpy ejecta could be modelled in a simplified way if each nuclear burning zone is represented by a number of randomly distributed clumps, occupying some fraction of the core volume (filling factor). The global properties, as density and composition, then represent the mean of these quantities. In the current version, this model of macroscopic mixing is only implemented as a (globally) homogeneous spherical core, specified by the number of clumps and filling factors for each nuclear burning zone. Macroscopic mixing of material outside this core may however be represented as repeated sequences of spherical shells if needed. Macroscopic mixing is known to occur due to hydrodynamical instabilities in the explosion (Hammer et al. 2010), but the degree of it is uncertain and it is also quite different from microscopic mixing, as the nuclear burning zones retain their different compositions and may also end up with different densities. In this sense the steady-state NLTE modelling presented here and in J14, is quite different from that presented by Shivvers et al. (2013).

Figures 18 and 19 show the 100-500 days U to 4.5 μm and U to z model and observed pseudo-bolometric lightcurves. Figure 20 shows the 0-100 days model bolometric lightcurves calculated with the HDE code compared to the observed U to 4.5 μm pseudo-bolometric lightcurve. The model giving the best fit to the U to 4.5 μm and U to z pseudo-bolometric lightcurves is model 12C which, as discussed in J14, is also the model giving the best fit to the spectral evolution. This model has strong macroscopic mixing, local positron trapping, no molecule cooling, dust absorption/emission and an oxygen zone filling factor of 0.043. Below we discuss the effects of the degree of macroscopic mixing, oxygen zone filling factor and positron trapping on the lightcurves. The effects of molecule cooling and dust absorption/emission, is discussed in Sects. 4.3 and 4.2 respectively.

!Clearly we should also discussed the effect of changing the initial mass. However, I had some troubles processing this ejecta model with the HDE code so this have to wait until this problem is solved!

The degree of macroscopic mixing affects the lightcurves in several ways. Most important is the mixing of the Fe/Co zone containing the ^{56}Ni synthesized in the explosion and its decay products, determining the deposition of the radioactive decay energy in the ejecta. The mixing of the other zones, in turn determine the deposition of the radioactive decay energy in each of these zones. We have used two configurations, one where all core zones (Fe/Co-O/C) are randomly mixed within 3500 km s^{-1} (medium), and one that differs only in that 50 percent of Fe/Co material have been mixed out in the helium zone within 3500-6000 km s^{-1} (strong). As compared to the optimal model (12C), all models with medium mixing show a slower rise to peak luminosity. In Sect. 4.5 we show that the optimal hydrodynamical model also has strong outward mixing of the ^{56}Ni, which seems to be required to fit the rise to peak luminosity. As compared to the optimal model (12C), these models also have higher luminosity on the tail and in general do not give a good fit to the lightcurve. Clearly there is a large number of possible configurations that have not been investigated, e.g. a configuration with partial mixing of the core zones, as we found evidence for in

Sect. 3.3. Note that the size of the core of 3500 km s^{-1} is chosen to be intermediate between the estimated sizes of the oxygen and magnesium line emitting regions for SNe 2011dh, 1993J and 2008ax (Sects. 3.3.4, 3.3.6 and 3.3.11), to restrict the number of models.

The filling factors of each macroscopically mixed zone affects the lightcurves in several ways, but there are reasons to suspect that the effect could be quite small. In the optically thin limit, the deposition of radioactive decay energy does not depend on the filling factors, as the total cross section of each zone remains the same and, as shown in Kozma & Fransson (1992), the fraction of the deposited energy going into heating, ionization and excitation is not particularly sensitive to the density. We have used a number of configurations, where the filling factor of the oxygen zones ranges from small (0.043) to large (0.19), and adjusted the filling factors of the other zones accordingly. Comparing the pseudo-bolometric lightcurves of model 13C and 13E, which differs only in the oxygen zone filling factor, these are indeed very similar, but show a small difference increasing to ∼10 percent towards 500 days. The choice of a small oxygen zone filling factor is motivated by the better fit to the evolution of the [O I] 6300,6364 Å line (J14) !is this correct!. However, the value of 0.043, is consistent with the upper limit of ∼0.07 estimated from small scale variations in the [O I] 6300 and Mg I] 4571 Å lines (Sect. 3.3.10). Again there is a large number of possible configurations that have not been investigated.

The positron trapping only affects the lightcurves when the fraction of radioactive decay energy deposited by the positrons becomes significant, and before this models with locally trapped or free-streaming positrons are indistinguishable. As compared to model 12B, which differs only in that the positrons are free-streaming, the U to z pseudo-bolometric lightcurve of the optimal model (12C) has a higher decline rate and a lower luminosity after 300 days. The reason for this is that in the optimal model (12C) all positrons are trapped in the Fe/Co zone, and do not contribute to the heating of other zones, resulting in a lower luminosity in lines arising from these zones, in particular the strong [O I] 6300,6364 Å and Mg I] 4571 Å lines. The Fe/Co zone also has a lower temperature than other zones because of efficient cooling from the large number of iron lines, and the emission arising from this zone is redder. The difference in the U to MIR pseudo-bolometric lightcurve is not as pronounced, as the emission in mainly shifted from the optical to the NIR and MIR. The choice of local positron trapping for the optimal model (12C) is motivated by the better fit to the pseudo-bolometric lightcurves after 300 days, when the contribution from positrons to the deposited radioactive decay energy starts to become significant. However, further evidence is gained from the 678 day spectrum of SN 2011dh presented by Shivvers et al. (2013), which shows a dramatic change as compared to our last spectrum. All strong lines arising from other core zones than the Fe/Co zone, as the Mg I] 4571 Å, [O I] 6300,6364 Å and [Ca II] 7291,7323 Å lines, have disappeared or diminished dramatically, which is consistent with a scenario where all the positrons are being trapped locally in the Fe/Co zone.

4.2. Dust absorption and emission

As discussed in Sect. 3.2 and seen in Fig. 7, there is a strong increase in the fractional MIR luminosity between ∼100 and ∼200 days. As also discussed in Sect. 3.2 and seen in Fig. 5, there is a significant increase in the decline rates of the U to K pseudo-bolometric lightcurve between ∼100 and ∼200 days, even more

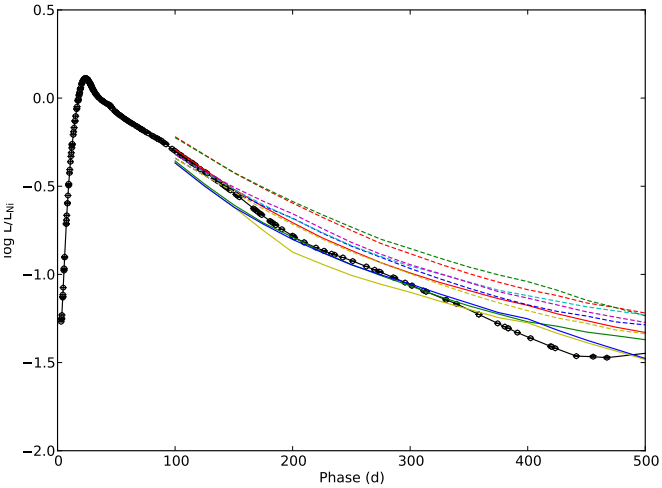

Fig. 18. 100-500 days U to 4.5 μm pseudo-bolometric lightcurves for the 12A (red solid line), 12B (green solid line), 12C (blue solid line), 13A (red short-dashed line), 13B (green short-dashed line), 13C (blue short-dashed line), 13D (yellow short-dashed line), 13E (magenta short-dashed line), 13F (cyan short-dashed line) and 17A (red long-dashed line) J14 models as compared to the observed U to 4.5 μm bolometric lightcurve (black dots and solid line). The lightcurves shown in this figure and Fig. 19 and 21 have been normalized to the radioactive decay chain luminosity of 0.075 $M_\odot$ of ^{56}Ni.

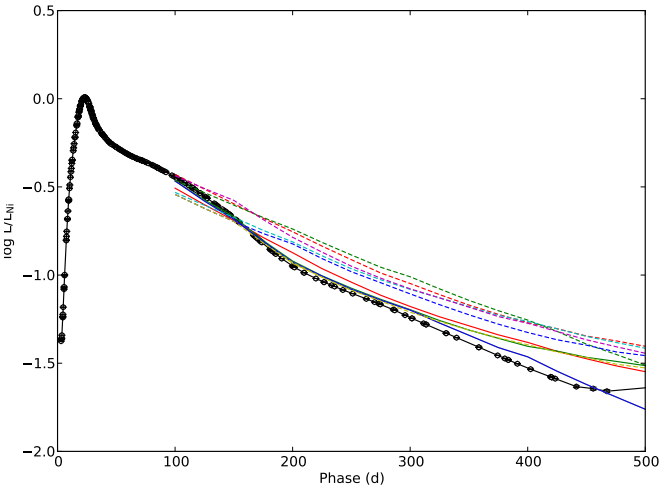

Fig. 19. 100-500 days U to z bolometric lightcurves for the J14 models as compared to the observed U to z bolometric lightcurve. The lightcurves are displayed as in Fig. 18 and have been normalized to the radioactive decay chain luminosity of 0.075 $M_\odot$ of ^{56}Ni.

pronounced in the U to z pseudo-bolometric lightcurve (Fig. 19), but less so in the U to 4.5 μm pseudo-bolometric lightcurve (Fig. 18). This suggests that some process is re-distributing flux from the optical and NIR to the MIR during this period. One example of such a process is dust formation in the ejecta, that would absorb the still quite hot radiation from the SN and re-emit it at a much lower temperature. However, a change of the lines dominating the cooling of the ejecta in some zone could cause a similar effect. As discussed in Sect. 3.2, an increasing excess in the MIR during this period is also seen in SN 1993J, but the corresponding increase in the decline rates of the U to K pseudo-bolometric lightcurve is not seen, which makes the interpretation less clear. However, circum stellar medium (CSM)

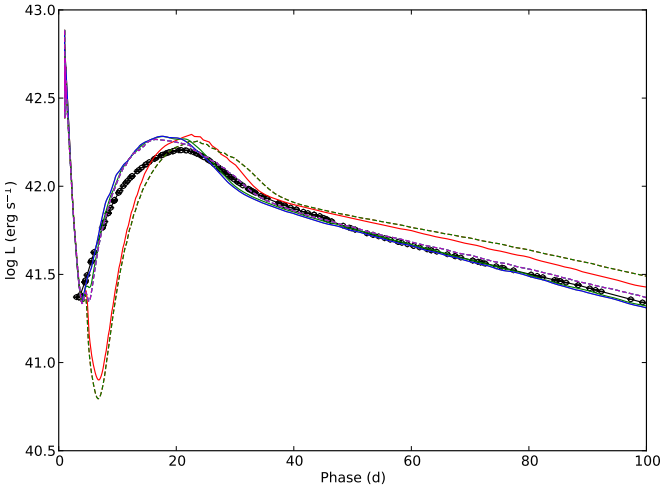

Fig. 20. 0-100 days bolometric lightcurves for the J14 models calculated with the HDE code as compared to the observed U to 4.5 μm bolometric lightcurve for the first 100 days. The lightcurves are displayed as in Fig. 18.

interaction that would affect the lightcurve in the opposite way, could be important for SN 1993J already at this early phase.

Dust is included in the modelling in a simplified way, and is represented as a gray absorptive opacity in the core (Fe/Co-O/C) zones. The absorbed luminosity is re-emitted as blackbody emission from a homologously expanding surface, representing a number of optically thick dust clouds. The fractional area of this surface x_{dust}, as compared to the area of the core, is a free parameter in the modelling, and determines the temperature of the emitted blackbody radiation. Note that our treatment of dust absorption and emission is only consistent if the number of dust clouds is large and the filling factor of those is small. At the temperatures expected for dust emission ($\lesssim$2000 K), the luminosity will be increased in the MIR and partly in the NIR, and decreased by a factor roughly equal to the total optical depth of the dust in the optical.

Using our simplified dust model, we find a value of 0.25 for the optical depth of the dust to match the behaviour of the optical lightcurves (see above). The value of x_{dust} was derived by minimization of the sum of squares of the relative flux differences of model and observed K, 3.6 and 4.5 μm photometry at 200, 300, 400 and 500 days (excluding K when the NIR coverage ends). This gives a value of x_{dust} of 0.01, which corresponds to temperatures of 2000, 1100, 666 and 416 K at 200, 300, 400 and 500 days respectively. However, assuming a large number of dust clouds and a small filling factor, it is possible to show from the assumptions made that $\tau = 3/4 x_{dust}$, so this value of x_{dust} is not consistent with our assumptions. Furthermore, as seen in Fig. 21, the evolution of the MIR bands is not well reproduced by the optimal model (12C), although the discrepancy is much worse for the same model without dust (12D). The discrepancy in the 4.5 μm band could possibly be explained by additional flux from the CO fundamental band, but the discrepancy in the 3.6 μm band will remain. Clearly the simplified dust model used is not good enough to well explain the MIR evolution, and further work is needed to better understand the evolution in these bands. On the other hand, as seen in Fig. 19, the optimal model (12C) gives a good fit to the evolution in the optical, in particular to the increased decline rates between 100 and 200 days, and does improve the discrepancy in the MIR considerably as compared to the same model without dust (12D).

As a further complication there might also be a contribution from heated CSM dust to the MIR emission. Helou et al. (2013) show that such a model could explain the early MIR evolution, whereas they fail to reproduce the late evolution. We have not investigated such models, but it is possible that a combination of emission from ejecta dust, CSM dust and molecules could well explain the MIR evolution. However, as the observational constraints are limited, it is not clear how to disentangle the contributions from these different sources from each other.

4.3. Molecule emission

As discussed in E14, there is an excess in the 4.5 μm band developing during the first hundred days, as compared to blackbody fits to the optical and NIR photometry. As seen in Fig. 8, this excess continues to develop after 100 days, and at ~600 days the 4.5 μm band is a factor of ~100 times brighter as compared to such a blackbody fit. Although the interpretation of a blackbody fit to nebular photometry is far from clear, we find a similar factor if we compare to synthetic photometry for the J14 models without dust absorption/emission and molecule cooling (Fig. 21). Clearly molecule (CO and SiO), dust or some other source of emission is needed to explain this discrepancy. However, even if we exclude other explanations, it is not easy to disentangle between a molecule and dust origin.

As discussed in Sect. 3.3.9, we detect CO first overtone emission at ~100 and ~200 days. This implies at least some contribution from CO fundamental band emission to the 4.5 μm flux. Knowledge of the fundamental to overtone band flux ratio would make an estimate of the contribution from fundamental band emission to the 4.5 μm flux possible. For SN 1987A this ratio was ~1 at 100 days, a few at 200 days, but increased dramatically to ~100 towards 500 days (Bouchet & Danziger 1993). As discussed in Sect. 3.3.9, we can set upper limits on the fundamental to overtone band flux ratio of ~15 and ~20 at ~100 and ~200 days respectively, so assuming the same flux ratios as for SN 1987A would suggest a minor contribution to the 4.5 μm flux from fundamental band emission at these epochs. However, this assumption is a bit dubious as the mass, density and composition of the ejecta is quite different for a Type IIb SN as compared to SN 1987A.

Molecule cooling is included in the modelling in a simplified way, and is represented as the fraction of the deposited radioactive decay energy emitted as molecule (CO and SiO) emission in the O/C and O/Si/S zones. This energy is then emitted as CO and SiO fundamental and first overtone band emission, represented as square line profiles with the typical widths of these emission bands. The CO first overtone band overlaps with the K band and the CO fundamental and SiO first overtone bands with the 4.5 μm band. The ratios of the fundamental and first overtone band emission are assumed to be the same as for SN 1987A (Bouchet & Danziger 1993). We have used two configurations, one where there the fraction of deposited radioactive decay energy emitted as molecule emission has been set to one, and one where this fraction has been set to zero.

Molecule cooling is an important parameter in the modelling, not only because it affects the flux in the K band and 4.5 μm bands. It also determines the fraction of the deposited radioactive decay energy available for line emission and the temperature in the O/C and O/Si/S zones. The observed CO first overtone emission at ~100 and ~200 days, implies that there is some molecule cooling in the O/C zone. Synthetic photometry on the J14 spectra for models with complete molecule cooling overproduce the 4.5 μm magnitudes (Fig. 21), suggesting the amount

of molecule cooling in the O/C zone to be modest. The strong similarity of the [O I] 6300 and Mg I] 4571 Å line profiles suggests the contribution from the O/C and O/Si/S zones to the [O I] 6300 Å emission to be modest, in turn suggesting the amount of molecule cooling in the O/C and O/Si/S zones to be significant. The redshift of the Ca II 8662 Å lines suggests a significant contribution from the [C I] 8727 Å line, found to arise mainly !is this correct! from the O/C in J14, in turn suggesting the amount of molecule cooling in the O/C zone to be modest. We have chosen no molecule cooling for our optimal model, but in the O/C zone an intermediate amount of cooling seems to be more likely.

4.4. Time dependent effects and 500-750 days bolometric lightcurve

Figure 22 shows the U to MIR and U to z pseudo-bolometric lightcurves compared to the bolometric lightcurve, deposited ^{56}Co decay gamma-ray and positron luminosity and deposited ^{57}Co decay luminosity for the optimal steady-state NLTE model (12C). The optimal hydrodynamical model produce very similar results. It is evident from the figure, that the deposited ^{56}Co decay luminosity is dominated by the positron contribution after ∼450 day, and that the observed 500-750 days pseudo-bolometric lightcurves are unlikely to be powered by the gamma-rays emitted in this decay. Shivvers et al. (2013) suggested that the SN has entered a phase powered by the positrons emitted in the ^{56}Co decay after 300-350 days. Given our results, this suggestion seems to be roughly correct in the sense that the positron contribution dominates the deposited luminosity after ∼450 days. However, as we will discuss below, it is not clear that the positron contribution dominates the emitted luminosity, because there is a number of processes that could provide additional energy sources.

There is observational evidence for additional energy sources from the observed pseudo-bolometric lightcurves. The decline rates of the pseudo-bolometric lightcurves between 500 and 750 days is 0.0065-0.0070 mag s^{-1}, significantly lower than the decay rate of ^{56}Co. As discussed in Sect. 4.1, our optimal model requires the positrons to be locally trapped to fit the 300-500 days U to z pseudo-bolometric lightcurve. This implies an increasing contribution from the low temperature Fe/Co zone (Sect. 4.1), in turn implying an increasing bolometric correction. However, the ratio of the observed U to z pseudo-bolometric luminosity and the bolometric luminosity of the optimal steady-state NLTE model, increases from ∼0.3 to ∼0.5 between 450 and 750 days, in contradiction with this expectation.

If the recombination time scales become longer than the time scale of the ^{56}Co decay, the steady-state assumption required for the NLTE modelling is no longer valid. Some fraction of the deposited radioactive decay energy will then build up a reservoir of ionization energy, which through recombination emission could eventually dominate the emitted luminosity. This process is called freeze-out and, as discussed in J14, approximate calculations suggest that freeze-out in the hydrogen-rich envelope occurs already at 100-200 days and in the helium envelope at ∼500 days !is this correct!. The contribution from the hydrogen envelope, which absorbs a negligible fraction of the radioactive decay energy, is likely to be small whereas the contribution from the helium envelope could very well be substantial. We use a time-dependent NLTE code (Kozma & Fransson 1992, 1998a,b) to test the steady-state assumption for our optimal steady-state NLTE model. Figure 23 shows the synthetic B, V, r and I band photometry, with and without a steady-state assumption, as modelled with this code. It is clear from the figure, that time-dependent effects starts to become important at ∼600 days, and after ∼700 days recombination emission from the helium envelope provide a dominant and increasing contribution to the flux in these bands. To determine if the additional energy source provided by freeze-out in the helium envelope can fully explain the late-time evolution of the pseudo-bolometric lightcurves is outside the scope of this paper, but it is clear that this contribution is likely to be substantial. The 678 day spectrum of SN 2011dh presented by Shivvers et al. (2013), show features not present in our last optical spectra that could be identified as the He I 6678 Å and 7065 Å lines, whereas the strong feature identified as Na I 5890,5896 by the authors could have a significant contribution from, or be fed by, the He I 5876 Å line. This is consistent with a substantial contribution from helium envelope recombination emission at this epoch.

CSM interaction became the dominant energy source at ∼300 days for SN 1993J !reference!, giving rise to broad box-like Hα and Na I 5890,5896 Å lines and a considerable flattening of the lightcurves. The 678 day spectra of SN 2011dh presented by Shivvers et al. (2013) show a feature that is interpreted as broad box-like Hα emission by the authors, but no broad box-like Na I 5890,5896 Å emission is seen. The interpretation of the broad feature as Hα emission is far from clear, as a number of other lines may contribute in this wavelength range (including the He I 6678 Å line discussed above), and the feature is also much weaker than for SN 1993J at a similar epoch. It is hard to exclude a contribution from CSM interaction to the emitted luminosity, but as the flatting of the lightcurve is seen in all optical bands as well as the MIR bands, and is actually least pronounced in the r band, we do not find it likely to be dominant.

Additional energy sources could also be provided by the decay of other radioactive isotopes than ^{56}Co. In the optimal steady-state NLTE model, the fractional luminosity deposited by the ^{57}Co decay is ∼10 percent at 700 days and increasing. A higher mass of ejected ^{57}Co than assumed in the optimal steady-state NLTE model, could not be excluded, and could help explain the observed evolution. The fractional luminosity deposited by the decay chain of ^{44}Ti in the optimal steady-state NLTE model is negligible, but contributions from other isotopes not included in the modelling could not be excluded.

4.5. Modelling of the 0-100 days bolometric lightcurve

In this section we use the HDE code to construct a model grid, from which the parameters giving the best fit to the bolometric lightcurve and the photospheric velocities is found by the use of a quantitative fitting procedure. This allows us to refine the discussion of the sensitivity of the derived quantities to errors in the observed quantities initiated in E14. It also allows us to fit the bolometric lightcurves of SNe 1993J and 2008ax using the same model grid and refine the discussion of the nature of their progenitors initiated in E14. We restrict the model grid to consist of bare helium core models without a hydrogen envelope and, as in B12, the diffusion phase and the early tail lightcurve and the photospheric velocities are used to determine the parameters of the helium core. We also make the assumption, justified for Type IIb SNe, that the helium core is not affected by mass loss. The thin hydrogen rich envelope only affects the bolometric lightcurve in the cooling phase and the parameters of this envelope has to be modelled separately. The details of the HDE code and all the caveats related to this type of modelling are discussed in Appendix A.

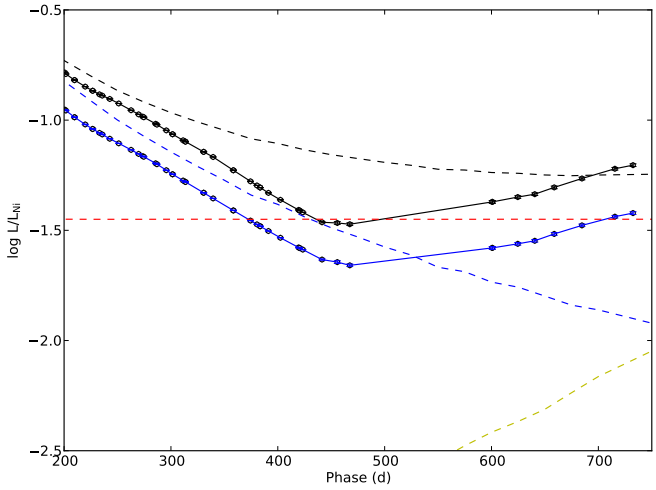

Fig. 22. U to MIR (black dots) and U to z (blue dots) pseudo-bolometric lightcurves compared to the bolometric lightcurve (black dashed line), deposited ^{56}Co decay gamma-ray (blue dashed line) and positron (red dashed line) luminosity and deposited ^{57}Co decay luminosity (yellow dashed line) for the optimal steady-state NLTE model (12C). The lightcurves have been normalized to the radioactive decay chain luminosity of 0.075 $M_\odot$ of ^{56}Ni.

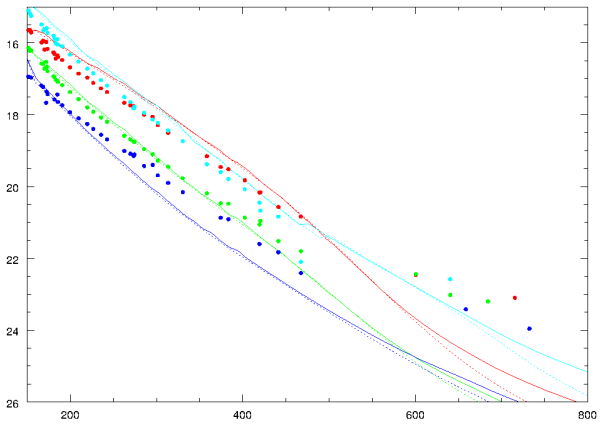

Fig. 23. Synthetic *B* (blue), *V* (yellow), *r* (red) and *I* (cyan) magnitudes for the optimal steady-state NLTE model (12C) as calculated with the time dependent NLTE code with (dashed lines) and without (solid lines) a steady-state assumption compared to the observed magnitudes (dots). !This figure has to be remade and does not show model 12C (but a similar model)!

!The original ide was to construct a model grid also for the cooling phase. However, this requires some work on how to parameterize and construct the thin hydrogen envelope. I think it is probably better to postpone this to a forthcoming paper where I plan to expand the sample of Type IIb SNe and possibly also make some other improvements in the hydrodynamical modelling and the underlying grid of stellar models. However, in Sect. 4.1 we refer to the optimal (extended) hydrodynamical model which currently is taken to be the original (extended) M_{He}=4.0 $M_\odot$ model from B12 processed with the HDE code. All this has to be clarified of course.!

The parameters varied are the mass of helium core M_{He}, the explosion energy E, the mass of ejected ^{56}Ni M_{Ni} and the distribution of it. The mass fraction of the ^{56}Ni is assumed to be a linearly declining function of mass becoming zero at some fraction of the total mass Mix_{Ni}. The parameter space spanned was M_{He}=2.5-6.5 $M_\odot$, E=0.5-2.0×10^{51} erg, M_{Ni}=0.02-0.2 $M_\odot$ and Mix_{Ni}=0.5-1.0 using a 10×10×10×10 grid. We find this resolution to be sufficient to safely interpolate intermediate values. The fitting is done by minimization of the square of the relative residuals, giving equal weight to the diffusion phase lightcurve (5-40 days), the tail lightcurve (40-100 days) and the early photospheric velocity evolution (5-40 days). As stellar models we have used solar metallicity STARS models (Stancliffe & Eldridge 2009), removing the hydrogen envelope and re-calculating the density profile using the constraints from hydrostatic and thermal equilibrium as described in B12 !Fix this!. As the HDE code does not include a network of nuclear reactions the explosive nucleosynthesis as a function of mass and explosion energy, except for the synthesized ^{56}Ni (see above), has been adopted from Woosley & Heger (2007) !Fix this! and linearly interpolated.

!The grid of stellar models currently consists of scaled versions of the M_{He}=4.0 $M_\odot$ model from B12 and the effect of explosive nucleo-synthesis is not included. This needs to be improved somehow. However, this is not likely change the conclusion sigificantly, at least not in some neigbourhood of the original M_{He}=4.0 $M_\odot$ model!

Figure 24 shows the model bolometric lightcurve and photospheric velocity evolution compared to the observed UV to MIR pseudo-bolometric lightcurve and velocity evolution for the absorption minimum of the Fe II 5169 Å line for the optimal models of SNe 2011dh, 2008ax and 1993J. The UV to MIR pseudo-bolometric lightcurves for SNe 2008ax and 1993J were constructed from the *U* to *K* pseudo-bolometric lightcurves assuming the same UV and MIR fractions as for SN 2011dh. Table 3 gives the helium core mass, explosion energy, mass of ejected ^{56}Ni and the distribution of it for the optimal models and the corresponding errors. The errors were calculated as the square root of the sum of the squared errors resulting from the errors in distance and extinction and a systematic error in the photospheric velocities. The derived parameters for SN 2011dh are in good agreement with the results in B12. The helium core mass and explosion energy derived for SNe 1993J and 2008ax are similar to what is derived for SN 2011dh, whereas the mass of ejected ^{56}Ni differs significantly. The ^{56}Ni is distributed far out in the ejecta for all three SNe. We note that the velocity evolution of SN 2008ax is not well fitted, which could be explained by a worse correspondence between the absorption minimum of Fe II 5169 Å and the photosphere as compared to SNe 2011dh and 1993J. Figure 25 shows contour plots of the relative error in the fit as a function of helium core mass and energy. These contour plots show that, as expected and discussed in E14, there is as a strong degeneracy in helium core mass and explosion energy if the fitting is done using the bolometric lightcurve alone. The constraint from the photospheric velocity evolution decrease this degeneracy significantly and the fit becomes quite robust. This means however that we expect the results to be quite sensitive to errors in the photospheric velocities.

!As is evident from the figures and the table we would probably need to extend the model grid to a bit lower explosion energies and to redefine the Mix_{Ni} parameter to allow for stronger mixing!

Measuring the sensitivity of the derived quantities to errors in the distance, extinction and a systematic error in the photospheric velocity, we indeed find the dependence of the helium core mass and explosion energy on the photospheric velocity to be strong. The dependence of helium core mass and explosion

energy on the distance and extinction, on the other hand, is weak although a higher extinction or larger distance tends to lower the helium core mass. The dependence of mass of the ejected ^{56}Ni on the distance and extinction is strong, whereas the dependence on the photospheric velocity is weak. In general we see that an error in the distance and extinction mainly corresponds to an error in the mass of ejected ^{56}Ni, whereas an error in the photospheric velocity mainly corresponds to an error in the helium core mass and explosion energy. The dependencies of the derived quantities on the distance and extinction are in agreement with the qualitative discussion in E14, but our model grid now makes it possible to quantify these as well as the dependencies on the photospheric velocity. As discussed in E14 we expect the mass of ejected ^{56}Ni to be proportional to the distance and, if we assume that the SED is peaking near the V band and the change in extinction is reasonably small, to be proportional to $10^{A_V/2.5}$. As the diffusion time depends on the ejecta mass and explosion energy as $\tau_{\rm d} \propto M_{\rm ej}^3/E$ and the velocity as $v^2 \propto E/M_{\rm ej}$, we expect the ejecta mass and explosion energy to depend on the photospheric velocity as $M_{\rm ej} \propto v_{\rm ph}$ and $E \propto v_{\rm ph}^3$. We find all of these approximate scalings to agree well with the measured sensitivity of the derived quantities.

To calculate the error bars for the derived quantities in Table 3, we have assumed a systematic error in the photospheric velocity of 15 percent. As discussed in E14, the photospheric radius as measured from the absorption minimum of the Fe II 5169 Å line could be overestimated by as much as ∼50 percent for SN 2011dh, if we treat the thermalization radius as estimated from blackbody fits to the photometry as a lower limit. Such an error would ruin our lower error bars on the mass and explosion energy, whereas the upper error bars would remain unchanged. However, such a ∼30 percent overestimate corresponds to a dilution factor (ratio between thermalization and photospheric radii) of 1.0, which is not particularly likely. Actually, the average observed dilution factor between 5 and 40 days of ∼0.75 equals the average model dilution factor (Sect. 5.1) between 5 and 25 days (where the thermalization radius disappears in the modelling). Although this argument is only indicative and the observed dilution factor is not known with better accuracy than the distance we find the 15 percent error used in the calculation reasonable.

We find a similar good agreement between average observed and model dilution factors for SN 1993J, but as discussed in Sect. 5.1, for SN 2008ax the average observed and model dilution factors is ∼0.5 and ∼0.8 respectively, and the observed blackbody temperature is also much higher than the model thermalization temperature. This is a clear indication that the adopted extinction is overestimated ,although the comparison has a number of caveats and other explanations are possible. As discussed above, the derived mass and explosion energy are weakly dependent on the adopted extinction, and the significant uncertainly in this quantity for SN 2008ax is included in the calculation of the error bars in Table 3. To get a better correspondence between observed and model dilution factors and temperatures, the extinction for SN 2008ax would need to be revised towards the lower error limit, which would correspond to an increase of the derived mass to ∼3.5 $M_\odot$!verify this!. The derived mass of the ejected ^{56}Ni on the other hand, would be very sensitive to such a revision and reduced with a factor of ∼2 !verify this! which, as discussed in E14, makes some sense as we find the other explosion parameters (helium core mass and explosion energy) to be similar to those of SN 2011dh.

!This issue is also discussed in the unfinished Sect. 5.1 and should maybe be expanded and moved to the discussion section

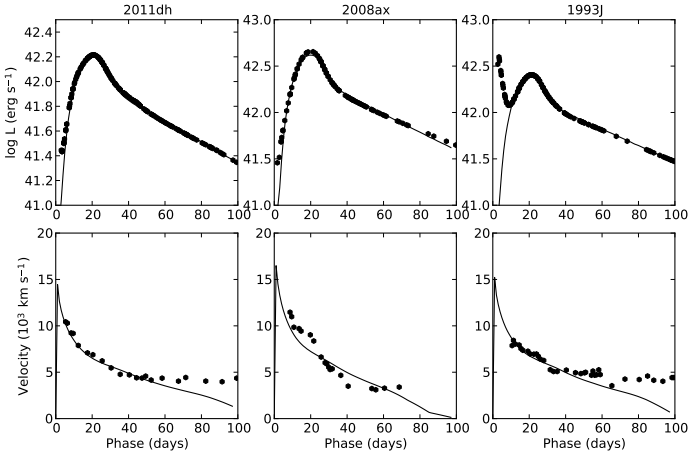

Fig. 24. Bolometric lightcurve (upper panels) and photospheric velocity evolution (lower panels) for the optimal models as compared to the observed UV to MIR pseudo-bolometric lightcurve and velocity evolution for the absorption minimum of the Fe II 5169 Å line for SNe 2011dh (left panels), 2008ax (middle panels) and 1993J (right panels).

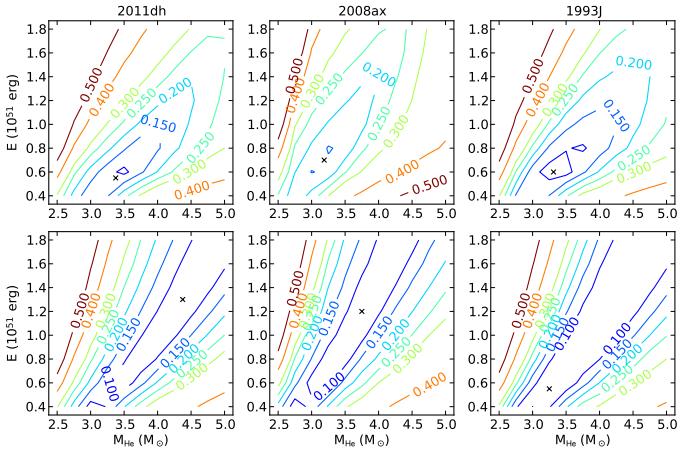

Fig. 25. Contour plots of the relative error in the fits as a function of mass and explosion energy for the case where the photospheric velocities were used (upper panels) and not used (lower panels) for SNe 2011dh (left panels), 2008ax (middle panels) and 1993J (right panels). !This plot needs to be improved, both estethically and with regards to the plotted quantities.!

as we can probably put further constraints on the extinction of SN 2008ax from athmosphere modelling (as for SN 2011dh in E14) as well as the steady-state NLTE modelling. On the other hand, as pointed out, the estimate of the helium core mass is not particulary sensitive to the adopted value of the extinction.!

4.6. Modelling of the 0-300 days bolometric lightcurve

In this section we extend the temporal coverage of the model grid described in Sect. 4.5 to 300 days (which is the period for which we have full U to 4.5 μm coverage), and make a fit of the observed U to 4.5 μm pseudo-bolometric lightcurve of SN 2011dh to the model grid, in a way similar to what was done in Sect. 4.5. The method used is to calculate the bolometric lightcurve after 100 days using the HDE code, assuming homologous expansion and instant emission of the energy deposited by the radioactive decay chains. However, to compare with the pseudo-bolometric lightcurve after 100 days, we also include a correction for the

Table 3. Helium core mass, explosion energy, mass of the ejected ^{56}Ni and the distribution of it for the optimal models of SNe 2011dh, 1993J and 2008ax.

SN	E (10^{51} erg)	M_{He} ($M_\odot$)	M_{Ni} ($M_\odot$)	Mix_{Ni}
2011dh	0.55 (+0.40,-0.16)	3.38 (+0.58,-0.32)	0.075 (+0.028,-0.017)	1.00 (+0.00,-0.00)
2008ax	0.70 (+0.50,-0.30)	3.19 (+0.56,-0.39)	0.175 (+0.087,-0.099)	0.93 (+0.05,-0.00)
1993J	0.60 (+0.45,-0.20)	3.31 (+0.64,-0.26)	0.106 (+0.034,-0.028)	0.90 (+0.12,-0.07)

flux within the U to 4.5 μm wavelength range, determined with the steady-state NLTE code. The fitting is done by minimization of the square of the relative residuals, giving equal weight to the diffusion phase lightcurve (5-40 days), the early tail lightcurve (40-100 days), the late tail lightcurve (100-300 days) and the early photospheric velocity evolution (5-40 days). This weighting scheme give less weight to the photospheric velocities, but this is also motivated as we have additional information about the lightcurve.

The correction for the flux within the U to 4.5 μm wavelength range was determined by evolving a strongly restricted set of the ejecta models with the steady-state NLTE modelling. In most of the parameter space spanned this correction did not vary much, and the number of ejecta models were chosen as small as possible to get a reasonable precision (~10 percent) using linear interpolations. To further restrict the number of ejecta models, we excluded those for which the average bolometric luminosity was more than 25 percent below the average observed U to 4.5 μm luminosity, using the lower error bars for the distance and extinction, as we know these would never make a good fit.

The method has its limitations and all the free parameters of the steady-state NLTE modelling which are not possible to map from the hydrodynamical modelling, as the degree of macroscopic mixing, the fraction of the energy going into molecule cooling in the O/C and O/Si zones and the amount of dust, have to be assigned some values. Here we have chosen to give these parameters the same values as for our optimal steady-state NLTE model (Sect. 4.1). On the other hand, the fractional flux within U to 4.5 μm does not vary much between the J14 ejecta models during the first 300 days, and as the optical depth to the γ-rays (and thus the deposited energy) depends on the ejecta mass as M^2/E, we don't expect the derived helium core mass to be very sensitive to changes in this fraction.

Figure 26 shows the model bolometric lightcurve and photospheric velocity evolution compared to the observed UV to MIR pseudo-bolometric lightcurve and velocity evolution for the absorption minimum of the Fe II 5169 Å line for the optimal model. The parameters of the optimal model are E=$0.55^{+0.40}_{-0.15}\times10^{51}$ erg, $M_{He}=3.38^{+0.58}_{-0.27}$ $M_\odot$, $M_{Ni}=0.075^{+0.028}_{-0.017}$ $M_\odot$ and $Mix_{Ni}=1.00^{+0.00}_{-0.00}$, in close agreement with the results from the 0-100 days bolometric lightcurve. Figure 26 also shows contour plots of the relative error in the fit as a function of helium core mass and energy. These are quite similar to those for the 0-100 days bolometric lightcurve shown in Fig. 25 so, a bit surprisingly, the additional information provided by the 100-300 days tail is not sufficient to give a robust fit without the use of the photospheric velocity evolution.

!Work in progress. The variation of the bolometric correction in parameter space is not yet included and we always use the bolometric correction from the optimal NLTE model!

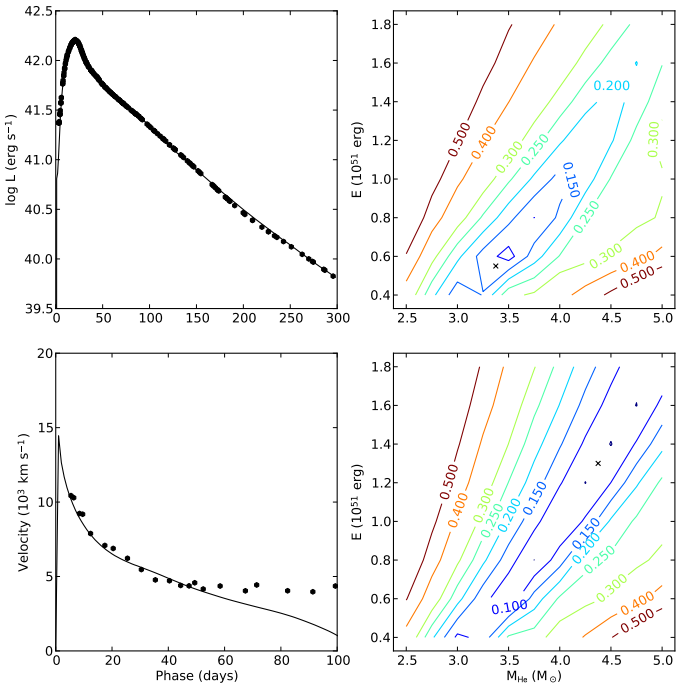

Fig. 26. Bolometric lightcurve (upper right panel) and photospheric velocity evolution (lower right panel) for the optimal model as compared to the observed UV to MIR pseudo-bolometric lightcurve and velocity evolution for the absorption minimum of the Fe II 5169 Å line. Contour plots of the relative error in the fit as a function of mass and explosion energy for the case where the photospheric velocities were used (upper left panel) and not used (lower left panel) are also shown. !This plot needs to be improved, both estethically and with regards to the plotted quantities.

5. Discussion

5.1. Physical interpretation of photometric and spectral evolution

In this section we discuss how the photometric and spectroscopic evolution could be understood given our optimal (extended) hydrodynamical model, a 3.5 $M_\odot$ helium core with a low-mass 270 $R_\odot$ envelope exploded with an energy of 0.6×10^{51} erg, ejecting 0.075 $M_\odot$ of ^{56}Ni. When the shock reaches the hydrogen rich envelope at ~10^2 seconds, the explosion energy is roughly equipartitioned between kinetic and thermal energy and the shock speed is ~2×10^4 km s^{-1}. In the nearly constant density envelope, the shock is decelerated to ~1×10^4 km s^{-1}, and when the radiation breaks out from the shock at ~10^4 seconds, almost all of the thermal energy deposited in the helium core has been lost

by expansion. About one tenth of the explosion energy is deposited in the hydrogen envelope, but even here equipartition is not reached, and at shock breakout only a small fraction of the explosion energy is in the form of thermal energy. Figure 27 shows the density and temperature profiles at shock breakout. Because of the deceleration of the shock, the hydrogen envelope has been strongly compressed and the temperature is high. In the three days that follows the hydrogen envelope will accelerate and expand and the temperature and luminosity at the photosphere, which are initially very high, will decrease rapidly because of expansion cooling and the short diffusion time for the radiation. This is the cooling phase seen in the early photometry published in Arcavi et al. (2011) and Tsvetkov et al. (2012).

The cooling phase ends at ∼3 days, when our observations begins, and is followed by the diffusion phase, which corresponds to the diffusion of the thermal energy deposited in the ejecta by the radioactive decay chain of ^{56}Ni, and was discussed in some detail in E14 as understood by approximate models (Arnett 1982; Imshennik & Popov 1992). In our optimal model of SN 2011dh the photosphere reaches the helium core at 4.5 days, after which the position of the photosphere is determined by the ionization front of helium, slowly moving inwards in mass coordinates but outwards in radial coordinates. Defining the thermalization radius as $\sqrt{3\tau_{abs}\tau_{tot}} = 2/3$ (Ensman & Burrows 1992), this is located near the outer edge of the ionization front of helium, and follows the evolution of this until ∼25 days, when helium recombines and the thermalization surface ceases to exist. In Fig. 28 we show the dilution factor (ratio of thermalization and photospheric radii) for the optimal bare helium core models for SNe 2011dh, 1993J and 2008ax compared to the observed dilution factor, as estimated from blackbody fits to the *VIJHK* photometry and the measured absorption minimum of the Fe II 5169 Å line. We also show the thermalization temperature compared to the observed temperature, as estimated from blackbody fits to the *VIJHK* photometry.

Before the temperature peak, the observed temperature of SNe 2011dh and 1993J is lower and the observed dilution factor higher than in the model, possibly because of the presence of the hydrogen envelope, but after this the agreement is good. The model temperatures and dilution factors for all SNe are fairly constant at ∼9000 K and ∼0.8 respectively. The observed temperature of SN 2008ax, on the other hand, is much higher and the observed dilution factor much lower. In the modelling the thermalization temperature is mainly determined by the ionization temperature of helium, and to reach a temperature above 15000 K at the center of the ionization front in a pure helium envelope requires a density higher than 10^{-9} g cm^{-3}, which is a factor of 100 above the canonical 10^{-11} g cm^{-3}. Although there is a number of caveats, as the variation of the thermalization radius and thus the temperature with wavelength (Dessart & Hillier 2005), and the relation between this temperature and a blackbody fit to the *VIJHK* photometry, we find the discrepancy intriguing. One obvious explanation is that the extinction adopted for SN 2008ax is overestimated, but other explanations as differences in density and composition might be possible as well.

!This section is work in progress!

5.2. The nature of the progenitor star

In M11, B12, E14, J14 and this paper we investigate the nature of the progenitor star using a number of different and, at least partially, independent methods. In M11 we analyse direct observations of the star by comparison of the observed magnitudes

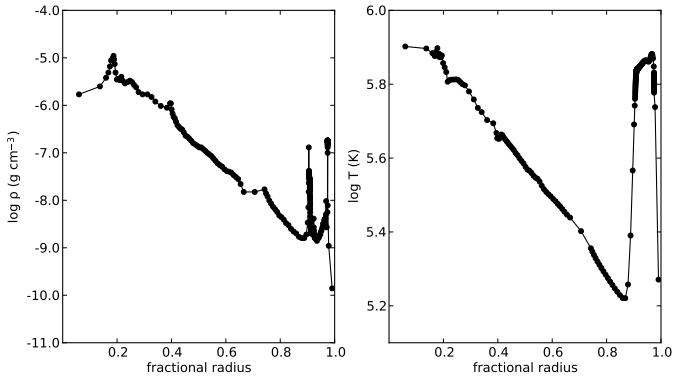

Fig. 27. Density (left panel) and temperature (right panel) profiles of the optimal (extended) hydrodynamical model for SN 2011dh at shock breakout.

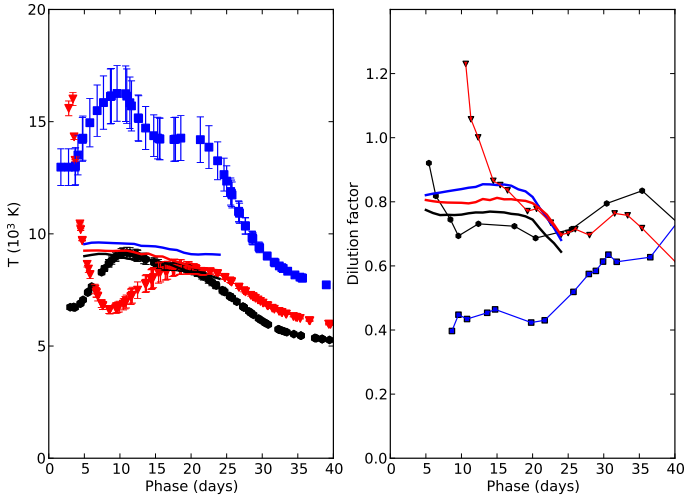

Fig. 28. Left panel: Observed blackbody temperature for SNe 2011dh (black dots), 1993J (red triangles) and 2008ax (blue squares) compared to the thermalization temperature as estimated from the hydrodynamical modelling (solid lines). Right panel: Observed dilution factor for SN 2011dh (black dots), 1993J (red triangles) and 2008ax (blue squares) compared to the dilution factor as estimated from the hydrodynamical modelling (solid lines).

to predictions from stellar atmosphere and evolutionary models. The best match is found to be a yellow supergiant with an initial mass of 13±3 M$_\odot$ and a radius of ∼270 R$_\odot$. In E14 we present observations of the disappearance of this star, thus confirming that it was the progenitor of SN 2011dh.

In B12 and this paper we present hydrodynamical modelling, which shows that a star with a helium core of $3.3^{+0.6}_{-0.2}$ M$_\odot$ and a low-mass (∼0.1 M$_\odot$) and extended (200-300 R$_\odot$) hydrogen-rich envelope, exploding with an energy of $0.50^{+0.42}_{-0.10}\times10^{51}$ erg and ejecting $0.075^{+0.028}_{-0.013}$ M$_\odot$ of ^{56}Ni, mixed out to high velocities, well reproduce the observed bolometric lightcurve for the first 100 days.

In J14 we present steady-state NLTE modelling of nebular spectra, which shows that a star with an initial mass of 12 M$_\odot$ well reproduce the observed spectral evolution, with particular focus on the [O I] 6300,6364 Å lines, which are very sensitive to the initial mass of the star. In this paper we find the optimal model from J14 to well reproduce the observed U to 4.5 μm and U to z pseudo-bolometric lightcurves between ∼100 and ∼450

days. After ∼450 days we cannot reproduce the observed evolution of the pseudo-bolometric lightcurves, but it is clear from modelling using a time-dependent NLTE code (Kozma & Fransson 1992, 1998a,b), that in this phase freeze-out in the helium envelope is important and the assumption of steady-state is no longer valid.

In E14 we estimate a hydrogen mass of 0.01-0.04 $M_\odot$ using a Monte-Carlo atmosphere code, in agreement with the 0.024 $M_\odot$ estimated by Arcavi et al. (2011), using a similar but more advanced code, that included a NLTE treatment of hydrogen and helium. This hydrogen mass is consistent with the B12 ejecta model, and we also find the interface between the helium core and the hydrogen rich envelope to be located at a velocity consistent with this model.

As proposed in E14 and shown in this paper, the sensitivity of the mass and explosion energy derived from the hydrodynamical modelling to the errors in distance and extinction is weak, and merely effects the derived mass of ejected ^{56}Ni. Although we have not scanned parameter space with the steady-state NLTE code, as this would be too computationally intensive, a similar conclusion is likely to hold for the initial mass as estimated from nebular spectra with the steady-state NLTE code. The fitting procedure for the hydrodynamical modelling used in this paper also allows us to quantify the sensitivity of the results to errors in the photospheric velocities and, including errors in all the observables, the upper bound on the initial mass is found to be ∼15 $M_\odot$.

Overall the results obtained with the different methods are consistent and, even given the caveats of each individual method, it is likely that the progenitor star is of moderate initial mass (12-15 $M_\odot$), and has a low-mass extended hydrogen rich envelope, of which most must have been lost either through stellar winds or interaction with a binary companion. The moderate mass suggests that interaction with a binary companion is needed, as stellar winds of stars in this mass range are not strong enough to expell the hydrogen envelope before core-collapse. As we show in J14 and in this paper, using steady-state NLTE modelling of nebular spectra and hydrodynamical modelling of the bolometric lightcurve, SNe 2008ax and 1993J are likely to be of similar initial mass and have similar explosion energy as SN 2011dh, although the mass of the ejected ^{56}Ni may differ significantly depending on the adopted distance and extinction. In particular, the upper bound on the initial mass for all three SNe is found to be ∼15 $M_\odot$. By the same reason as discussed above, this suggests that interaction with a binary companion have taken place. In the case of SN 1993J, this conclusion is supported by direct observations of the binary companion (Maund et al. 2004). Observations, that could detect or set useful constraints on the presence of a companion star for SN 2011dh, are scheduled for Cycle 21 at HST, whereas similar observations for SN 2008ax would not be feasible, because of the longer distance. Clearly there is growing evidence that the main production channel for Type IIb SNe are stars stripped on their hydrogen envelope by interaction with a binary companion. Modelling of the nebular spectra and hydrodynamical modelling of the bolometric lightcurves for a larger sample of Type IIb SNe, could provide further evidence for this hypothesis.

6. Conclusions

We present two years of optical and NIR photometric and spectroscopic observations for the Type IIb SN 2011dh. Together with SWIFT UV and Spitzer MIR data we build a UV to MIR pseudo-bolometric lightcurve covering ∼750 days, although the photometric coverage ends at ∼100 days in UV and at ∼350 days in NIR. The spectral coverage ends at ∼200 days in NIR and ∼450 days in the optical.

We use a steady-state NLTE code (Jerkstrand et al. 2011, 2012, 2014) to find an ejecta model, corresponding to a star of 12 $M_\odot$ initial mass, that well reproduce the 100-500 days U to 4.5 μm and U to z pseudo-bolometric lightcurves. A restricted set of ejecta models is used to explore the effects of changes in some of the free model parameters. Strong mixing of the Fe/Co zone material is required to reproduce the rise to peak luminosity as well as the tail luminosity, in agreement with the results from the hydrodynamical modelling. Local trapping of the positrons emitted in the ^{56}Co decay is required to fit the 300-500 days U to z pseudo-bolometric lightcurve. As discussed further below, a modest amount of dust formed in the ejecta and no cooling from molecules (CO and SiO) gives the best fit to the optical and MIR photometric evolution. Modelling with a time-dependent NLTE code (Kozma & Fransson 1992, 1998a,b) show that after ∼600 days the steady-state assumption is no longer valid.

The suggestion by Shivvers et al. (2013), that the SN has entered a phase powered by the positrons emitted in the ^{56}Co decay after 300-350 days, is found to be roughly correct in the sense that the positron deposition dominates the γ-ray deposition after ∼450 days in our optimal steady-state NLTE model. However, there is both observational and theoretical evidence that the emitted flux is dominated by additional energy sources. The decline rates of the 500-750 days pseudo-bolometric lightcurves are significantly lower than the decay rate of ^{56}Co and the observed optical luminosity is ∼50 percent of the bolometric luminosity in our optimal models, in contradiction with a scenario with locally trapped positron (see above). Modelling with the time-dependent NLTE code shows that after ∼600 days freeze-out in the helium envelope becomes important, and recombination emission from the helium envelope is likely to contribute substantially to the observed luminosity. We find a substantial contribution from CSM interaction and other radioactive isotopes less likely.

We use the hydrodynamical HDE code to build a model grid for the 3-100 days bolometric lightcurve, spanning a large volume of parameter space. This allows a quantitative fitting procedure as well as consistent modelling of SNe 2011dh, 1993J and 2008ax, taking into account the significant uncertainties in distance and extinction. Using this method, we find a helium core mass of $3.4^{+0.6}_{-0.3}$ $M_\odot$, an explosion energy of $0.55^{+0.40}_{-0.16}\times10^{51}$ erg and a mass of ejected ^{56}Ni of $0.075^{+0.028}_{-0.017}$ $M_\odot$, in agreement with our results from Bersten et al. (2012). For SNe 1993J and 2008ax we find values of the helium core mass and explosion energy similar to those of SN 2011dh, whereas the mass of ^{56}Ni depends sensitively on the adopted distance and extinction. The mass and explosion energy, on the other hand, are insensitive to changes in the distance and extinction, which is an important quality of the modelling. Strong mixing of the ejected ^{56}Ni is required for all three SNe to fit the rise to peak luminosity.

We also construct an extended model grid with temporal coverage up to 300 days by assuming instant emission of the energy deposited by the radioactive decay chains after 100 days. To compare with the observed U to 4.5 μm pseudo-bolometric lightcurve we determine the fractional flux within this wavelength range with the steady-state NLTE code. This allows us to combine the power of the hydrodynamical and steady-state NLTE modelling and the use of a quantitative fitting procedure. Applying this to the observed 3-300 days U to 4.5 μm pseudo-bolometric lightcurve of SN 2011dh, we find best fit values for the helium core mass, explosion energy, mass of ejected ^{56}Ni

and the distribution of it in good agreement with those based on the 3-100 days bolometric lightcurve.

We find an excess in the MIR as compared to steady-state NLTE model photometry developing between 100 and 200 days, during which an increase in the optical tail decline rates is also observed. This behaviour could be reproduced by the steady-state NLTE modelling if a modest amount of dust (τ = 0.25) is being continuously formed in the ejecta during this period, although the photometric evolution in the MIR is only partly reproduced. As discussed in E14 an excess develops in the 4.5 μm band already during the first 100 days, which is unlikely to be caused by dust forming in the ejecta. CO fundamental band emission or emission from heated CSM dust, as proposed by Helou et al. (2013), are possible explanations. We detect CO first overtone band emission in NIR spectroscopy at 89 and 202 days implying a contribution to the 4.5 μm band flux from CO fundamental band emission at these epochs. The photometric evolution in the MIR is complex and might involve components from CO, SiO, ejecta and CSM dust emission for which, at the best, only a simple and approximate treatment is included in the steady-state NLTE modelling.

We estimate the sizes of the oxygen, magnesium, iron and [Ca II] 7291,7323 Å line emitting regions to 2900-3400, 2700-3600, 1600-2100 and 2100-2400 km s^{-1} respectively, in all compared cases smaller than those of SNe 1993J and 2008ax. Given the findings in J14, these regions would correspond to the oxygen, O/Ne/Mg, Fe/Co and Si/S nuclear burning zones and suggest partial mixing of the core material. The profiles of the [O I] 6300 Å and Mg I] 4571 Å lines show a remarkable similarity, suggesting that these lines arise from the same nuclear burning zone. Given the findings in J14, this would be the O/Ne/Mg zone and contributions from the O/Si/S and O/C zones to the [O I] 6300 Å flux would be modest. This suggests the amount of molecule (CO and SiO) cooling in these zones to be considerable. On the other hand, the overproduction of 4.5 μm flux in models with complete molecule cooling as well as the (possible) presence of the [C I] 8727 Å line, suggests this amount to be modest. Our optimal steady state NLTE model has no molecule cooling but an intermediate amount is probably more likely.

We use repetitions of small scale fluctuations in the [O I] 6300 Å and [O I] 6364 Å lines to find a line ratio close 3, consistent with optically thin emission and in agreement with the results in J14, from 200 days and onwards. Applying the method of Chugai (1994) to these small scale fluctuations, we find an upper limit on the filling factor of the [O I] 6300 Å and Mg I] 4571 Å line emitting material of ~0.07 and a lower limit on the number of clumps of ~900. We also find the two strongest small scale features to repeat in the [O I] 5577 Å, O I 7774 Å and Na I 5890,5896 Å lines, suggesting these to be emitted, at least partly, by the same material. This is in agreement with the results in J14 where we find all these lines to have a significant contribution from the O/Ne/Mg zone.

We find a blue-shift of the center of flux of the [O I] 5577 Å, [O I] 6300 Å and Mg I] 4571 Å lines of ~1000 km s^{-1} or more decreasing towards zero at ~400 days. The evolution of the line profiles is well fitted by an absorptive continuum opacity in the line emitting region decreasing towards zero at 400 days, in agreement with the results in J14, where the cause of this opacity is found to be line-blocking in the core. SNe 1993J and 2008ax show a similar blue-shift of these lines, but contrary to SN 2011dh it saturates at ~500 km s^{-1} from 200 days and onwards. For SNe 2011dh and 2008ax we find no significant blue-shift of the oxygen and magnesium lines in the NIR. This gives support to the line-blocking hypothesis and disfavours an asymmetric distribution of the line emitting material towards the observer.

This paper concludes our observational and modelling work on SN 2011dh presented in M11, B12, E14 and J14. We have applied stellar evolutionary progenitor analysis, hydrodynamical modelling, SN atmosphere modelling and steady-state NLTE modelling to our extensive set of observational data. Although a number of issues remains unsolved, as the photometric evolution in the MIR and the late time flattening of the lightcurve, the main characteristics of the SN and its progenitor star found by the different methods are consistent. The progenitor star appears to have been of moderate (12-15 $M_\odot$) initial mass, and the 3-4 $M_\odot$ helium core surrounded by a low-mass (~0.1 $M_\odot$) and extended (200-300 $R_\odot$) hydrogen-rich envelope. In particular we have found the initial masses of SNe 2011dh, 1993J and 2008ax to be $\lesssim$15 $M_\odot$, from both hydrodynamical modelling of the early bolometric evolution and steady-state NLTE modelling of the late spectral evolution. This limit is also supported by stellar evolutionary progenitor analysis for SNe 2011dh and 1993J (Maund et al. 2004, 2011). Given that the mass-loss rates for stars in this mass range are probably not strong enough to expell the hydrogen envelope before core-collapse, a binary origin for these SNe is strongly suggested.

7. Acknowledgements

Appendix A: Hydrodynamical modelling

For the hydrodynamical modelling done in this paper we use the HDE code, similar in most aspects to the code used in B12 implementing the method described in Falk & Arnett (1977) and Bersten et al. (2011). The hydrodynamical conservation equations for mass, momentum and energy (Falk & Arnett 1977, eqs. 1-4) are solved by a finite difference scheme similar to the one described by Falk & Arnett (1977, eqs A1-A12) assuming that the radiative flux is given by the diffusion approximation (Falk & Arnett 1977, eq. 5). This is motivated in the optically thick regime but not in the optically thin regime where the radiation field is decoupled from the matter. In the optically thin regime we use a flux limiter following the prescription given by Bersten et al. (2011), being essentially a transformation of the radiation field from the optically thick to the optically thin limit. To handle strong velocity gradients (shocks) we use an artificial viscosity following the prescription by Von Neumann & Richtmyer (1950). The opacity is calculated from the OPAL opacity tables (Iglesias & Rogers 1996) complemented with the low temperature opacities given by Alexander & Ferguson (1994). These opacity tables are calculated for a non-expanding medium and therefore the bound-bound opacity, which is strongly dependent on the velocity field, is not applicable to SNe. To handle this we use, as discussed in Bersten et al. (2011), a minimum value of the opacity called opacity floor. The value of this floor is set to 0.01 cm^2 gram^{-1} in the hydrogen envelope and 0.025 cm^2 gram^{-1} in the helium core following B12 who calibrated these values by comparison to the STELLA hydrodynamical code (Blinnikov et al. 1998). The electron density needed in the equation of state is calculated by solving the Saha equation using the same atomic data as in Jerkstrand et al. (2011, 2012) !These data should be complemented with higher ionization stages!. The transfer of the gamma-rays and positrons emitted in the decay chain of ^{56}Ni is calculated with a Monte-Carlo method using the same gray opacities, luminosities and decay times as in Jerkstrand et al. (2011, 2012) and the heating rate then fed into the energy equation. The

code may also be run in homologous mode where the dynamics have been switched off and the energy equation is solved given the constraint of homologous expansion.

The momentum equation was written in explicit finite difference form as

$$\frac{\Delta v_k^n}{\Delta t^n} = -4\pi (r_k^n)^2 \frac{(\Delta P_k^n + \Delta Q_k^n)}{\Delta m_k} - \frac{G m_k}{(r_k^n)^2} \tag{A.1}$$

where

$$\begin{aligned} \Delta v_k^n &= v_k^{n+1/2} - v_k^{n-1/2} \\ \Delta P_k^n &= P_{k-1/2}^n - P_{k+1/2}^n \\ \Delta Q_k^n &= Q_{k+1/2}^n - Q_{k-1/2}^n \end{aligned} \tag{A.2}$$

and solved for $v_k^{n+1/2}$. The energy equation was written in implicit finite difference form as

$$\frac{\Delta E_{k+1/2}^{n+1/2}}{\Delta t^{n+1/2}} = \epsilon_{k+1/2}^{n+1/2} - (P_{k+1/2}^{n+1/2} + Q_{k+1/2}^{n+1/2}) \frac{\Delta V_{k+1/2}^{n+1/2}}{\Delta t^{n+1/2}} - \frac{\Delta L_{k+1/2}^{n+\theta}}{\Delta m_{k+1/2}} \tag{A.3}$$

where

$$\begin{aligned} \Delta E_{k+1/2}^{n+1/2} &= E_{k+1/2}^{n+1} - E_{k+1/2}^n \\ \Delta V_{k+1/2}^{n+1/2} &= V_{k+1/2}^{n+1} - V_{k+1/2}^n \\ \Delta L_{k+1/2}^{n+\theta} &= \theta (L_{k+1}^{n+1} - L_k^{n+1}) + (1-\theta)(L_{k+1}^n - L_k^n) \\ \epsilon_{k+1/2}^{n+1/2} &= (\epsilon_{k+1/2}^{n+1} + \epsilon_{k+1/2}^n)/2 \\ P_{k+1/2}^{n+1/2} &= (P_{k+1/2}^{n+1} + P_{k+1/2}^n)/2 \\ Q_{k+1/2}^{n+1/2} &= (Q_{k+1/2}^{n+1} + Q_{k+1/2}^n)/2 \end{aligned} \tag{A.4}$$

and solved for $T_{k-1/2}^{n+1}$, $T_{k+1/2}^{n+1}$ and $T_{k+3/2}^{n+1}$. This was achived by defining the quantity

$$D_{k+1/12}^{n+1/2} = \Delta E_{k+1/2}^{n+1/2} + (P_{k+1/2}^{n+1/2} + Q_{k+1/2}^{n+1/2}) \Delta V_{k+1/2}^{n+1/2} + \Delta L_{k+1/2}^{n+\theta} \frac{\Delta t^{n+1/2}}{\Delta m_{k+1/2}} \tag{A.5}$$

and finding the zero of this function by iteratively solving

$$\frac{\partial D_{k+1/2}^{n+1/2}}{\partial T_{k-1/2}^{n+1}} \delta T_{k-1/2}^{n+1} + \frac{\partial D_{k+1/2}^{n+1/2}}{\partial T_{k+1/2}^{n+1}} \delta T_{k+1/2}^{n+1} + \frac{\partial D_{k+1/2}^{n+1/2}}{\partial T_{k+3/2}^{n+1}} \delta T_{k+3/2}^{n+1} = D_{k+1/2}^{n+1/2} \tag{A.6}$$

for the temperature corrections $\delta T_{k-1/2}^{n+1}$, $\delta T_{k+1/2}^{n+1}$ and $\delta T_{k+3/2}^{n+1}$. The coefficients of this equation system constitutes a tridiagonal matrix which could be inverted by the use of standard methods.

References

Alexander, D. R. & Ferguson, J. W. 1994, ApJ, 437, 879
Arcavi, I., Gal-Yam, A., Yaron, O., et al. 2011, ApJ, 742, L18
Arnett, W. D. 1982, ApJ, 253, 785
Benvenuto, O. G., Bersten, M. C., & Nomoto, K. 2013, ApJ, 762, 74
Bersten, M. C., Benvenuto, O., & Hamuy, M. 2011, ApJ, 729, 61
Bersten, M. C., Benvenuto, O. G., Nomoto, K., et al. 2012, ApJ, 757, 31
Blinnikov, S. I., Eastman, R., Bartunov, O. S., Popolitov, V. A., & Woosley, S. E. 1998, ApJ, 496, 454
Bouchet, P. & Danziger, I. J. 1993, A&A, 273, 451
Chugai, N. N. 1994, ApJ, 428, L17
Dessart, L. & Hillier, D. J. 2005, A&A, 439, 671
Ensman, L. & Burrows, A. 1992, ApJ, 393, 742
Ergon, M., Sollerman, J., Fraser, M., et al. 2013, ArXiv e-prints
Falk, S. W. & Arnett, W. D. 1977, ApJS, 33, 515
Griga, T., Marulla, A., Grenier, A., et al. 2011, Central Bureau Electronic Telegrams, 2736, 1
Hammer, N. J., Janka, H.-T., & Müller, E. 2010, ApJ, 714, 1371
Helou, G., Kasliwal, M. M., Ofek, E. O., et al. 2013, ApJ, 778, L19
Iglesias, C. A. & Rogers, F. J. 1996, ApJ, 464, 943
Imshennik, V. S. & Popov, D. V. 1992, AZh, 69, 497
Jerkstrand, A., Ergon, M., Smartt, S., et al. 2014, In preparation
Jerkstrand, A., Fransson, C., & Kozma, C. 2011, A&A, 530, A45
Jerkstrand, A., Fransson, C., Maguire, K., et al. 2012, A&A, 546, A28
Kozma, C. & Fransson, C. 1992, ApJ, 390, 602
Kozma, C. & Fransson, C. 1998a, ApJ, 496, 946
Kozma, C. & Fransson, C. 1998b, ApJ, 497, 431
Matheson, T., Filippenko, A. V., Ho, L. C., Barth, A. J., & Leonard, D. C. 2000, AJ, 120, 1499
Maund, J. R., Fraser, M., Ergon, M., et al. 2011, ApJ, 739, L37
Maund, J. R., Smartt, S. J., Kudritzki, R. P., Podsiadlowski, P., & Gilmore, G. F. 2004, Nature, 427, 129
Maurer, I., Mazzali, P. A., Taubenberger, S., & Hachinger, S. 2010, MNRAS, 409, 1441
Milisavljevic, D. & Fesen, R. 2010, in Bulletin of the American Astronomical Society, Vol. 42, American Astronomical Society Meeting Abstracts #215, 454.05
Podsiadlowski, P., Hsu, J. J. L., Joss, P. C., & Ross, R. R. 1993, Nature, 364, 509
Sahu, D. K., Anupama, G. C., & Chakradhari, N. K. 2013, MNRAS, 433, 2
Shivvers, I., Mazzali, P., Silverman, J. M., et al. 2013, ArXiv e-prints
Stancliffe, R. J. & Eldridge, J. J. 2009, MNRAS, 396, 1699
Stathakis, R. A., Dopita, M. A., Cannon, R. D., & Sadler, E. M. 1991, Supernovae, 649
Stritzinger, M., Hamuy, M., Suntzeff, N. B., et al. 2002, AJ, 124, 2100
Taubenberger, S., Navasardyan, H., Maurer, J. I., et al. 2011, MNRAS, 413, 2140
Tsvetkov, D. Y., Volkov, I. M., Baklanov, P., Blinnikov, S., & Tuchin, O. 2009, Peremennye Zvezdy, 29, 2
Tsvetkov, D. Y., Volkov, I. M., Sorokina, E., et al. 2012, Peremennye Zvezdy, 32, 6
Valenti, S., Fraser, M., Benetti, S., et al. 2011, MNRAS, 416, 3138
Van Dyk, S. D., Li, W., Cenko, S. B., et al. 2011, ApJ, 741, L28
Van Dyk, S. D., Zheng, W., Clubb, K. I., et al. 2013, ApJ, 772, L32
Von Neumann, J. & Richtmyer, R. D. 1950, Appl. Phys., 21, 232
Woosley, S. E. & Heger, A. 2007, Phys. Rep., 442, 269
Yaron, O. & Gal-Yam, A. 2012, PASP, 124, 668

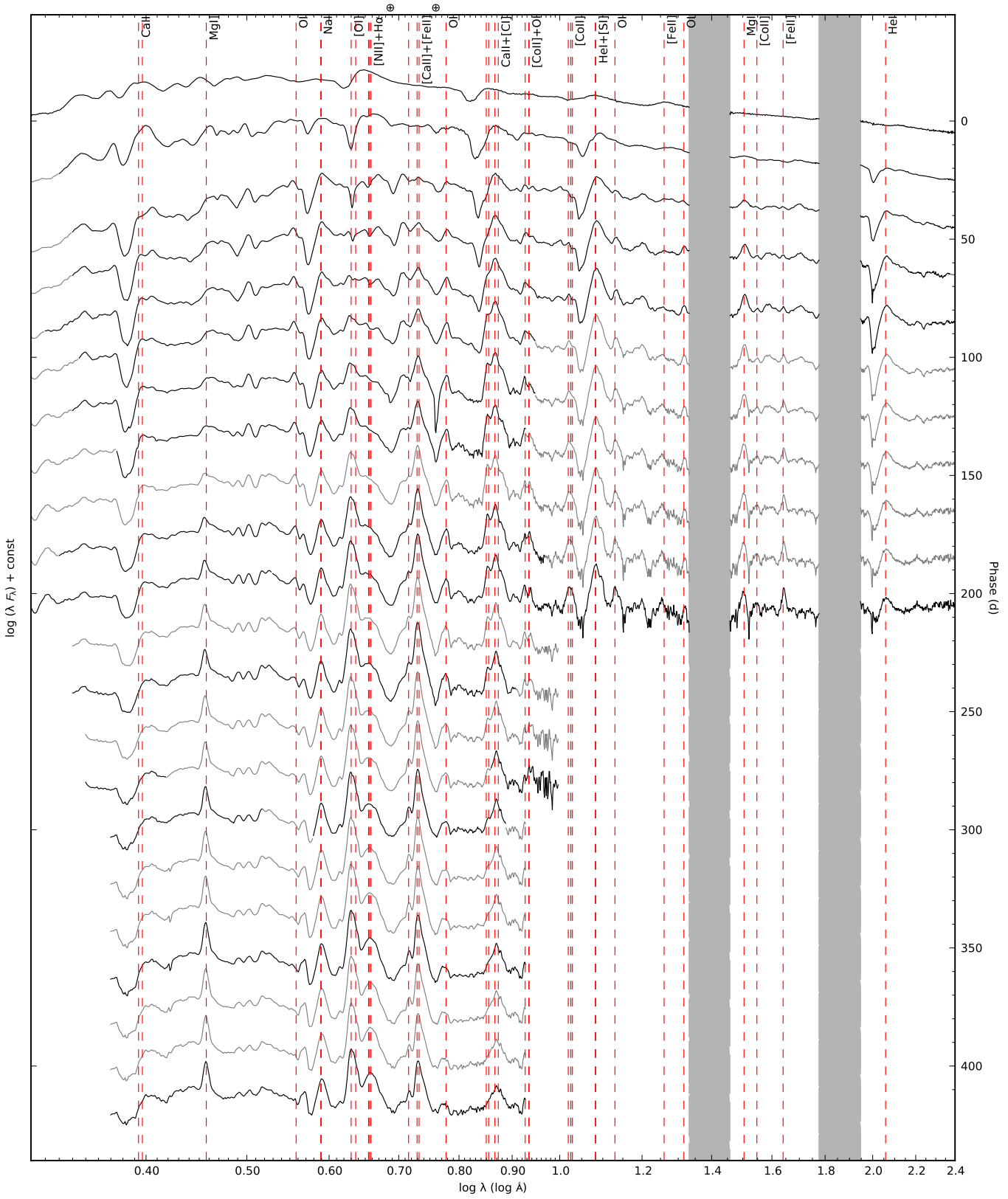

Fig. 2. Optical and NIR (interpolated) spectral evolution for SN 2011dh for days 5−425 with a 20-day sampling. Telluric absorption bands are marked with a ⊕ symbol in the optical and shown as grey regions in the NIR.

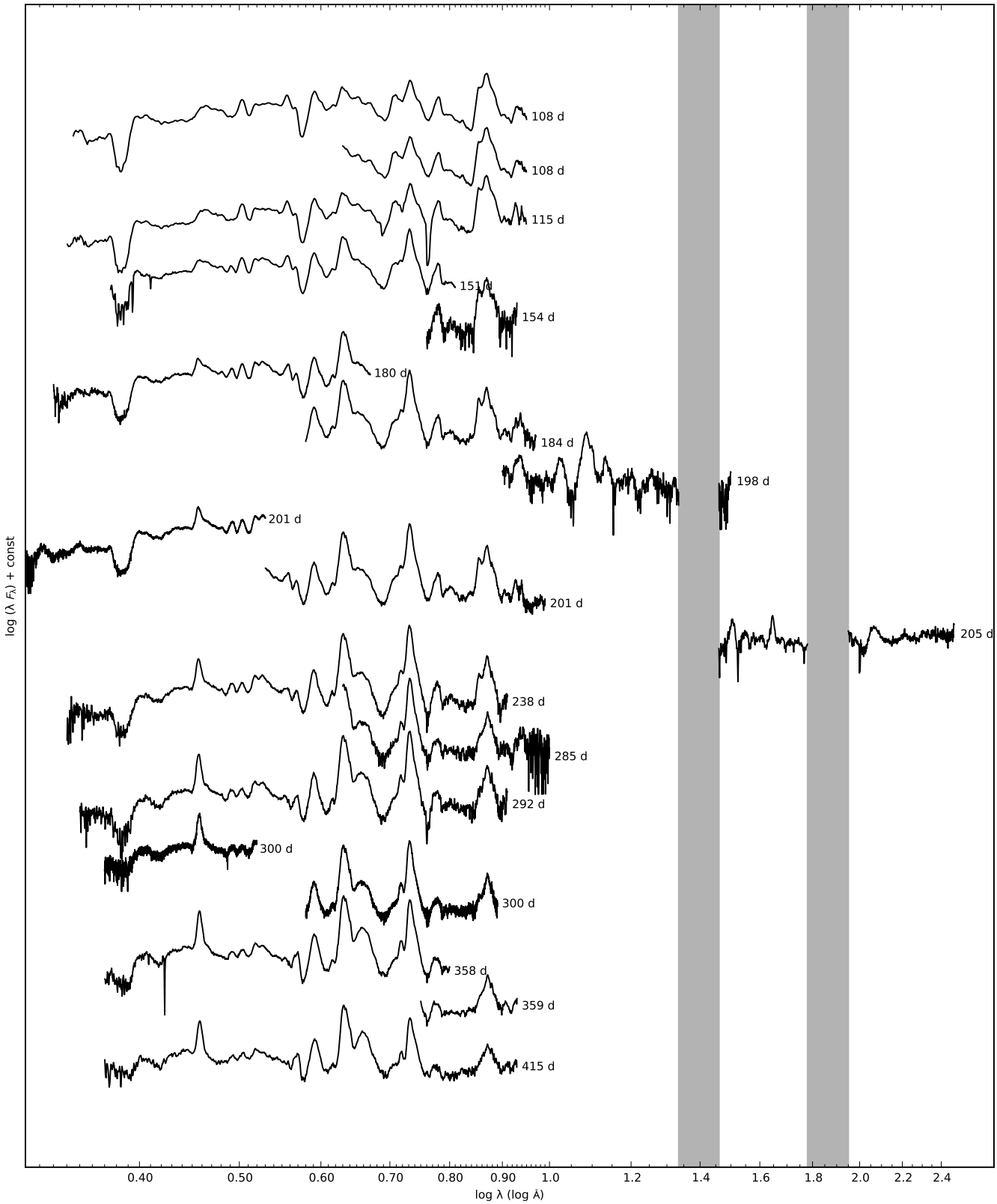

Fig. 3. Sequence of the observed late-time (100-415 days) spectra for SN 2011dh. Spectra obtained on the same night using the same telescope and instrument have been combined and each spectra have been labelled with the phase of the SN. Telluric absorption bands are marked with a ⊕ symbol in the optical and shown as grey regions in the NIR. !The AS-1.82/AFOSC spectra from 117 days is not yet included here.!

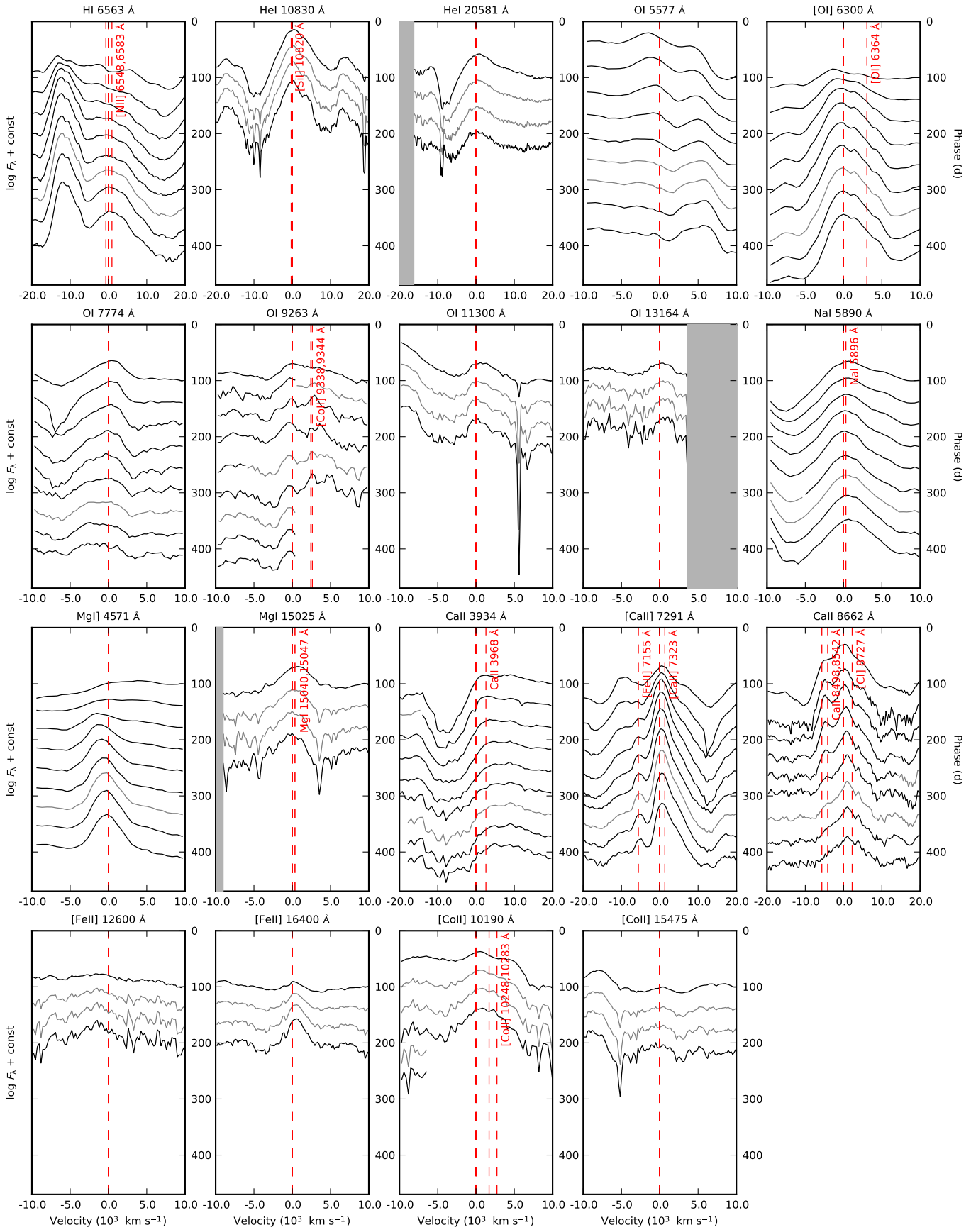

Fig. 9. Spectral evolution of all identified lines. Multiple or blended lines are marked with red dashed lines and telluric absorption bands in the NIR shown as grey regions.

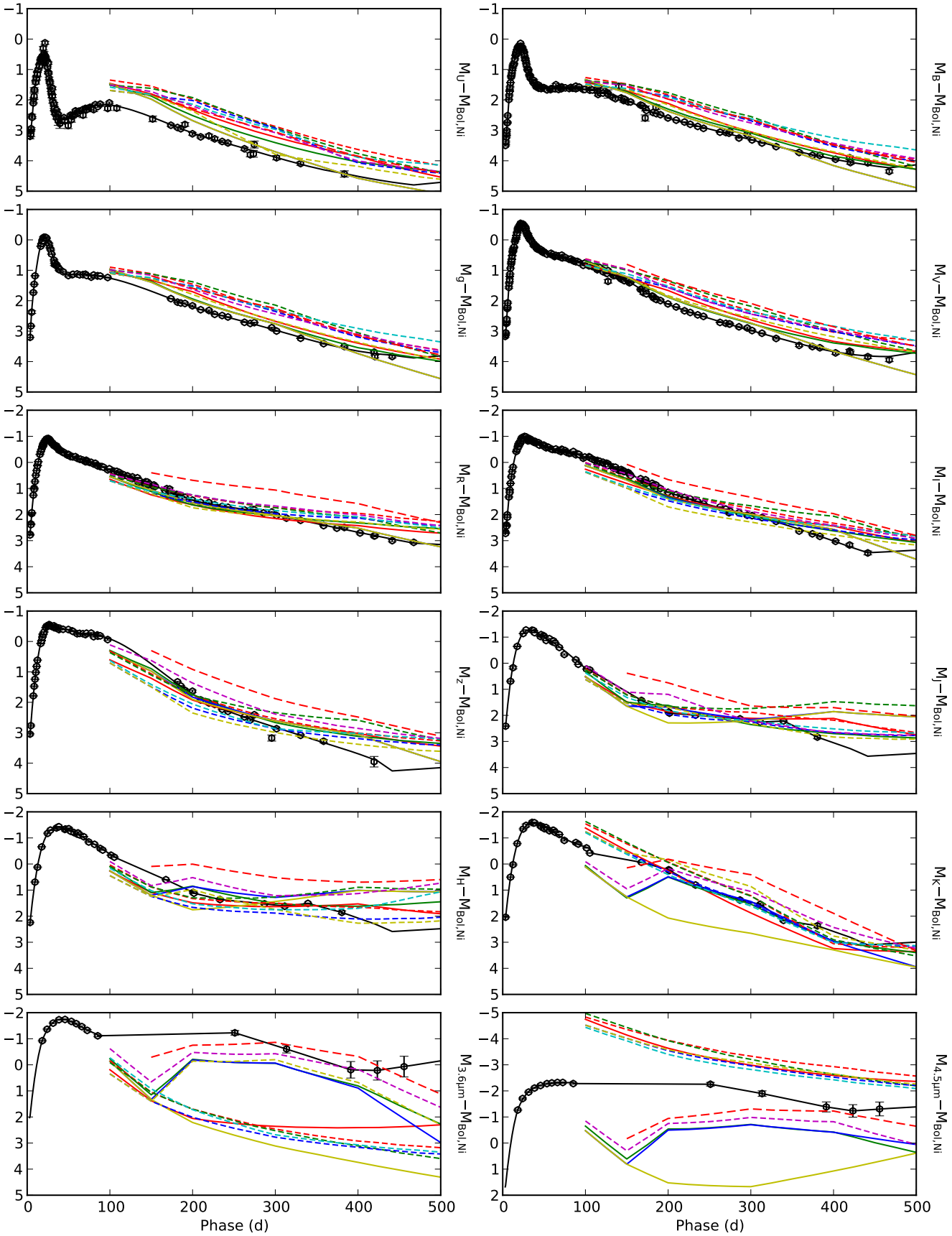

Fig. 21. Optical, NIR and MIR magnitudes for the J14 models as compared to the observed magnitudes. The lightcurves are displayed as in Fig. 18 and have been normalized to the radioactive decay chain luminosity of 0.075 $M_\odot$ of ^{56}Ni.

Table 4. Optical colour-corrected JC *U* and S-corrected JC *BVRI* magnitudes for SN 2011dh. Errors are given in parentheses. For completeness data for the first 100 days already published in E14 are included. !One AFOSC observations from 2011-11-20 is not yet included in the table.!

JD (+2400000) (d)	Phase (d)	*U* (mag)	*B* (mag)	*V* (mag)	*R* (mag)	*I* (mag)	Telescope (Instrument)
55716.43	3.43	14.99 (0.03)	15.35 (0.02)	14.92 (0.02)	14.54 (0.01)	14.41 (0.02)	LT (RATCam)
55716.43	3.43	15.15 (0.08)	15.39 (0.02)	14.94 (0.02)	14.57 (0.01)	14.46 (0.01)	TNG (LRS)
55717.43	4.43	15.03 (0.03)	15.14 (0.02)	14.67 (0.03)	14.25 (0.01)	14.26 (0.03)	LT (RATCam)
55717.48	4.48	15.17 (0.09)	15.21 (0.03)	14.63 (0.03)	14.24 (0.01)	14.23 (0.02)	AS-1.82m (AFOSC)
55717.48	4.48	...	15.12 (0.03)	14.63 (0.02)	14.27 (0.01)	14.28 (0.02)	CANTAB (BIGST8)
55718.48	5.48	...	14.84 (0.01)	14.28 (0.02)	13.94 (0.01)	13.94 (0.01)	LT (RATCam)
55718.57	5.57	14.68 (0.06)	14.84 (0.02)	14.24 (0.02)	13.91 (0.01)	14.04 (0.01)	CA-2.2m (CAFOS)
55720.42	7.42	14.42 (0.02)	14.25 (0.01)	13.75 (0.03)	13.41 (0.01)	13.43 (0.02)	LT (RATCam)
55721.42	8.42	14.28 (0.10)	14.02 (0.01)	13.48 (0.01)	13.22 (0.01)	13.24 (0.02)	LT (RATCam)
55721.43	8.43	14.07 (0.07)	14.06 (0.01)	13.60 (0.04)	13.27 (0.02)	13.34 (0.02)	NOT (ALFOSC)
55722.42	9.42	...	13.86 (0.01)	13.29 (0.01)	13.05 (0.01)	13.07 (0.01)	LT (RATCam)
55723.41	10.41	13.98 (0.06)	13.71 (0.01)	13.16 (0.01)	12.89 (0.01)	12.90 (0.01)	LT (RATCam)
55724.41	11.41	13.91 (0.08)	13.62 (0.01)	13.03 (0.01)	12.79 (0.01)	12.77 (0.01)	LT (RATCam)
55725.39	12.39	...	...	12.94 (0.02)	12.66 (0.01)	...	MONTCAB (BIGST8)
55725.43	12.43	13.88 (0.07)	13.52 (0.02)	12.92 (0.04)	12.68 (0.01)	12.68 (0.01)	LT (RATCam)
55726.36	13.36	...	13.52 (0.01)	12.91 (0.02)	12.59 (0.01)	...	MONTCAB (BIGST8)
55728.40	15.40	...	13.39 (0.01)	12.77 (0.01)	12.44 (0.01)	...	MONTCAB (BIGST8)
55729.39	16.39	13.65 (0.01)	13.35 (0.01)	12.77 (0.06)	12.39 (0.01)	12.35 (0.02)	LT (RATCam)
55730.40	17.40	13.64 (0.03)	13.33 (0.01)	12.66 (0.01)	12.36 (0.01)	12.32 (0.01)	LT (RATCam)
55731.41	18.41	13.74 (0.09)	13.30 (0.01)	12.60 (0.02)	12.31 (0.01)	12.27 (0.01)	LT (RATCam)
55731.82	18.82	...	...	...	12.33 (0.02)	12.25 (0.01)	FTN (FS02)
55732.40	19.40	...	13.35 (0.03)	12.61 (0.01)	12.27 (0.01)	12.21 (0.01)	CANTAB (BIGST8)
55732.41	19.41	13.44 (0.06)	13.36 (0.02)	12.64 (0.02)	12.33 (0.02)	12.31 (0.02)	NOT (ALFOSC)
55732.46	19.46	13.71 (0.07)	13.32 (0.01)	12.58 (0.01)	12.28 (0.02)	12.22 (0.01)	LT (RATCam)
55733.45	20.45	13.67 (0.07)	...	...	12.26 (0.01)	12.20 (0.02)	LT (RATCam)
55734.52	21.52	13.37 (0.05)	13.33 (0.01)	12.58 (0.01)	12.25 (0.01)	12.29 (0.01)	CA-2.2m (CAFOS)
55735.44	22.44	13.91 (0.04)	...	...	12.26 (0.01)	12.16 (0.01)	LT (RATCam)
55736.44	23.44	14.13 (0.08)	...	...	12.26 (0.01)	12.16 (0.01)	LT (RATCam)
55737.39	24.39	...	13.65 (0.01)	12.72 (0.01)	...	...	LT (RATCam)
55738.42	25.42	14.50 (0.04)	13.79 (0.02)	12.81 (0.01)	12.32 (0.02)	12.22 (0.01)	LT (RATCam)
55738.51	25.51	14.20 (0.04)	13.77 (0.02)	12.82 (0.01)	12.38 (0.01)	12.26 (0.01)	NOT (ALFOSC)
55739.43	26.43	14.73 (0.04)	13.95 (0.02)	12.88 (0.01)	12.38 (0.01)	12.23 (0.01)	LT (RATCam)
55740.36	27.36	...	14.09 (0.04)	12.93 (0.01)	12.45 (0.01)	12.29 (0.01)	MONTCAB (BIGST8)
55740.43	27.43	14.91 (0.03)	14.12 (0.01)	12.97 (0.01)	12.48 (0.01)	12.30 (0.01)	LT (RATCam)
55740.44	27.44	...	...	12.97 (0.01)	12.47 (0.01)	...	TJO (MEIA)
55741.44	28.44	...	...	...	12.54 (0.01)	12.32 (0.01)	LT (RATCam)
55742.49	29.49	15.33 (0.01)	...	...	12.62 (0.01)	12.40 (0.01)	LT (RATCam)
55743.41	30.41	...	14.53 (0.01)	13.27 (0.02)	...	...	LT (RATCam)
55743.42	30.42	15.18 (0.05)	14.51 (0.02)	...	12.65 (0.01)	12.53 (0.01)	CA-2.2m (CAFOS)
55743.42	30.42	15.43 (0.05)	14.53 (0.01)	13.26 (0.03)	12.68 (0.01)	12.49 (0.01)	NOT (ALFOSC)
55745.39	32.39	15.74 (0.03)	14.74 (0.01)	13.44 (0.01)	12.77 (0.01)	12.56 (0.01)	NOT (ALFOSC)
55745.44	32.44	15.93 (0.04)	...	...	12.81 (0.01)	12.53 (0.01)	LT (RATCam)
55745.80	32.80	...	...	...	12.80 (0.01)	12.51 (0.01)	FTN (FS02)
55746.45	33.45	16.07 (0.04)	14.87 (0.03)	13.51 (0.01)	12.83 (0.01)	12.55 (0.02)	LT (RATCam)
55747.44	34.44	16.12 (0.04)	...	...	12.89 (0.01)	12.59 (0.01)	LT (RATCam)
55748.43	35.43	16.02 (0.02)	14.97 (0.01)	13.62 (0.01)	12.88 (0.01)	12.65 (0.01)	NOT (ALFOSC)
55748.44	35.44	16.27 (0.04)	...	...	12.94 (0.01)	12.62 (0.01)	LT (RATCam)
55750.40	37.40	16.20 (0.04)	15.10 (0.01)	13.73 (0.01)	13.03 (0.01)	12.73 (0.01)	NOT (ALFOSC)
55750.42	37.42	16.41 (0.14)	15.11 (0.02)	13.78 (0.03)	13.03 (0.01)	12.73 (0.02)	LT (RATCam)
55751.41	38.41	...	15.14 (0.01)	13.81 (0.01)	13.08 (0.01)	12.73 (0.01)	TJO (MEIA)
55751.43	38.43	...	...	...	13.11 (0.01)	12.77 (0.01)	LT (RATCam)
55752.45	39.45	16.54 (0.16)	...	...	13.13 (0.01)	12.75 (0.01)	LT (RATCam)

Table 3. Continued.

JD (+2400000) (d)	Phase (d)	U (mag)	B (mag)	V (mag)	R (mag)	I (mag)	Telescope (Instrument)
55753.42	40.42	...	15.29 (0.01)	13.90 (0.02)	...	...	LT (RATCam)
55753.46	40.46	16.45 (0.05)	15.24 (0.01)	13.86 (0.01)	13.15 (0.01)	12.81 (0.01)	NOT (ALFOSC)
55755.40	42.40	16.42 (0.04)	15.30 (0.01)	13.96 (0.01)	13.23 (0.01)	12.89 (0.01)	NOT (ALFOSC)
55756.44	43.44	...	15.28 (0.02)	13.98 (0.02)	13.28 (0.02)	12.86 (0.01)	AS-Schmidt (SBIG)
55756.45	43.45	...	15.38 (0.02)	13.98 (0.01)	13.27 (0.03)	12.92 (0.01)	LT (RATCam)
55757.43	44.43	16.42 (0.04)	15.38 (0.01)	14.05 (0.01)	13.29 (0.01)	12.97 (0.01)	NOT (ALFOSC)
55759.45	46.45	...	15.44 (0.01)	14.06 (0.02)	...	...	LT (RATCam)
55761.40	48.40	...	15.44 (0.01)	14.17 (0.01)	13.44 (0.01)	13.02 (0.01)	AS-Schmidt (SBIG)
55762.41	49.41	...	15.45 (0.01)	14.16 (0.01)	13.44 (0.01)	13.06 (0.01)	NOT (ALFOSC)
55762.78	49.78	...	...	...	13.44 (0.01)	13.03 (0.01)	FTN (FS02)
55763.44	50.44	...	15.47 (0.01)	14.22 (0.01)	13.47 (0.01)	13.09 (0.01)	AS-Schmidt (SBIG)
55765.43	52.43	16.44 (0.03)	15.52 (0.01)	14.26 (0.01)	13.55 (0.01)	13.17 (0.01)	NOT (ALFOSC)
55767.43	54.43	16.50 (0.05)	...	...	13.58 (0.01)	13.16 (0.02)	LT (RATCam)
55768.45	55.45	16.48 (0.04)	...	...	13.60 (0.02)	13.19 (0.02)	LT (RATCam)
55771.40	58.40	16.37 (0.03)	15.58 (0.01)	14.32 (0.01)	13.62 (0.01)	13.28 (0.01)	CA-2.2m (CAFOS)
55773.39	60.39	16.45 (0.04)	15.60 (0.01)	14.38 (0.01)	13.71 (0.01)	13.32 (0.01)	NOT (ALFOSC)
55776.38	63.38	16.47 (0.04)	15.64 (0.01)	14.46 (0.01)	13.77 (0.01)	13.36 (0.01)	NOT (ALFOSC)
55777.33	64.33	...	15.52 (0.03)	14.46 (0.02)	13.78 (0.02)	13.34 (0.02)	AS-Schmidt (SBIG)
55780.40	67.40	16.42 (0.03)	15.65 (0.01)	14.50 (0.01)	13.85 (0.01)	13.43 (0.01)	NOT (ALFOSC)
55783.43	70.43	16.41 (0.03)	15.71 (0.01)	14.58 (0.01)	13.94 (0.01)	13.51 (0.01)	NOT (ALFOSC)
55784.33	71.33	...	15.66 (0.02)	14.59 (0.01)	...	13.43 (0.02)	AS-Schmidt (SBIG)
55784.39	71.39	16.45 (0.04)	15.66 (0.01)	14.52 (0.02)	13.90 (0.01)	13.47 (0.02)	CA-2.2m (CAFOS)
55784.77	71.77	...	...	...	13.93 (0.02)	13.45 (0.01)	FTN (FS02)
55785.36	72.36	...	15.70 (0.02)	14.61 (0.01)	13.96 (0.01)	13.45 (0.01)	AS-Schmidt (SBIG)
55788.41	75.41	...	...	...	14.02 (0.02)	13.52 (0.01)	AS-Schmidt (SBIG)
55790.38	77.38	16.45 (0.09)	...	...	14.03 (0.01)	13.61 (0.01)	LT (RATCam)
55793.37	80.37	16.55 (0.07)	15.80 (0.01)	14.74 (0.01)	14.13 (0.01)	13.67 (0.01)	NOT (ALFOSC)
55795.35	82.35	16.40 (0.04)	15.78 (0.01)	14.76 (0.01)	14.12 (0.01)	13.68 (0.01)	CA-2.2m (CAFOS)
55797.37	84.37	...	15.83 (0.02)	14.82 (0.01)	...	...	AS-Schmidt (SBIG)
55797.76	84.76	...	...	...	14.22 (0.01)	13.68 (0.01)	FTN (FS02)
55798.36	85.36	16.50 (0.03)	15.84 (0.01)	14.84 (0.01)	14.25 (0.01)	13.65 (0.02)	NOT (ALFOSC)
55799.33	86.33	...	15.82 (0.01)	14.86 (0.01)	...	...	AS-Schmidt (SBIG)
55801.36	88.36	16.44 (0.04)	15.89 (0.01)	14.90 (0.01)	14.31 (0.01)	13.80 (0.01)	NOT (ALFOSC)
55801.40	88.40	...	15.80 (0.02)	14.90 (0.01)	...	...	AS-Schmidt (SBIG)
55803.35	90.35	...	15.88 (0.02)	14.91 (0.01)	14.32 (0.01)	13.79 (0.01)	AS-Schmidt (SBIG)
55805.33	92.33	...	15.87 (0.02)	14.97 (0.02)	14.37 (0.01)	13.83 (0.01)	AS-Schmidt (SBIG)
55810.34	97.34	16.68 (0.06)	16.00 (0.01)	15.11 (0.01)	14.52 (0.01)	14.02 (0.01)	NOT (ALFOSC)
55812.33	99.33	16.51 (0.03)	16.02 (0.01)	15.05 (0.01)	14.49 (0.01)	14.00 (0.01)	CA-2.2m (CAFOS)
55817.35	104.35	...	16.02 (0.03)	15.19 (0.02)	14.63 (0.02)	14.04 (0.02)	AS-Schmidt (SBIG)
55818.33	105.33	...	16.10 (0.02)	15.19 (0.02)	14.66 (0.01)	14.08 (0.01)	AS-Schmidt (SBIG)
55821.31	108.31	16.77 (0.08)	16.12 (0.02)	15.25 (0.01)	14.68 (0.01)	14.16 (0.01)	CA-2.2m (CAFOS)
55824.32	111.32	...	...	15.31 (0.02)	14.75 (0.03)	14.24 (0.03)	AS-Schmidt (SBIG)
55827.33	114.33	...	16.16 (0.03)	15.42 (0.01)	14.87 (0.02)	14.27 (0.01)	AS-Schmidt (SBIG)
55827.48	114.48	...	16.22 (0.07)	15.37 (0.03)	14.94 (0.05)	14.38 (0.05)	AT (ANDOR)
55828.27	115.27	...	16.34 (0.04)	15.39 (0.02)	14.86 (0.02)	14.31 (0.01)	AT (ANDOR)
55830.28	117.28	...	16.30 (0.02)	15.38 (0.01)	14.91 (0.01)	14.34 (0.01)	AS-1.82m (AFOSC)
55834.26	121.26	...	16.23 (0.03)	15.49 (0.02)	14.99 (0.02)	14.44 (0.02)	AT (ANDOR)
55834.31	121.31	...	16.35 (0.02)	15.55 (0.01)	14.99 (0.02)	14.41 (0.02)	AS-Schmidt (SBIG)
55838.34	125.34	...	...	15.64 (0.02)	15.11 (0.03)	14.49 (0.01)	AS-Schmidt (SBIG)
55839.28	126.28	...	16.39 (0.03)	15.65 (0.02)	15.12 (0.02)	14.52 (0.02)	AS-Schmidt (SBIG)
55840.26	127.26	...	16.44 (0.03)	15.57 (0.02)	15.15 (0.03)	14.53 (0.02)	AT (ANDOR)
55840.30	127.30	...	16.44 (0.14)	15.93 (0.06)	15.08 (0.04)	14.59 (0.04)	AS-Schmidt (SBIG)

Table 3. Continued.

JD (+2400000) (d)	Phase (d)	U (mag)	B (mag)	V (mag)	R (mag)	I (mag)	Telescope (Instrument)
55846.26	133.26	...	16.60 (0.03)	15.77 (0.02)	15.17 (0.02)	14.71 (0.02)	AT (ANDOR)
55847.30	134.30	...	...	15.81 (0.02)	15.35 (0.03)	14.77 (0.02)	AT (ANDOR)
55849.26	136.26	...	16.68 (0.05)	15.81 (0.02)	15.33 (0.03)	14.75 (0.02)	AT (ANDOR)
55853.27	140.27	...	16.32 (0.06)	15.90 (0.05)	15.44 (0.05)	14.91 (0.04)	AS-Schmidt (SBIG)
55855.38	142.38	...	...	15.96 (0.03)	15.44 (0.03)	14.93 (0.03)	AT (ANDOR)
55856.24	143.24	...	16.72 (0.06)	16.01 (0.03)	15.42 (0.02)	14.91 (0.02)	AT (ANDOR)
55858.29	145.29	...	...	16.02 (0.03)	15.45 (0.03)	14.96 (0.02)	AT (ANDOR)
55859.23	146.23	...	16.84 (0.05)	16.08 (0.02)	15.56 (0.03)	15.01 (0.02)	AT (ANDOR)
55860.22	147.22	...	16.80 (0.05)	16.10 (0.03)	15.53 (0.03)	15.02 (0.02)	AT (ANDOR)
55864.69	151.69	17.55 (0.09)	16.94 (0.02)	16.14 (0.01)	15.65 (0.01)	15.10 (0.01)	AS-1.82m (AFOSC)
55866.28	153.28	...	...	16.23 (0.02)	15.64 (0.03)	15.18 (0.02)	AT (ANDOR)
55867.70	154.70	...	16.97 (0.02)	16.21 (0.03)	15.71 (0.02)	15.25 (0.02)	CA-2.2m (CAFOS)
55879.66	166.66	...	17.19 (0.03)	16.58 (0.02)	15.99 (0.02)	15.49 (0.02)	AS-Schmidt (SBIG)
55881.74	168.74	...	17.23 (0.02)	16.59 (0.02)	15.94 (0.01)	15.66 (0.03)	CA-2.2m (CAFOS)
55883.24	170.24	...	...	16.72 (0.05)	16.19 (0.05)	15.61 (0.02)	AT (ANDOR)
55885.21	172.21	...	17.67 (0.10)	16.53 (0.03)	15.98 (0.05)	15.62 (0.03)	AT (ANDOR)
55885.73	172.73	...	17.36 (0.08)	16.67 (0.02)	...	15.59 (0.03)	AS-1.82m (AFOSC)
55886.75	173.75	17.97 (0.03)	17.43 (0.01)	16.79 (0.01)	16.17 (0.01)	15.73 (0.01)	NOT (ALFOSC)
55893.71	180.71	...	...	16.93 (0.02)	16.27 (0.01)	15.80 (0.02)	AS-Schmidt (SBIG)
55894.76	181.76	18.12 (0.03)	17.58 (0.01)	16.96 (0.01)	16.31 (0.01)	15.89 (0.01)	NOT (ALFOSC)
55896.20	183.20	...	...	17.03 (0.05)	16.44 (0.06)	16.01 (0.04)	AT (ANDOR)
55898.19	185.19	...	17.44 (0.08)	17.06 (0.04)	16.35 (0.04)	15.90 (0.03)	AT (ANDOR)
55898.73	185.73	18.20 (0.04)	17.65 (0.01)	17.09 (0.01)	16.39 (0.01)	16.05 (0.01)	NOT (ALFOSC)
55903.76	190.76	18.11 (0.06)	17.74 (0.02)	17.18 (0.02)	16.48 (0.01)	16.10 (0.02)	NOT (ALFOSC)
55912.79	199.79	18.51 (0.05)	17.93 (0.02)	17.37 (0.01)	16.68 (0.01)	16.33 (0.01)	NOT (ALFOSC)
55922.76	209.76	18.70 (0.03)	18.10 (0.01)	17.57 (0.01)	16.86 (0.01)	16.52 (0.01)	NOT (ALFOSC)
55932.79	219.79	18.77 (0.06)	18.26 (0.01)	17.80 (0.02)	16.97 (0.02)	16.72 (0.02)	NOT (ALFOSC)
55939.73	226.73	18.93 (0.05)	18.40 (0.02)	17.92 (0.02)	17.12 (0.01)	16.85 (0.01)	NOT (ALFOSC)
55948.73	235.73	19.11 (0.04)	18.56 (0.01)	18.08 (0.01)	17.27 (0.01)	17.04 (0.01)	NOT (ALFOSC)
55955.76	242.76	19.23 (0.04)	18.69 (0.01)	18.20 (0.01)	17.37 (0.01)	17.19 (0.01)	NOT (ALFOSC)
55975.69	262.69	19.61 (0.05)	19.01 (0.01)	18.59 (0.01)	17.67 (0.01)	17.51 (0.01)	NOT (ALFOSC)
55982.74	269.74	19.88 (0.07)	19.09 (0.02)	18.69 (0.02)	17.74 (0.01)	17.65 (0.01)	NOT (ALFOSC)
55986.62	273.62	19.88 (0.11)	19.15 (0.03)	18.75 (0.03)	17.76 (0.02)	17.83 (0.03)	CA-2.2m (CAFOS)
55987.62	274.62	19.59 (0.12)	19.11 (0.02)	18.76 (0.02)	17.78 (0.01)	17.78 (0.01)	LT (RATCam)
55998.67	285.67	...	19.43 (0.02)	18.96 (0.02)	18.00 (0.01)	17.95 (0.01)	NOT (ALFOSC)
56008.66	295.66	...	19.40 (0.03)	19.10 (0.03)	18.06 (0.02)	18.14 (0.03)	LT (RATCam)
56014.51	301.51	20.28 (0.07)	19.65 (0.01)	19.24 (0.02)	18.26 (0.01)	18.22 (0.01)	NOT (ALFOSC)
56026.49	313.49	...	19.86 (0.02)	19.44 (0.02)	18.47 (0.01)	18.41 (0.02)	NOT (ALFOSC)
56043.59	330.59	20.76 (0.06)	20.15 (0.02)	19.78 (0.02)	18.72 (0.01)	18.72 (0.02)	NOT (ALFOSC)
56071.42	358.42	...	20.61 (0.02)	20.28 (0.04)	19.20 (0.02)	19.36 (0.03)	NOT (ALFOSC)
56087.43	374.43	...	20.86 (0.02)	20.48 (0.03)	19.45 (0.02)	19.62 (0.02)	NOT (ALFOSC)
56096.48	383.48	21.62 (0.10)	20.95 (0.03)	20.60 (0.04)	19.51 (0.02)	19.81 (0.03)	NOT (ALFOSC)
56115.44	402.44	...	21.26 (0.03)	20.96 (0.05)	19.91 (0.02)	20.18 (0.04)	NOT (ALFOSC)
56132.43	419.43	...	21.38 (0.06)	21.07 (0.06)	20.19 (0.03)	20.49 (0.05)	NOT (ALFOSC)
56133.40	420.40	...	21.55 (0.05)	21.13 (0.06)	20.19 (0.03)	...	NOT (ALFOSC)
56154.39	441.39	...	21.76 (0.05)	21.46 (0.06)	20.58 (0.04)	21.01 (0.08)	NOT (ALFOSC)
56180.37	467.37	...	22.30 (0.05)	21.82 (0.06)	20.90 (0.04)	...	NOT (ALFOSC)
56313.73	600.73	...	...	22.44 (0.10)	...	...	NOT (ALFOSC)
56353.50	640.50	...	...	23.02 (0.00)	...	22.58 (0.00)	HST (ACS)
56371.69	658.69	...	23.42 (0.32)	...	...	...	NOT (ALFOSC)
56397.64	684.64	...	...	23.20 (0.20)	...	...	NOT (ALFOSC)
56445.43	732.43	...	23.96 (0.50)	...	...	...	NOT (ALFOSC)

Table 4. Optical colour-corrected SDSS *u* and S-corrected SDSS *griz* magnitudes for SN 2011dh. Errors are given in parentheses. For completeness data for the first 100 days already published in E14 are included.

JD (+2400000) (d)	Phase (d)	*u* (mag)	*g* (mag)	*r* (mag)	*i* (mag)	*z* (mag)	Telescope (Instrument)
55716.47	3.47	15.90 (0.03)	15.08 (0.01)	14.68 (0.01)	14.80 (0.01)	14.76 (0.02)	LT (RATCam)
55717.46	4.46	16.01 (0.03)	14.80 (0.01)	14.38 (0.01)	14.61 (0.01)	14.58 (0.02)	LT (RATCam)
55718.53	5.53	...	14.44 (0.04)	14.06 (0.01)	14.27 (0.01)	...	LT (RATCam)
55720.44	7.44	15.39 (0.02)	13.97 (0.01)	13.53 (0.01)	13.73 (0.02)	13.87 (0.01)	LT (RATCam)
55721.44	8.44	15.09 (0.01)	13.78 (0.01)	13.33 (0.01)	13.52 (0.01)	13.64 (0.01)	LT (RATCam)
55722.44	9.44	...	13.59 (0.01)	13.18 (0.01)	13.35 (0.01)	13.49 (0.01)	LT (RATCam)
55723.41	10.41	14.82 (0.03)	...	13.02 (0.01)	13.16 (0.01)	13.34 (0.01)	LT (RATCam)
55724.41	11.41	14.72 (0.02)	...	12.93 (0.01)	13.05 (0.01)	13.22 (0.01)	LT (RATCam)
55725.43	12.43	14.74 (0.04)	...	12.83 (0.01)	12.94 (0.01)	13.09 (0.01)	LT (RATCam)
55729.39	16.39	14.56 (0.03)	13.10 (0.01)	12.56 (0.01)	12.62 (0.01)	12.81 (0.01)	LT (RATCam)
55730.40	17.40	14.45 (0.03)	13.07 (0.01)	12.51 (0.01)	12.56 (0.01)	12.77 (0.01)	LT (RATCam)
55731.41	18.41	14.54 (0.03)	13.02 (0.01)	12.46 (0.01)	12.51 (0.01)	12.71 (0.01)	LT (RATCam)
55731.82	18.82	...	13.07 (0.01)	12.46 (0.01)	12.50 (0.01)	12.65 (0.01)	FTN (FS02)
55732.46	19.46	14.56 (0.01)	13.00 (0.03)	12.42 (0.01)	12.48 (0.01)	12.67 (0.01)	LT (RATCam)
55733.45	20.45	14.52 (0.05)	13.03 (0.01)	12.41 (0.01)	12.45 (0.01)	12.65 (0.01)	LT (RATCam)
55735.44	22.44	14.75 (0.04)	13.12 (0.01)	12.43 (0.01)	12.41 (0.01)	12.60 (0.01)	LT (RATCam)
55736.44	23.44	14.96 (0.03)	13.19 (0.02)	12.45 (0.01)	12.42 (0.01)	12.59 (0.02)	LT (RATCam)
55738.45	25.45	15.37 (0.02)	13.43 (0.01)	12.55 (0.01)	12.47 (0.01)	12.65 (0.01)	LT (RATCam)
55739.44	26.44	15.55 (0.02)	13.50 (0.03)	12.59 (0.01)	12.50 (0.01)	12.65 (0.01)	LT (RATCam)
55740.44	27.44	15.80 (0.01)	13.66 (0.01)	12.66 (0.01)	12.55 (0.01)	12.70 (0.01)	LT (RATCam)
55741.44	28.44	...	13.75 (0.02)	12.76 (0.01)	12.59 (0.02)	12.76 (0.01)	LT (RATCam)
55742.49	29.49	16.20 (0.02)	13.92 (0.01)	12.84 (0.01)	12.65 (0.01)	12.80 (0.01)	LT (RATCam)
55745.44	32.44	16.71 (0.05)	14.20 (0.02)	13.04 (0.01)	12.79 (0.01)	12.87 (0.03)	LT (RATCam)
55745.80	32.80	...	14.35 (0.04)	13.00 (0.01)	12.79 (0.01)	12.94 (0.01)	FTN (FS02)
55746.45	33.45	16.83 (0.04)	14.32 (0.01)	13.09 (0.01)	12.82 (0.01)	12.94 (0.01)	LT (RATCam)
55747.44	34.44	16.90 (0.04)	14.40 (0.02)	13.13 (0.01)	12.86 (0.01)	12.95 (0.01)	LT (RATCam)
55748.44	35.44	17.09 (0.04)	14.42 (0.02)	13.19 (0.01)	12.90 (0.01)	13.01 (0.01)	LT (RATCam)
55750.44	37.44	17.20 (0.10)	14.55 (0.02)	13.29 (0.01)	13.02 (0.02)	13.04 (0.04)	LT (RATCam)
55751.43	38.43	17.14 (0.03)	14.64 (0.03)	13.36 (0.01)	13.04 (0.01)	13.11 (0.01)	LT (RATCam)
55752.45	39.45	17.24 (0.07)	14.66 (0.01)	13.39 (0.01)	13.04 (0.01)	13.09 (0.01)	LT (RATCam)
55756.46	43.46	...	14.79 (0.01)	13.55 (0.01)	13.22 (0.01)	13.19 (0.01)	LT (RATCam)
55762.78	49.78	...	15.00 (0.02)	13.68 (0.01)	13.37 (0.01)	13.28 (0.01)	FTN (FS02)
55767.43	54.43	17.30 (0.02)	15.03 (0.01)	13.84 (0.01)	13.52 (0.01)	13.38 (0.02)	LT (RATCam)
55768.45	55.45	17.29 (0.02)	15.03 (0.01)	13.86 (0.01)	13.56 (0.01)	13.41 (0.01)	LT (RATCam)
55773.39	60.39	17.27 (0.04)	15.07 (0.01)	13.99 (0.01)	13.72 (0.01)	13.54 (0.02)	NOT (ALFOSC)
55776.38	63.38	17.36 (0.03)	15.13 (0.01)	14.03 (0.01)	13.76 (0.01)	13.56 (0.01)	NOT (ALFOSC)
55780.41	67.41	17.33 (0.03)	15.16 (0.01)	14.09 (0.01)	13.84 (0.01)	13.61 (0.01)	NOT (ALFOSC)
55783.44	70.44	17.26 (0.04)	15.18 (0.01)	14.19 (0.01)	13.93 (0.01)	13.67 (0.01)	NOT (ALFOSC)
55784.77	71.77	...	15.23 (0.02)	14.16 (0.01)	13.88 (0.01)	13.64 (0.01)	FTN (FS02)
55790.38	77.38	17.29 (0.03)	15.35 (0.04)	14.28 (0.01)	14.04 (0.01)	13.69 (0.02)	LT (RATCam)
55793.37	80.37	17.32 (0.03)	15.30 (0.01)	14.39 (0.01)	14.16 (0.01)	13.84 (0.01)	NOT (ALFOSC)
55797.76	84.76	...	15.38 (0.01)	14.42 (0.01)	14.18 (0.01)	13.82 (0.01)	FTN (FS02)
55798.37	85.37	17.35 (0.03)	15.38 (0.01)	14.50 (0.01)	14.26 (0.01)	13.87 (0.01)	NOT (ALFOSC)
55801.36	88.36	17.34 (0.01)	15.42 (0.01)	14.53 (0.01)	14.31 (0.01)	13.89 (0.01)	NOT (ALFOSC)
55810.34	97.34	17.49 (0.02)	15.55 (0.01)	14.75 (0.01)	14.56 (0.01)	14.10 (0.02)	NOT (ALFOSC)
55886.75	173.75	21.74 (1.97)	16.99 (0.01)	16.36 (0.01)	16.16 (0.01)	...	NOT (ALFOSC)
55894.76	181.76	18.89 (0.03)	17.19 (0.02)	16.50 (0.01)	16.28 (0.02)	16.31 (0.02)	NOT (ALFOSC)
55898.73	185.73	18.97 (0.03)	17.25 (0.01)	16.59 (0.01)	16.42 (0.01)	16.49 (0.01)	NOT (ALFOSC)
55903.76	190.76	19.07 (0.05)	17.32 (0.02)	16.68 (0.01)	16.47 (0.01)	16.68 (0.04)	NOT (ALFOSC)
55912.79	199.79	19.28 (0.04)	17.48 (0.02)	16.86 (0.01)	16.66 (0.01)	16.79 (0.03)	NOT (ALFOSC)

Table 5. Continued.

JD (+2400000) (d)	Phase (d)	u (mag)	g (mag)	r (mag)	i (mag)	z (mag)	Telescope (Instrument)
55922.77	209.77	19.44 (0.02)	17.71 (0.01)	17.05 (0.01)	16.83 (0.01)	17.18 (0.01)	NOT (ALFOSC)
55932.79	219.79	19.50 (0.05)	17.83 (0.02)	17.18 (0.02)	17.01 (0.02)	17.37 (0.04)	NOT (ALFOSC)
55939.74	226.74	19.74 (0.05)	18.02 (0.01)	17.31 (0.01)	17.11 (0.01)	17.49 (0.02)	NOT (ALFOSC)
55948.73	235.73	19.87 (0.03)	18.15 (0.01)	17.45 (0.01)	17.27 (0.01)	17.74 (0.01)	NOT (ALFOSC)
55955.76	242.76	20.01 (0.03)	18.27 (0.01)	17.57 (0.01)	17.40 (0.01)	17.87 (0.02)	NOT (ALFOSC)
55975.69	262.69	20.37 (0.04)	18.64 (0.01)	17.84 (0.01)	17.71 (0.01)	18.25 (0.02)	NOT (ALFOSC)
55982.74	269.74	20.64 (0.05)	18.74 (0.01)	17.92 (0.01)	17.86 (0.01)	18.42 (0.03)	NOT (ALFOSC)
55987.62	274.62	20.47 (0.11)	18.76 (0.01)	17.95 (0.01)	17.96 (0.01)	18.30 (0.03)	LT (RATCam)
56008.66	295.66	...	19.14 (0.02)	18.22 (0.01)	18.33 (0.03)	19.27 (0.10)	LT (RATCam)
56014.52	301.52	21.28 (0.04)	19.30 (0.01)	18.40 (0.01)	18.45 (0.01)	19.02 (0.02)	NOT (ALFOSC)
56043.60	330.60	21.73 (0.03)	19.82 (0.01)	18.82 (0.01)	18.96 (0.01)	19.52 (0.03)	NOT (ALFOSC)
56071.43	358.43	21.85 (0.06)	20.27 (0.02)	19.26 (0.02)	19.62 (0.03)	19.98 (0.05)	NOT (ALFOSC)
56096.49	383.49	22.35 (0.05)	20.61 (0.02)	19.55 (0.02)	20.09 (0.03)	...	NOT (ALFOSC)
56132.43	419.43	...	21.14 (0.03)	20.21 (0.03)	20.79 (0.05)	21.25 (0.17)	NOT (ALFOSC)
56133.41	420.41	...	21.30 (0.04)	20.21 (0.03)	20.95 (0.06)	...	NOT (ALFOSC)
56154.39	441.39	...	21.50 (0.04)	20.61 (0.03)	21.32 (0.07)	...	NOT (ALFOSC)
56313.75	600.75	...	...	22.46 (0.11)	...	...	NOT (ALFOSC)
56428.46	715.46	...	...	23.10 (0.20)	...	...	NOT (ALFOSC)

Table 6. NIR S-corrected 2MASS *JHK* magnitudes for SN 2011dh. Errors are given in parentheses. For completeness data for the first 100 days already published in E14 are included.

JD (+2400000) (d)	Phase (d)	*J* (mag)	*H* (mag)	*K* (mag)	Telescope (Instrument)
55716.51	3.51	14.09 (0.01)	13.90 (0.01)	13.68 (0.02)	TNG (NICS)
55722.40	9.40	12.89 (0.01)	12.87 (0.01)	12.67 (0.01)	TNG (NICS)
55725.50	12.50	12.61 (0.04)	12.54 (0.01)	12.43 (0.02)	NOT (NOTCAM)
55730.51	17.51	12.12 (0.01)	12.08 (0.01)	11.94 (0.01)	TNG (NICS)
55737.72	24.72	11.96 (0.01)	11.90 (0.01)	11.72 (0.03)	LBT (LUCIFER)
55741.13	28.13	11.94 (0.01)	11.90 (0.02)	11.70 (0.05)	TCS (CAIN)
55748.43	35.43	12.14 (0.01)	12.00 (0.02)	11.77 (0.01)	TCS (CAIN)
55750.42	37.42	12.19 (0.01)	12.00 (0.01)	11.84 (0.04)	TCS (CAIN)
55751.42	38.42	12.29 (0.01)	12.01 (0.01)	11.84 (0.03)	TCS (CAIN)
55758.45	45.45	12.55 (0.01)	12.22 (0.01)	12.06 (0.01)	TNG (NICS)
55759.41	46.41	12.49 (0.03)	12.22 (0.03)	12.11 (0.04)	TCS (CAIN)
55762.41	49.41	12.57 (0.01)	12.26 (0.01)	12.17 (0.03)	TCS (CAIN)
55763.42	50.42	12.62 (0.02)	12.27 (0.04)	12.25 (0.06)	TCS (CAIN)
55765.45	52.45	12.79 (0.01)	12.38 (0.01)	12.23 (0.01)	TNG (NICS)
55769.41	56.41	12.77 (0.01)	12.48 (0.06)	12.40 (0.03)	TCS (CAIN)
55773.37	60.37	12.94 (0.03)	12.58 (0.01)	12.42 (0.02)	TNG (NICS)
55774.40	61.40	12.90 (0.01)	12.55 (0.03)	12.43 (0.04)	TCS (CAIN)
55776.40	63.40	13.00 (0.01)	12.64 (0.01)	12.53 (0.02)	TCS (CAIN)
55781.41	68.41	13.23 (0.01)	12.76 (0.01)	12.66 (0.01)	WHT (LIRIS)
55787.44	74.44	13.56 (0.03)	13.03 (0.02)	12.95 (0.02)	NOT (NOTCAM)
55801.36	88.36	13.90 (0.02)	13.41 (0.02)	13.17 (0.01)	TNG (NICS)
55804.34	91.34	14.10 (0.01)	13.50 (0.01)	13.26 (0.01)	CA-3.5m (O2000)
55814.32	101.32	14.38 (0.01)	13.80 (0.01)	13.50 (0.01)	CA-3.5m (O2000)
55818.36	105.36	14.45 (0.02)	13.91 (0.01)	13.74 (0.01)	NOT (NOTCAM)
55880.72	167.72	16.23 (0.01)	15.38 (0.01)	14.70 (0.01)	CA-3.5m (O2000)
55913.68	200.68	17.00 (0.01)	16.19 (0.02)	15.31 (0.02)	CA-3.5m (O2000)
55914.66	201.66	17.05 (0.01)	16.23 (0.02)	15.35 (0.02)	CA-3.5m (O2000)
55946.13	233.13	17.43 (0.02)	16.78 (0.02)	16.21 (0.02)	UKIRT (WFCAM)
55999.91	286.91	18.10 (0.02)	17.47 (0.02)	17.31 (0.02)	UKIRT (WFCAM)
56024.38	311.38	18.46 (0.03)	17.80 (0.03)	17.71 (0.04)	WHT (LIRIS)
56052.47	339.47	18.69 (0.02)	17.96 (0.02)	18.60 (0.03)	WHT (LIRIS)
56093.48	380.48	19.71 (0.06)	18.71 (0.06)	19.21 (0.08)	WHT (LIRIS)

Table 7. MIR Spitzer 3.6 μm and 4.5 μm magnitudes for SN 2011dh. Errors are given in parentheses. For completeness data for the first 100 days already published in E14 are included.

JD (+2400000) (d)	Phase (d)	3.6 μm (mag)	4.5 μm (mag)	Telescope (Instrument)
55731.21	18.21	11.83 (0.02)	11.48 (0.02)	SPITZER (IRAC)
55737.06	24.06	11.66 (0.02)	11.31 (0.02)	SPITZER (IRAC)
55744.32	31.32	11.66 (0.02)	11.30 (0.02)	SPITZER (IRAC)
55751.46	38.46	11.68 (0.02)	11.30 (0.02)	SPITZER (IRAC)
55758.75	45.75	11.79 (0.02)	11.32 (0.02)	SPITZER (IRAC)
55766.45	53.45	11.96 (0.02)	11.34 (0.02)	SPITZER (IRAC)
55772.33	59.33	12.11 (0.03)	11.38 (0.02)	SPITZER (IRAC)
55779.12	66.12	12.30 (0.03)	11.43 (0.02)	SPITZER (IRAC)
55785.60	72.60	12.50 (0.03)	11.50 (0.02)	SPITZER (IRAC)
55798.28	85.28	12.84 (0.04)	11.66 (0.03)	SPITZER (IRAC)
55964.14	251.14	14.34 (0.09)	13.31 (0.07)	SPITZER (IRAC)
56026.63	313.63	15.57 (0.15)	14.27 (0.11)	SPITZER (IRAC)
56104.23	391.23	17.12 (0.32)	15.54 (0.19)	SPITZER (IRAC)
56136.41	423.41	17.46 (0.37)	16.01 (0.24)	SPITZER (IRAC)
56168.69	455.69	17.63 (0.40)	16.25 (0.26)	SPITZER (IRAC)
56337.59	624.59	18.42 (0.57)	17.59 (0.49)	SPITZER (IRAC)

Table 8. List of late-time (100-415 days) optical and NIR spectroscopic observations.

JD (+2400000) (d)	Phase (d)	Grism	Range (Å)	Resolution	Resolution (Å)	Telescope (Instrument)
55821.33	108.33	b200	3300-8700	...	12.0	CA-2.2m (CAFOS)
55821.33	108.33	r200	6300-10500	...	12.0	CA-2.2m (CAFOS)
55828.35	115.35	R300B	3200-5300	...	4.1	WHT (ISIS)
55828.35	115.35	R158R	5300-10000	...	7.7	WHT (ISIS)
55830.25	117.25	Grism 4	3500-8450	613	...	AS 1.82m (AFOSC)
55864.65	151.65	Grism 4	3500-8450	613	...	AS 1.82m (AFOSC)
55867.71	154.71	?	?-?	...	?	CA-2.2m (CAFOS)
55893.76	180.76	Grism 3	3200-6700	345	12.4	NOT (ALFOSC)
55897.76	184.76	Grism 5	5000-10250	415	16.8	NOT (ALFOSC)
55911.20	198.20	zJ	8900-15100	700	...	WHT (LIRIS)
55914.70	201.70	R300B	3200-5300	...	8.2	WHT (ISIS)
55914.70	201.70	R158R	5300-10000	...	15.4	WHT (ISIS)
55918.69	205.69	HK	14000-25000	333	...	TNG (NICS)
55951.64	238.64	Grism 4	3200-9100	355	16.2	NOT (ALFOSC)
55998.68	285.68	r200	6300-10500	...	12.0	CA-2.2m (CAFOS)
56005.63	292.63	Grism 4	3200-9100	355	16.2	NOT (ALFOSC)
56013.14	300.14	R600B	?-?	...	5.7	WHT (ISIS)
56013.14	300.14	R316R	?-?	...	3.0	WHT (ISIS)
56071.56	358.56	R500B	3440-7600	322	15.0	GTC (OSIRIS)
56072.61	359.61	R500R	4800-10000	352	20.8	GTC (OSIRIS)
56128.47	415.47	R300B	3600-7000	270	16.7	GTC (OSIRIS)

Table 9. Pseudo-bolometric 3-300 days UV to MIR lightcurve for SN 2011dh calculated from spectroscopic and photometric data with a 1-day sampling between 3 and 50 days and a 5-day sampling between 50 and 300 days. Random errors are given in the first parentheses and systematic lower and upper errors (arising from the distance and extinction) respectively in the second parentheses.

JD (+2400000) (d)	Phase (d)	L (log erg s^{-1})	JD (+2400000) (d)	Phase (d)	L (log erg s^{-1})
55717.00	4.00	41.465 (0.001) (0.098,0.186)	55773.00	60.00	41.670 (0.002) (0.093,0.160)
55718.00	5.00	41.553 (0.001) (0.097,0.181)	55778.00	65.00	41.627 (0.002) (0.093,0.160)
55719.00	6.00	41.653 (0.001) (0.097,0.179)	55783.00	70.00	41.585 (0.002) (0.093,0.161)
55720.00	7.00	41.747 (0.001) (0.097,0.178)	55788.00	75.00	41.544 (0.002) (0.093,0.161)
55721.00	8.00	41.835 (0.001) (0.097,0.178)	55793.00	80.00	41.502 (0.002) (0.093,0.161)
55722.00	9.00	41.909 (0.001) (0.097,0.178)	55798.00	85.00	41.460 (0.002) (0.093,0.162)
55723.00	10.00	41.970 (0.001) (0.097,0.177)	55803.00	90.00	41.417 (0.002) (0.094,0.162)
55724.00	11.00	42.019 (0.001) (0.097,0.176)	55808.00	95.00	41.375 (0.002) (0.094,0.163)
55725.00	12.00	42.057 (0.001) (0.097,0.176)	55813.00	100.00	41.333 (0.002) (0.094,0.163)
55726.00	13.00	42.089 (0.001) (0.096,0.175)	55818.00	105.00	41.291 (0.002) (0.094,0.163)
55727.00	14.00	42.118 (0.001) (0.096,0.174)	55823.00	110.00	41.249 (0.001) (0.094,0.164)
55728.00	15.00	42.142 (0.001) (0.096,0.174)	55828.00	115.00	41.208 (0.001) (0.094,0.164)
55729.00	16.00	42.164 (0.001) (0.096,0.173)	55833.00	120.00	41.166 (0.001) (0.094,0.164)
55730.00	17.00	42.182 (0.001) (0.096,0.173)	55838.00	125.00	41.124 (0.001) (0.094,0.164)
55731.00	18.00	42.198 (0.001) (0.096,0.173)	55843.00	130.00	41.081 (0.002) (0.094,0.164)
55732.00	19.00	42.209 (0.001) (0.096,0.172)	55848.00	135.00	41.038 (0.002) (0.094,0.165)
55733.00	20.00	42.214 (0.001) (0.096,0.172)	55853.00	140.00	40.995 (0.001) (0.094,0.165)
55734.00	21.00	42.216 (0.001) (0.096,0.171)	55858.00	145.00	40.953 (0.001) (0.094,0.165)
55735.00	22.00	42.211 (0.001) (0.095,0.171)	55863.00	150.00	40.909 (0.001) (0.094,0.165)
55736.00	23.00	42.201 (0.001) (0.095,0.170)	55868.00	155.00	40.863 (0.001) (0.094,0.165)
55737.00	24.00	42.186 (0.001) (0.095,0.169)	55873.00	160.00	40.817 (0.001) (0.094,0.165)
55738.00	25.00	42.165 (0.001) (0.095,0.167)	55878.00	165.00	40.772 (0.001) (0.094,0.165)
55739.00	26.00	42.142 (0.001) (0.094,0.166)	55883.00	170.00	40.726 (0.001) (0.094,0.164)
55740.00	27.00	42.117 (0.001) (0.094,0.165)	55888.00	175.00	40.681 (0.001) (0.094,0.164)
55741.00	28.00	42.091 (0.001) (0.094,0.164)	55893.00	180.00	40.637 (0.001) (0.094,0.164)
55742.00	29.00	42.064 (0.001) (0.094,0.163)	55898.00	185.00	40.594 (0.001) (0.094,0.164)
55743.00	30.00	42.039 (0.001) (0.094,0.162)	55903.00	190.00	40.552 (0.001) (0.094,0.164)
55744.00	31.00	42.016 (0.001) (0.093,0.162)	55908.00	195.00	40.512 (0.001) (0.094,0.164)
55745.00	32.00	41.996 (0.001) (0.093,0.161)	55913.00	200.00	40.472 (0.001) (0.094,0.164)
55746.00	33.00	41.977 (0.001) (0.093,0.161)	55918.00	205.00	40.432 (0.001) (0.094,0.164)
55747.00	34.00	41.959 (0.001) (0.093,0.160)	55923.00	210.00	40.396 (0.001) (0.094,0.164)
55748.00	35.00	41.943 (0.001) (0.093,0.160)	55928.00	215.00	40.362 (0.001) (0.094,0.164)
55749.00	36.00	41.928 (0.001) (0.093,0.160)	55933.00	220.00	40.327 (0.001) (0.094,0.164)
55750.00	37.00	41.914 (0.001) (0.093,0.159)	55938.00	225.00	40.294 (0.001) (0.094,0.164)
55751.00	38.00	41.900 (0.001) (0.093,0.159)	55943.00	230.00	40.262 (0.001) (0.094,0.164)
55752.00	39.00	41.887 (0.001) (0.093,0.159)	55948.00	235.00	40.230 (0.001) (0.094,0.164)
55753.00	40.00	41.874 (0.001) (0.093,0.159)	55953.00	240.00	40.200 (0.001) (0.094,0.163)
55754.00	41.00	41.861 (0.001) (0.093,0.159)	55958.00	245.00	40.169 (0.001) (0.094,0.163)
55755.00	42.00	41.848 (0.001) (0.093,0.159)	55963.00	250.00	40.137 (0.001) (0.094,0.163)
55756.00	43.00	41.836 (0.001) (0.093,0.159)	55968.00	255.00	40.104 (0.001) (0.094,0.163)
55757.00	44.00	41.823 (0.001) (0.093,0.159)	55973.00	260.00	40.071 (0.001) (0.094,0.163)
55758.00	45.00	41.812 (0.001) (0.093,0.159)	55978.00	265.00	40.039 (0.001) (0.094,0.163)
55759.00	46.00	41.802 (0.001) (0.093,0.159)	55983.00	270.00	40.006 (0.001) (0.094,0.163)
55760.00	47.00	41.792 (0.001) (0.093,0.159)	55988.00	275.00	39.973 (0.001) (0.094,0.163)
55761.00	48.00	41.782 (0.001) (0.093,0.159)	55993.00	280.00	39.940 (0.001) (0.094,0.163)
55762.00	49.00	41.773 (0.002) (0.093,0.159)	55998.00	285.00	39.907 (0.001) (0.094,0.163)
55763.00	50.00	41.763 (0.002) (0.093,0.159)	56003.00	290.00	39.873 (0.001) (0.094,0.163)
55768.00	55.00	41.716 (0.002) (0.093,0.159)	56008.00	295.00	39.838 (0.001) (0.094,0.163)